12-2005

Effect of Hydrogenon on Mechanical Behavior of a Zircaloy-4 Alloy

Elena Garlea
University of Tennessee - Knoxville

To the Graduate Council:

I am submitting herewith a thesis written by Elena Garlea entitled "Effect of Hydrogenon on Mechanical Behavior of a Zircaloy-4 Alloy." I have examined the final electronic copy of this thesis for form and content and recommend that it be accepted in partial fulfillment of the requirements for the degree of Master of Science, with a major in Materials Science and Engineering.

Hahn Choo, Major Professor

We have read this thesis and recommend its acceptance:

Peter K. Liaw, Raymond A. Buchanan

Accepted for the Council:
Carolyn R. Hodges

Vice Provost and Dean of the Graduate School

(Original signatures are on file with official student records.)

To the Graduate Council:

I am submitting herewith a thesis written by Elena Garlea entitled "Effect of Hydrogen on Mechanical Behavior of a Zircaloy-4 Alloy." I have examined the final electronic copy of this thesis for form and content and recommend that it be accepted in partial fulfillment of the requirements for the degree of Master of Science, with a major in Materials Science and Engineering.

Hahn Choo

Major Professor

We have read this thesis
and recommend its acceptance:

Peter K. Liaw

Raymond A. Buchanan

Accepted for the Council:

Anne Mayhew

Vice Chancellor and
Dean of Graduate Studies

(Original signatures are on file with official student records.)

Effect of Hydrogen on Mechanical Behavior of a Zircaloy-4 Alloy

A Thesis

Presented for the

Master of Science Degree

The University of Tennessee, Knoxville

Elena Garlea

December 2005

Dedication

This thesis is dedicated to my husband Ovidiu for always believing in me, for his support and encouragement which helped me to reach this goal.

Acknowledgement

I wish to thank all those who helped me complete my Master of Science degree in Materials Science and Engineering.

I would like to thank my advisors, Profs. Choo, Liaw and Buchanan for their guidance and their efforts to make me familiar with the concepts of Neutron Diffraction, Mechanical Behavior, and Hydrogen Charging.

I would also like to thank Dr. Hubbard of the Oak Ridge National Laboratory for his assistance on the NRSF 2 instrument and for his valuable ideas through the research process. I would like to extend my thanks to Drs. Oliver and Santisteban of ISIS, Rutherford Appleton Laboratory, UK, for their help with the experimental work and data analysis.

I would like to acknowledge the National Science Foundation (NSF) International Materials Institutes (IMI) Program (DMR-0231320), managed by Drs. C. Huber and Tennessee Advanced Materials Laboratory (TAML) Fellowship Program with Prof. W. Plummer as the Program Director for financial support.

I wish to give special thanks to Hans Letzring of PPG Industries, for believing in me and being such an inspiration to me.

Lastly, I would like to thank my family and friends, whose suggestions and encouragement made this work possible.

Abstract

Hydride formation is one of the main degradation mechanisms of zirconium alloys in hydrogen-rich environments. When sufficient hydrogen is present, zirconium-hydride precipitates can be formed. Cracking of the brittle hydrides near a crack tip can initiate the growth of a crack leading to the premature failure of the material. Hydride formation is believed to be enhanced by the presence of residual or applied stresses. Therefore, the increase in the stress field ahead of a crack tip may promote precipitation of additional hydrides. In order to verify these phenomena, the effect of internal stresses on the zirconium-hydride-precipitate formation, and in turn, the influence of the hydrides on the subsequent intergranular strain evolution in a hexagonal-close-packed zircaloy-4 alloy were investigated, using neutron and x-ray diffraction.

First, the evolution of intergranular strains in a zircaloy-4 was investigated *in-situ*, using neutron diffraction, to understand the deformation behavior at the microscopic length scale. A series of uniaxial tensile loads up to 500 MPa was applied to a round-bar tensile specimen in the as-received condition and the intergranular (hkl-specific) strains, parallel and perpendicular to the loading direction, were studied. The results provide a fundamental understanding of the anisotropic elastic-plastic deformation of the zirconium alloy under applied stresses. Then the hydride formation was examined by conducting qualitative phase mapping across the diameter of two tensile specimens charged with hydrogen gas for ½ hour and 1 hour, respectively. It was observed that the zirconium hydrides (δ-ZrH_2) form a layer, in a ring shape, near the surface with a thickness of approximately 400 μm. The hydrogen-charging effects on intergranular strains were investigated and compared to the as-received specimen.

Second, spatially-resolved internal-strain mapping was performed on a fatigue pre-cracked compact-tension (CT) specimen using *in-situ* neutron diffraction under applied loads of 667 and 4,444 newtons, to determine the in-plane (parallel to the loading direction) and through–thickness (perpendicular to the loading direction) lattice-strain profiles around the crack tip. An increase in elastic lattice strains near the crack tip was observed with the increase in the applied stresses. The effect of hydrogen charging was

also investigated on CT specimens electrochemically charged with hydrogen. X-ray diffraction results clearly showed the presence of zirconium hydrides on the surface of the specimen. The internal strain in the hydrogen-charged specimen was measured, using neutron diffraction to provide an understanding of the effect of the surface hydrides on the strain profile near the crack-tip in comparison to the strain data measured from a CT specimen without hydrogen.

Future work is planned to correlate the uniaxial behavior with fracture mechanics characteristics of the hydrogen-charged Zircaloy-4 at continuum and mesoscopic length scales using *in-situ* diffraction and computational modeling.

Table of Contents

Table of Contents (continued)

Table of Contents (continued)

CHAPTER **PAGE**

Table of Contents (continued)

CHAPTER **PAGE**

List of Tables

List of Figures

List of Figures (continued)

List of Figures (continued)

List of Figures (continued)

List of Figures (continued)

FIGURE **PAGE**

List of Figures (continued)

FIGURE **PAGE**

List of Figures (continued)

List of Figures (continued)

FIGURE **PAGE**

List of Figures

FIGURE **PAGE**

Chapter 1

Introduction

The objective of this research is to investigate the deformation and fracture behavior of a zirconium alloy at mesoscopic scale, in hydrogen-rich environments using *in-situ* neutron-scattering technique.

The present research addresses important issues related to the life predictions of components operating in corrosive environments important for fossil, nuclear energy, and aerospace industries.

The hydride formation is one of the main degradation sources of zirconium alloys in hydrogen-rich environments. When sufficient hydrogen (H) is available in these alloys, zirconium-hydride precipitates can be formed. The brittle hydrides near a crack tip can facilitate crack initiation and growth leading to the premature failure of the material. The hydride formation is believed to be enhanced by the presence of residual or applied stresses. Therefore, the increase in the stress field ahead of a crack tip may promote precipitation of additional hydrides. Thus, understanding the hydride phase formation around the crack tip in a corrosive environment and its effects on the performance and reliability is a critical issue in the current surge of "hydrogen economy".

Figure 1.1* shows the flow chart of the detailed research plan on Zircaloy-4 (Zr-4) alloy. At the top, the materials and material conditions are indicated in square boxes, followed by the techniques and tests that were employed to study these materials. Each block arrow on the far left side states a scientific issue and points towards the test that needs to be done. The tests that use a similar technique appear in a similar type of boxes, however, if a different issue is addressed, the color changes. Note, that the tasks, shown in white boxes with dotted outlines, are not meant to be accomplished for the Master's Thesis.

---

*All figures are in the Appendix

They are included in this chart to provide a big picture of the overall research project and are planned to be completed for a Ph.D. Thesis.

Chapter 2 presents a summary of the literature survey on the effects of hydrogen on mechanical behavior of metals. Also, neutron-diffraction techniques employed for phase and strains studies will be discussed. It begins with a general presentation related to state of hydrogen, effects on iron-based alloys and then focuses on zirconium alloys, which have practical engineering importance and also allow the study of the hydrogen embrittlement through the hydride formation. Hydrogen damages occur when hydrogen is absorbed in metals and weakens the load-carrying capacity of the metal. This process can occur during the production, processing, and/or the service of the metal. Furthermore, hydrogen tends to accumulate at the grain boundaries, inclusions, voids, dislocation arrays, and solute atoms. To this extent, the hydrogen embrittlement is controlled by those hydrogen-accumulation sites that are most sensitive to fracture.

Hydrogen damage to specific alloys manifests itself in many ways, and accordingly, there are numerous theories for the various forms of degradation. Therefore, reviewing the voluminous literature on the subject, one may safely summarize that, despite the extensive studies over 100 years, a complete mechanistic understanding of hydrogen embrittlement has yet to be achieved. No single mechanism is responsible for all hydrogen-induced failures [1, 2]. Many mechanisms have been proposed to explain hydrogen-related failures and, as the evidence for and against each mechanism have been extensively reviewed [3, 4].

At the end of Chapter 2, neutron-diffraction techniques employed for the phase and strain measurements are reviewed. Neutron scattering is an efficient experimental technique, which allows the non-destructive measurements of the total hydrogen content in any alloy. Moreover, the high penetration of thermal neutrons through most engineering materials, such as steels, aluminium, or zirconium alloys, makes it possible to measure nondestructively internal stresses deep inside industrial components.

Chapter 3 is devoted to the experimental approaches employed to address the scientific issues. First, the Zr-4 specimen preparations will be discussed, followed by the metallographic methods utilized to investigate the fracture surface of the samples, such as

optical and scanning-electron microscopy. Then the experimental setups for phase and strain studies are illustrated for two different specimen geometries, cylindrical tensile and compact-tension specimens using pulsed-neutron sources. The incoherent neutron scattering experiment is also described.

In Chapter 4, the experimental results and the scientific interpretations will be presented. First, the macro- and micro- structures of specimens with and without hydrogen are shown. Then the phase-study results obtained from the surface and the bulk of the hydrogen-charged specimens are presented. Finally, the bulk-averaged intergranular strains measured from the *in-situ* tensile loading and strain profiles measured at the crack tip are shown as a function of the applied loads and hydrogen contents.

The conclusions drawn from this study are presented in Chapter 5 and the future research plans are mentioned in Chapter 6.

Chapter 2

Literature Review

2.1. Overview

This review summarizes critical issues related to the effects of hydrogen on mechanical-behavior of metals and neutron-diffraction techniques for phase and strains studies. It starts with a general presentation of state of hydrogen in iron-based alloys and then focuses on zirconium alloys, which have practical engineering importance and allow the study of hydrogen embrittlement through the hydride formation. Neutron-diffraction techniques employed for the phase study and strain measurements are also reviewed.

2.2. Hydrogen-Metal Interaction

2.2.1. Generalities

Hydrogen (H) along with its isotopes (deuterium, tritium, and also the light isotope muonium) is the simplest element in the periodic table with just one electron. As a gas it exists in the form of molecular H_2, which liquefies (21 K) and solidifies (14 K) at low temperatures. Solid hydrogen is a molecular insulating solid. Under high-pressures, the molecular insulating and transparent solid hydrogen should transform into an atomic solid, which should become the simplest metal and theoretically a room-temperature superconductor [5]. Experimentally full metallization was not reached with solid hydrogen, but with liquid hydrogen, and the shock-induced transformation of liquid deuterium into a metallic fluid was also shown [6]. Hydrogen is a quantum gas, similar to and different from helium, as was shown by Bose–Einstein-condensation experiments [7]. Hydrogen is the most abundant element the universe (75%). On earth it is found in small concentrations in air and also in H_2O in unlimited amounts, but chemically bounded. In the area of energy technology H is found in gaseous, liquid, or solid hydrocarbons, (e.g. CH_4), in nuclear fusion and fission processes, and is consider as a

future synthetic fuel produced by the dissociation of H_2O or CH_4 using an appropriate primary energy.

Another form of hydrogen is the hydrogen plasma, a neutral mixture of protons, electrons, neutral atoms, and photons produced, e.g., by a discharge or by microwaves [8].

2.2.2. The State of Hydrogen in Alloys

It is instructive to summarize many important facts concerning the state of hydrogen in iron-based alloys and other materials, which have practical engineering importance and are subject to stress corrosion cracking.

1) Hydrogen dissolves atomically in virtually all metals and is ionized, i.e., it gives its electron to the conduction band of the host metal. The concentration of hydrogen, $C_{\underline{H}}$, dissolved in a metal in equilibrium with the hydrogen gas can be generally described in a range of temperatures, T, and partial pressures of hydrogen, P_{H_2} by using Sievert's law:

$$C_{\underline{H}} = \eta\,(T)\, P_{H_2}^{1/2} \tag{2.1}$$

where η (T) is a temperature-dependent constant of proportionality [9].

2) Hydrogen dissolves interstitially in virtually all metals. While many studies suggest this type of behavior (e.g., analyses of thermodynamic and diffusion data, lattice parameters, or electrical resistivity) [10], neutron-diffraction [11-13] and the occurrence of Snoek mechanical and magnetic relaxation peaks [15-17] in several materials offer the most convincing evidences of this trend.

3) Hydrogen dissolves in most metals causing a large lattice distortion. This is particularly true in α-iron and other bcc metals, where the partial molar volumes of hydrogen, $V_{\underline{H}}$ are ≥ 2.0. Other kinds of data, which show a large lattice distortion, include internal friction [18], mechanical properties [19], and electrical resistivity [20, 21].

4) The interstitial sites occupied by hydrogen in a solid solution in various metals have not been established with certainty, largely because analyses of the various

techniques (e.g., internal friction, neutron diffraction, thermodynamic data, diffusion data, and lattice parameters) are not unequivocal.

5) Consistent with its interstitial site occupancy, hydrogen diffuses with a high mobility in most metals. This is especially true in bcc metals, for which activation energies for hydrogen diffusion are typically on the order of 1-5 kcal/mol [22, 23]. Because of the larger interstices and close packing of host atoms in fcc and hcp metals, the mobility of hydrogen is less than in bcc metals. Activation energies on the order of 5-15 kcal/mol are usually encountered in the fcc and hcp metals. Even so, these are small energies and the equilibrium between hydrogen and its crystalline environments can be attained in many practical materials situations. Two major complications occur in the diffusion of hydrogen in metals: (a) hydrogen interaction with defect "traps", which can appreciably lower the effective diffusivity at lower temperatures [24] and (b) quantum tunneling of hydrogen at very low temperatures, which results in a higher diffusivity than expected [14]. Both effects are well documented in the literature.

6) The solid solutions of hydrogen in most metals are noticeably non-ideal, [25] although the nature of the non-idealities is not agreed upon. For example, both attractive and repulsive hydrogen-hydrogen interactions have been postulated for refractory metal-solid solutions [23, 26]. In many materials embrittled easily by hydrogen, the hydrogen solubility becomes quite small at low temperatures, but can be enhanced by the presence of defect traps. Super-saturations of hydrogen in the solution will usually result either directly from the excessive hydrogen trapped at defects or from the inability of a hydride phases to nucleate at temperatures at which they are thermodynamically stable.

7) The interaction of hydrogen with defect-traps is universally observed in metal-hydrogen systems [10, 24]. Some interactions are strong and influence properties significantly over wide temperature ranges. However, because of the high mobility of hydrogen, even the relatively weak interactions can have significant effect on properties at lower temperatures [27].

2.2.3. Hydrogen and Group IVB Metals: (Ti, Zr, Hf)

Metals, intermetallic compounds, and alloys generally react with hydrogen and form mainly solid metal-hydrogen compounds. Hydrides exist as ionic, polymeric covalent, volatile covalent, and metallic hydrides. The demarcation between the various types of hydrides is not sharp; they merge into each other according to the electronegativities of the elements concerned. Hydrogen reacts at elevated temperatures with many transition metals and their alloys to form hydrides.

Titanium, zirconium, and hafnium (the metals in Group IV B in the Periodic Table of the Elements, Figure 2.1, possess α-hcp crystal structures at room temperature, which transform to bcc β–allotropic modifications at 882, 870, and 782 °C, respectively.

As a consequence, the Ti-H and Zr-H phase diagrams exhibit the expected eutectoid solid-phase reactions; but data at high temperatures to reveal the corresponding transformation reaction in the Hf-H system are not available.

Neutron diffraction studies by Sidhu et al. [28] have verified the speculation by Hägg [29] that the hydrogen atoms are absorbed in the tetrahedral interstices of the fluorite structure. It is apparent, Figure 2.2(a) [30] that hydrogen stabilizes the β-phase relative to the α-phase. Below the eutectoid temperature (573 K), the β-solid solution phase reacts to form the α-solid solution phase in equilibrium with the fluorite, TiH_{2-x} (γ) hydride. As the hydrogen content of the γ-hydride phase is increased, the cubic fluorite structure is distorted to a slightly tetragonal structure due to anisotropic lattice strain. Yakel [30] found that the transition from a cubic to tetragonal structure (a low-temperature phase) of the hydride ($TiH_{1.99}$) and the deuteride ($TiH_{1.98}$) occurred at 310 K. Since no discontinuity in the thermal expansivity as a function of temperature was observed, it was concluded that the transition was of the second order.

The zirconium-hydrogen phase diagram [30], Figure 2.2(b), is similar to the titanium-hydrogen phase diagram. The β-solid solution decomposes into an α-solid solution in equilibrium with the δ-hydride, ZrH_{2-x} at the eutectoid temperature of 550 ^{0}C (823 K). As more hydrogen is absorbed, a first-order phase transition transforms the fluorite δ-hydride to the body-centered-tetragonal ε-hydride (ZrH_2).

The hafnium-hydrogen system, as one would expect from the similarity of the metals, resembles the zirconium-hydrogen system: an α-hcp solid solution in equilibrium with a fluorite δ-hydride (HfH_{2-x}) and the ε-hydride phase (HfH_2 body-centered tetragonal structure) formed by a first-order phase transition from the δ-hydride.

2.3. Hydrogen Effects on Materials Behavior

The hydrogen damage occurs when hydrogen is absorbed in metals and weakens the load-carrying capacity of the metal. Metals absorb hydrogen when exist in an environment that contains or generates hydrogen. This trend can take place during the production, processing, and/or the service of the metal. Some reactive metals, such as titanium or zirconium, can form brittle hydrides from the dissolved hydrogen. Hydrogen also can react with carbon in steels to reduce the strength and/or ductility. The hydrogen dissolved in the crystal lattice produces effects generally classified as hydrogen embrittlement. The major form of hydrogen embrittlement is hydrogen-induced cracking (HIC) of various high-strength alloys (ferrous and nonferrous) under sustained tensile loads in the presence of hydrogen or hydrogen-bearing environments.

2.3.1. Embrittlement

Hydrogen embrittlement is a severe environmental type of failure that affects almost all metals and their alloys. For example, the high-symmetry ordered intermetallic, Ni_3Al exhibits very poor ductility and brittle fracture in the presence of hydrogen or even moist air [31, 32]. In general, hydrogen enters a lattice as a monoatomic hydrogen atom (or ion) that forms as part of an electrochemical process (active corrosion, electroplating, etc) or when a sample under stress (either externally applied or residual) is exposed to a hydrogen gas atmosphere [33]. The flow diagram showed in Figure 2.3 [34] provides a useful summary of hydrogen sources, transport paths, destinations, and induced fracture micromechanics. It can be seen that hydrogen can enter the metal in a number of different ways: when dissolved in the molten metal hydrogen would form entrapped gas pockets upon solidification, or hydrogen from the residual water during welding could enter the metal, while the weld is hot. The hydrogen pickup and associated embrittlement can be

introduced into the metal whenever a sample under stress is exposed to a hydrogen-gas atmosphere. It is believed that the molecular hydrogen is dissociated by the chemisorption on iron, allowing the liberated atomic hydrogen to diffuse internally and embrittle the metal. Likewise, it has been shown that hydrogen is a product of the corrosion reaction between iron and water; this hydrogen then follows the same path as the chemisorbed hydrogen to the metal interior.

Hydrogen can diffuse rapidly through the lattice because of its small size. Calculations have shown that hydrogen transport rates in association with the dislocation motion can be several orders of magnitude greater than that associated with lattice diffusion. Furthermore, hydrogen tends to accumulate at grain boundaries, inclusions, voids, dislocation array, and solute atoms. The cracking process can involve cleavage, intergranular, or ductile fracture mechanisms [34].

Reviewing the voluminous literature on the subject, one may safely summarize that, despite the study for 100 years, a complete mechanistic understanding of hydrogen embrittlement has yet to be achieved. No single mechanism is responsible for all hydrogen-induced failures [2]. Many mechanisms have been proposed to explain the hydrogen-related failure and the evidences for and against each mechanism have been extensively reviewed [3, 35]. Sofronis and Roberston [35] provide the theoretical and experimental evidence for just one mechanism, namely the hydrogen-enhanced localized plasticity (HELP) mechanism. The evidence of plasticity on hydrogen-induced fracture surfaces has been a common observation for over 30 years and is not an issue of dispute [36, 37]. The remaining issue is the significance of the observation of plasticity. Generally, this plasticity was dismissed as an occurrence during or following hydrogen embrittlement rather than a cause of it. This trend may be attributed in part to the resolution at which the fracture surfaces were examined. At low resolutions, the effects of the localization of the ductility to regions of high hydrogen concentration would not be discernible; giving fracture surfaces a brittle appearance.

Beachem [37] was the first to propose, on the basis of the careful fractography of hydrogen-embrittled steels, that the failure occurred by ductile processes and that hydrogen enhanced and not retarded the mobility of dislocations. This idea was dismissed

and ignored until the late 1970s and early 1980s when Robertson, Birnbaum, and coworkers [38] revived Beachem's mechanism. They provided a direct observation of the dislocation-velocity enhancement due to hydrogen by deforming materials *in-situ* in a transmission electron microscope equipped with an environmental cell. Sofronis and Robertson combined experimental and numerical/analytical results to provide the explanation for the hydrogen-enhanced localized plasticity mechanism of hydrogen embritlement [35].

A basic, quantitative understanding of hydrogen embrittlement in metallic materials will be possible only if we know the characteristics and parameters associated with the entry of hydrogen. Thus, it is imperative to know the hydrogen permeation characteristics of a metallic material in order to gauge its hydrogen embrittlement behavior. The hydrogen-permeation characteristics of a metallic material in electrolytic solutions have been studied for a long time by using the electrochemical Devanathan–Stachurski cell method [39]. In this technique, the specimen to be studied is in the form of a thin membrane that is attached to a cathodic cell on one side and an anodic cell on the other side. A part of the discharged hydrogen is absorbed into the metallic membrane, and this hydrogen diffuses through the membrane to the anodic cell. The measured current in this anodic cell is a measure of the hydrogen-permeation flux. The important quantities measured are the electrode potential of the cathodic (hydrogen input) surface and the permeation current at the anodic (hydrogen exit) surface for each of the applied cathodic currents. However, for obtaining the meaningful and quantitative interpretation these measurements it is critical to understand the physical and electrochemical aspects. As far as the hydrogen embrittlement of the metallic material is concerned, the hydrogen entry kinetics, transport, and trapping aspects are the most important. It is possible to characterize the hydrogen transport and trapping behavior from the permeation measurements by applying the diffusion equations [40] and models of hydrogen trapping [41- 44]. If the diffusional condition is met, then one can obtain the lattice diffusivity (D_L) of hydrogen in the absence of hydrogen trapping by relationship [43]:

$$D_L = (1/6)(L^2/t_l) \tag{2.2}$$

where L = membrane thickness, and t_l = time lag measured from the transient hydrogen permeation curve. In the presence of significant trapping of hydrogen, D_L can be obtained as:

$$D_L = (1/6)\ (L^2/t_t)(1+c_{t'})^{-1} \tag{2.3}$$

where t_t = time lag in the presence of hydrogen trapping and $c_{t'} \equiv \delta c_t/\delta c_l$, which can be obtained from the trapping model relating the trapped hydrogen concentration (c_t) and the lattice hydrogen concentration (c_l) [41]. The actual transient curve will also include the information about the film-reduction kinetics, complicating evaluation of the hydrogen transport and trapping parameters. These surface effects are probably why the values of transport and especially trapping parameters in the hydrogen permeation literature are non-reproducible and perhaps unrealistic [42, 45-48].

However, the various kinetic parameters related to the hydrogen discharged, recombination, and permeation were not determinable until recently, with the development of a mechanism and analytical model, which for the first time, has considered the effect of hydrogen entry into a metallic material on the kinetics of the hydrogen evolution reaction (h. e. r.), and has recognized the significantly larger absorption of hydrogen into the metallic materials in poisoned electrolytes. Such a model is the I-P-Z model [49, 50], which enable the computation of the hydrogen discharging and recombination reaction rate constants and the hydrogen adsorption. This model quantitatively describes the surface and subsurface kinetic properties of metal-hydrogen interaction. Hence, it is invaluable for a better understanding and quantitative characterization of the hydrogen embrittlement of metallic materials. In order to elucidate the quantitative power of the I-P-Z model, a brief description of the equations is necessary. The basic I-P-Z model provides the following relationships [50]:

$$i_\infty = (k''/b)(Fk_3)^{-0.5}\sqrt{i_r} \tag{2.4}$$

$$i_c e^{a\alpha\eta} = -(bi_0'/k'')\ i_\infty + i_0' \tag{2.5}$$

$$(k'')^{-1} = (k_{ads}/k_{abs}) + (D_l/k_{abs})(L)^{-1} \tag{2.6}$$

where i_c = cathodic charging flux or current density; i_∞ = steady-state permeation flux; $i_r = i_c - i_\infty$; k" = thickness dependent absorption-adsorption constant; F = Faraday constant = 96,500 coulombs/mole; k_3 = recombination reaction rate constant; a = F/RT = 19.4

$(volts)^{-1}$ at 25^0C; α = transfer coefficient for proton discharged; η (hydrogen overvoltage) = $E_c - E_{eq}$; E_{eq} = equilibrium potential for the h.e. r; b = a constant = L/FD_l ; L = membrane thickness; D_l = lattice diffusivity of hydrogen; $i_0' = i_0/(1-\theta_e)$; i_0 = exchange current density; and θ_e = equilibrium hydrogen surface coverage; k_{ads} = hydrogen adsorption rate constant; k_{abs} = hydrogen absorption rate constant.

By plotting i_∞ vs $\sqrt{i_r}$ and $i_c e^{a\alpha\eta}$ vs i_∞ and performing a regression analysis of Equations (2.4) and (2.5), one can evaluate the kinetic quantities k", k_3, and i_0. Then, by performing a series of hydrogen-permeation experiments for different membrane thicknesses, one can evaluate k_{ads} and k_{abs} utilizing Equation (2.6). By determining the k_{ads} and k_{abs} at different temperatures, it will be possible to evaluate the activation energies of adsorption and absorption of hydrogen atoms into metallic materials. With such independent determinations of the activation energies, one can validate the values of k_{ads} and k_{abs} determined using I-P-Z model [51].

Thus, Pickering and Iyer have probably identified the most important parameters that will help characterize the kinetics of hydrogen entry at the very initial and crucial phase of the interaction of hydrogen atoms with the metal atoms. One potential benefit of knowing the surface and the subsurface thermodynamic and kinetic parameters relating to the metal–hydrogen interaction is if one is concerned about the enhanced hydrogen entry in the presence of poisons such as H_2S or As^{3+}, in the solution. Analyses with the I-P-Z model showed that the presence of H_2S in acidic solutions causes the enhanced entry of hydrogen into iron as a result of an increase in the h.e.r. transfer coefficient, α, and more significantly as a result of a decrease in the hydrogen rate constant, k_3. If it is possible to quantify these aspects, such as by using the I-P-Z model, then one has an attractive means to design the hydrogen–embrittlement resistant and economically attractive alloys.

2.3.2. Hydride Formation at a Crack Tip

As discussed above, the hydrogen embrittlement is governed by complex multiple mechanisms, which are not well established even in a specific material. One useful classification is to distinguish between systems, which form hydrides and those, which do not form hydrides under the relevant hydrogen fugacity and applied stress.

A number of authors [52-55] have shown that embrittlement occurs by the hydride formation at severe stress raisers such as crack tips, followed by cleavage of the brittle hydride [20]. The phenomenon is intermittent, as the crack propagating through the hydride and stopping when it reaches the matrix.

Subsequently, new hydride forms either autocatalytically [55] or as a result of external loading, and then cleavage reinitiates [20]. The stress induce hydride formation is a consequence of the volume dilatation, of the order of 15%, which accompanies hydride [52-54, 56-58]. It has been experimentally shown [53-55] that hydrides form in regions of hydrostatic tensile stresses even at temperatures, which are above the solvus temperature in the absence of stresses. The hydride formation is a result of the enhanced hydrogen concentration in the area of tensile stresses [59] and the decreased chemical potential of the hydride relative to the solid solution in the same stress field [52-54, 57, 58].

In brittle materials, the stress intensity at crack tips has been shown to be changed by phase transformation, which is accompanied by the volume dilatation [60, 61]. Substantial effects of the crack-tip shielding resulting from phase transformation were found for dilatations of the order of 1 % in zones extending approximately 10 microns on either side of a substantially advanced crack [60]. Hence, the precipitated hydrides may mechanically influence the crack tip stress [62] in addition to the material degradation, which results from the hydride's extremely brittle nature [53, 63, 64]. Some evidence for crack-tip shielding as a result of the presence of hydrides has been seen in titanium [55] and zirconium [64].

Mathematical modeling of these phenomena was first carried out by modeling the steady-state-hydride precipitation at a crack-tip and by solving the one-dimensional diffusion equation accounting for the hydrostatic-stress-gradient drifts [65]. The average

growth rate of the hydride was computed, and the crack velocity was equated with the hydride-growth rate. Similar treatments have been given by a number of other authors [64, 66-69]. Ellyin and Wu [70] modeled the hydride effect on the elastoplastic stress field near a crack-tip but the coupled hydrogen diffusion and mechanics phenomena were not treated. Further, Shi et al [71] extended the model of Dutton and [66] on non-steady state conditions in zirconium alloys. The model is a one-dimensional treatment of hydrogen diffusion at a crack-tip in, which the hydride forms in the unperturbed stress field of a crack and grows only along the axis of the symmetry directly ahead of the tip, while its thickness remains constant. The model results indicate that the hydride length increases rapidly with time at first, but eventually reaches a limit, which increases with the bulk hydrogen concentration and applied load. Also at low stress intensities, the model indicates a threshold behavior in hydride cracking, which is dependent on the hydrogen concentration in the bulk.

Lufrano and Sofronis [72] presented an example of the hydride formation at a stationary crack-tip under external stresses in niobium. The hydride precipitation was modeled, assuming an elastic accommodation of the hydrides and was based on a purely dilatant transformation strain upon precipitation [73]. The results shown in Figures 2.4 and 2.5 suggest that when the hydride formation reaches the equilibrium with local stresses, the shape of the hydride zone is self-similar; namely it scales directly with the applied load.

A threshold for the continual crack growth has been predicted, and this threshold is above the fracture toughness of pure hydride and depends on the nominal concentration of hydrogen away from the tip.

Two years later, the same authors [74] re-investigated stress driven diffusion of hydrogen in niobium using more realistic constitutive assumptions. The new model assumed both the elastic and elastoplastic accommodation of the forming hydride and is based on a purely dilatant transformation strain upon the precipitation. To this end, a separate model has been developed to calculate the terminal solid solubility of hydrogen in an elastoplastic matrix. The probabilistic formation of hydrides has been modeled, using the elastic and elastoplastic calculation for the solvus concentration. For the model

using elastoplastic calculation of the solvus concentration, the hydride precipitation has been predicted along lines obliquely aligned to the line of the crack as well as along a line directly in front of the crack. The elastoplastic calculation of the solvus concentration leads to a prediction of a larger hydride zone, compared with the prediction using the standard elastic accommodation arguments. Under a fixed temperature and initial concentration of hydrogen, the profile of the hydride volume fraction is strongly dependent on the applied load and loading rate. The results suggest the autocatalytic hydride growth after the completion of loading.

The formation of hydrides induces the stress relaxation and plastic strain enhancement in the region in front of the crack-tip. Hydrogen-induced stress relaxation at the crack tip has also been demonstrated at high initial hydrogen concentrations and at temperatures for which the formation of hydride is not energetically favorable.

2.3.3. Illustrative Examples: Effects of Hydrogen on Zirconium and Zirconium Alloys

Zirconium alloys were developed for use as nuclear-fuel cladding (amongst other nuclear reactor components) in the early 1950s [75, 76]. Zirconium was chosen for use in the cores of water-cooled nuclear reactors because of its low thermal neutron capture cross-section, reasonable mechanical properties and adequate corrosion resistance in high temperature water [75]. It was initially thought that the poor corrosion resistance of some batches of unalloyed zirconium was a result of stray impurities. However, it was found that improving the purity did not eliminate these problems. The oxidation rate of zirconium was found to vary considerably with grain orientation during the growth of thin, interference-colored, oxide films [77]. This problem was solved by the addition of transition metals (Cr, Fe, Ni) that were largely insoluble in the zirconium matrix and appeared as small particles of intermetallic phases. On the other hand, tin is soluble in zirconium and it annuls the negative effects of the nitrogen impurity [79].Thus, the main advantage of the alloying additions in what were now termed Zircaloy-2 (Zr-2) and Zircaloy-4 (Zr-4) [75] appeared to be the development of a more uniform and thick oxide films.

Hydrogen absorption during corrosion in aqueous environments was one of the earliest observations made during the study of zirconium alloy corrosion. The corrosion of solid-zirconium hydrides in the high-temperature steam has been studied and was found to be higher than that of the unhydrided metal [80]. Observations on reactor fuel cladding that developed solid hydride "lenses" at the outer oxide/metal interface [81] confirm this effect of the presence of solid hydride at the corroding interface.

The studies by Kido [82] showed increased corrosion starting at quite low average hydrogen contents (600-700 ppm) in 360 °C water. However, his micrographs suggested that most of this effect occurred at the edges of the sheet specimens, where the large elongated hydrides lying in the rolling plane emerged at the surface. A group of French researchers [83], reported a study in which sheet specimens, gaseously pre-hydrided, tended to show two types of effects: a small positive increment of weight gain that was independent of hydrogen content up to about the solubility of hydrogen at the test temperature (200 ppm at 400 °C) followed by a roughly linear increase in corrosion weight gain at higher hydrogen contents, Figure 2.6.

The first effect was thought to be a surface contamination effect, although this could not be deliberately replicated. The second suggested that the effect of hydrogen could be directly proportional to hydrogen concentrations above the solubility even in the two phase ($\alpha + \delta$) region. In this work, metallography did not show a significant number of hydrides intersecting the specimen surfaces, but edge effects were not examined in detail. Thus, no clear conclusions can be reached about how to allow for the presence of hydrides other than in the form of solid hydride layers.

Moreover, the effect of hydrogen on mechanical behavior has been widely reported on zirconium alloys, however little research on Zr-4 mainly focuses on the surface investigations. Pierron and co-workers [84] reported the fracture behavior under near plane-strain deformation conditions of Zr-4 sheet containing solid hydride blisters of various depths at 25° and 300 °C. The study was based on material with either blisters having diameters of 2 and 3 mm or a continuous layer of hydrides; in all cases, the substrate material contained discrete hydride precipitates. The fracture strains decrease rapidly with increasing hydride blister/layer depth to levels of about 100 μm deep, and

then remain roughly constant. The material was found somewhat more ductile, if the hydride was in the form of a blister than in the form of a continuous layer (rim). The hydride blisters/layers were brittle at all temperatures, and cracked shortly after yielding of the ductile substrate. At elevated temperatures, the hydride particles within the substrate are quite ductile inhibiting the crack growth. The failure eventually occurs due to a shear instability, Figure 2.7.

Bertolino et al. [85] investigated the influence of the hydrogen content and temperature on the fracture toughness of a Zr-4 commercial alloy. Toughness was measured on compact tension specimens obtained from a rolled material. The specimens were fatigue pre-cracked and hydrogen charged before testing them at different temperatures in the range of 293–473 K. The hydrogen charging produced δ-hydride precipitates, platelet shaped, oriented in planes parallel to the rolling direction, mainly at intergranular sites. The distribution and size of hydrides is are influenced to a great extent by the cooling rate; for slow cooling rates the platelets are grouped in long bands, Figure 2.8.

It was observed that the fracture toughness vbg was influenced by the orientation of the hydrides precipitates. Higher toughness values and fracture mechanisms with more plastic deformation were obtained for the precipitates normal to the crack path than for hydrides parallel to it. Moreover, a correlation between global H content and density of precipitates in the fracture surfaces could be established. Three different cases were identified:

(a) At very low hydrogen contents (as-received material, H < 25 ppm) few $Zr(Fe,Cr)_2$ precipitates were observed on the fracture surface. No hydride phase could be identified in agreement with the concentration value being lower than the terminal solid solubility (TSS).

(b) When the hydrogen content increased, the density of $Zr(Fe,Cr)_2$ precipitates located on the fracture surface also increased. This behavior was observed in hydrogen concentrations up to about 250–350 ppm, strongly suggesting that the precipitates guide the fracture path.

(c) As the observed density of $Zr(Fe,Cr)_2$ precipitates on the fracture surface diminished at higher hydrogen contents, the region occupied by the hydride phase grew, indicating that this brittle phase determined the direction of crack growth and favored the formation of a surface containing a mixed-mode fracture. Macroscopic behavior was still ductile.

2.4. Neutron Diffraction Techniques

There are two basic sources for neutron-scattering materials research: pulsed-neutron sources and steady-state reactors. A primary difference is the spectral character of the neutron beam that strikes the sample. Reactor-based instruments typically use a single, fixed wavelength beam that is selected from a spectrum of wavelength. The intensity is measured over a range of diffraction angles. Pulsed sources, on the other hand, typically use a range of neutron wavelengths. The intensities are measured at a fixed diffraction angle using the time-of-flight (TOF) technique.

Pulsed neutron sources produce neutrons by a process called spallation. High-energy protons strike a heavy metal target such as tungsten or depleted uranium. The spallation event knocks atomic particles out of atoms, producing a wide range of neutron energies or wavelengths that have a wide range of velocities. Thus neutron energies (wavelength) can be distinguished by the time they take to reach the detector. Such instruments are known as time-of-flight instruments. At pulsed neutron sources, a diffraction pattern is recorded over a range of lattice spacings (or wavelengths) and thus many diffraction peaks are recorded simultaneously.

At steady-state research reactors neutrons are produced by controlled nuclear fission. They are designed to produce maximum neutron flux with a minimum heat. A wavelength is selected by diffraction from a crystal that is placed in the reactor beam. Such a crystal is called monochromator because it selects a single wavelength from the reactor beam. Obtaining the wavelength of the beam in this manner leads to a broader range of wavelengths than is the case for x-rays, for which the radiation is produced by sharply defined atomic transition.

When x-ray and neutrons are scattered by a crystal, the periodic array of scattering sites (electrons for x-rays and nuclei for neutrons) leads to directions around the scattering material in which the incoming or incident plane waves scatter "constructively" or in-phase. In these directions, peaks, which are the summations of amplitudes of the incident plane waves scattered by the electrons or nuclei, are observed. The positions, intensities, and shape of these peaks are related to the crystal structure (peak position and intensity) and physical state (peak shape) of the material, as well as the experimental measurement parameters [86].

2.4.1 Phase Studies

2.4.1.1. Generalities

There are two aspects of phase analysis: qualitative and quantitative study.

The qualitative phase study means the identification of the phases that are present in materials and without knowing the quantity. Usually the crystal structures of the phases are already known and available from a database. The primary resource for the identification of unknown phases is the Powder Diffraction File (PDF). Diffraction is a primary means of identifying unknown phases because it provides the structural information which, when combined with element analysis, is often decisive in establishing the identity of phases present in materials systems.

Quantitative phase analysis means that the identity of phases is known but their quantitaties are not, for example, the retained austenite or the production of carbides during a heat treatment. Diffraction is an important method in the determination of the amount of phases present in a multiphase mixture. A number of approaches have been utilized, including the use of ratios of diffraction intensities of the phases present, the addition of known amounts of a reference material, and the generation of reference intensities.

The PDF database contains a great deal of information about the phases represented. However, a relatively new method of the Rietveld profile refinement will have a major impact on new listings in the future and for quantitative phase analyses. The

Rietveld method utilizes the profile intensities of neutron powder patterns to refine crystal structures. This method was developed for neutrons because of the difficulty in growing single crystals sufficiently large to yield practical intensities at neutron sources. The Rietveld or "profile refinement" method, [87] involves fitting the entire diffraction pattern or "profile", using least-square refinement methods. It has had a major impact on structure analyses for new classes of materials such as high-temperature superconductors and high-strength rare earth magnets. The principal fit parameters can be grouped into two categories: instrumental and structural. The instrumental parameters include counter zero, an intensity scale factor, and the half widths of peaks. The structural parameters include atomic coordinates, equipoint occupation numbers, and Debye-Waller temperature factors. The structural parameters characterize the atoms and the crystal structure of the diffracting material [86].

2.4.1.2. Illustrative Examples: Zirconium Alloys

Neutron scattering is the only experimental technique, which allows measurements of the total hydrogen content in any alloy non-destructively. But, more than a simple hydrogen content determination at room temperature, the neutron-scattering technique, when combined use is made of the incoherent background and of the diffraction peaks, is also a very valuable technique. It is quite appropriate to follow *in-situ* the precipitation/dissolution phenomena of hydrides at high temperatures, even for very weak contents of precipitates. The large coherent and incoherent cross-sections of hydrogen, (i.e., σ_H^{incoh} = 80.27 barn while σ_{Zr}^{incoh} =0.02 barn) make this tool very powerful to determine the hydrogen content and characterize the hydrides. Therefore, the incoherent cross-section gives rise to a continuous background in diffraction spectra, which is proportional to the hydrogen content, and is (nearly) independent of scattering angle. The coherent cross-section contributes significantly to the structure factor of the hydride phase, i.e. to the intensity of its diffraction peaks. Thus, by measuring the change of the background signal due to hydrogen incoherent scattering, a very small amount of hydrogen, 2-5 μg/g, in a material can be analyzed [88].

Couvreur et al. [89] determined non-destructively the total amount of incorporated hydrogen with a very good sensitivity and precision (< 20 ppm weight), Figure 2.9. The neutron-diffraction measurements were carried out *in-situ* at various temperatures (between 20 and 500 °C) under secondary vacuum, on a section of Zr-4 cladding tube containing 642 ppm weight hydrogen (length of the sample: 50 mm, diameter: 9.5 mm). One observes the increase of background with the hydrogen content, and the weak diffraction lines of δ-ZrH_2 hydride and a Laves phase. In addition to the total hydrogen content, they were able to obtain simultaneously from the analyses of diffraction spectra in the sample, the hydrogen content in the hydride form, and the crystallographic characterization of the $Zr(Fe, Cr)_2$ and ZrH_2 precipitates, solubility of hydrogen, dissolution of hydrides (Figure 2.10), and influence of hydrogen on the thermal expansion of Zr-4 (Figure 2.11).

Figure 2.10 shows the proportion of hydrogen content in hydride form (δ-phase) versus temperature for a sample containing 642 ppm weight hydrogen. This quantity decreases with increasing temperature. According to the phase diagram shown in the inset, dissolution of the hydrides is complete above 500 °C and the sample is a single-phase Zr-based (α) hexagonal solid solution. It allows to determine the hydrogen solubility curve in the studied material between room temperature and 500 °C, and to deduce a value for the enthalpy of dissolution of the δ-hydrides in Zr-4, $\Delta H = 41.5$ kJ / mol.

Figure 2.11 shows the temperature dependence of the lattice parameter *a* of Zr-4 (sample containing 642 ppm weight hydrogen). A similar curve is found for the lattice parameter *c*. They attributed the increase of slope above 350°C to the dissolution of hydrides, which introduces interstitial hydrogen atoms in the α-Zircaloy matrix and a supplementary swelling. This explanation is confirmed by the observed decrease in lattice parameter during an isothermal stay at 500°C due to hydrogen desorption out of the sample.

At room temperature and above, there are three known crystallographic phases of zirconium hydride [90]: a face-centered tetragonal gamma (γ) phase, a face-centered cubic delta (δ) phase, and another face-centered tetragonal epsilon (ε) phase.

Each crystallographic phase produces a distinct set of diffraction peaks, distributed at scattering angles, which are related to characteristic distances in the crystal lattice. Even though a number of phases contribute peaks to the complete diffraction pattern, one can identify individual peaks that arise from specific hydride phase. The intensity of each individual hydride diffraction peak is proportional to the total volume of hydrides in the neutron beam [91]. The (111) diffraction peaks from these three phases appear at similar scattering angles. The intensity of the (111) diffraction peaks in each phase is also similar (within 5 %) for an equal volume of material, when there are no preferred crystallographic orientations. Neutron diffraction can distinguish the peaks from different hydride phases and therefore offers a unique opportunity to investigate the individual responses of each phase with changes in temperature and thermal history [92].

Recent work has suggested that β-Zr also plays an important role in the hydride precipitation, which could be attributed to the high solubility of hydrogen in β-Zr compared to α-Zr [93]. Therefore, Khatamian and collaborators [94] investigated the structure and orientation of the hydrides formed in β-Zr (Zr-20 wt% Nb), using neutron diffraction. The specimen (~ 10 mm in diameter and ~ 9 mm in length) was cut from a longer Zr- 20 Nb sample charged with gaseous deuterium at 400 °C. Before and after charging with deuterium, the specimen was annealed in vacuum at 850 °C for 1 hour and cooled to room temperature. Chemical analyses revealed the niobium concentration as 19.3 wt%, and the analysis by hot vacuum extraction mass spectrometry indicated a concentration of 1,020 wt. ppm deuterium and 50 wt. ppm hydrogen. The diffraction patterns showed that the intensities of the β-Zr reflections are dependent upon the orientation of the sample. The hydride formed in a specimen of Zr-20 Nb, in which the zirconium is predominately in the β-phase, is orthorhombic in structure and is not consistent with literature that recognizes only tetragonal or cubic symmetries for zirconium hydrides [95]. However, the structure is consistent with a recent orthorhombic structure assigned to the γ-hydride in α-Zr [96] except for distortions in the lattice parameters. Temperature scans have shown that, in β-Zr, there is only one stable hydride structure up to the hydride dissolution temperature. In contrast, hydrides formed within

the α-Zr phase have been observed in two stable structures; γ at low temperatures and δ above ~ 200 °C [92].

2.4.2. Strain Studies

2.4.2.1. Generalities

The use of neutrons diffraction for stress measurements is much more recent than for x-rays, dating from about 1980. For light elements x-rays can provide near-surface depth information and can reveal stresses to hundreds of micrometers. Neutrons are atomic particles with no electric charge, a mass almost 2,000 times greater than an electron. Also neutrons with wavelengths in the range of laboratory x-rays possess much less energy than the x-rays do. These properties make the neutron usage to be complementary to x-rays and extend stress measurements to include macrostresses gradients in components, microstresses in composites and multiphase alloys, and the measurements of bulk averages in, for example, tensile test samples. Furthermore, the high penetration of neutrons, which could be about 1,000 times higher, and low absorption of neutrons allow the use of high- and low- temperature stages and/or environmental chambers because it is much easier to get beams in and out of such devices. Neutrons also offer a better bulk sampling with a defined gauge volumes created using slits or apertures, which enables internal spatial variations (such as, residual stress, texture, and phase variation). Finally, neutron offers identification of elements with low atomic number [86].

2.4.2.2. Macrostresses and Microstresses

The high penetration of thermal neutrons through engineering materials, such as steel, aluminium, or zirconium, makes it possible to measure internal stresses deep inside industrial components non-destructively. Residual stresses are generated, for example, when one region of the sample has been plastically deformed and other regions have been elastically deformed. Tensile residual stresses favor crack propagation and reduce fracture toughness, whereas compressive stresses mitigate against cracks [97]. This can

happen on a macroscopic scale, where regions away from the neutral axis have deformed plastically, and the region near the neutral axis has been deformed elastically. It can also happen on the scale of the grain size, where some grains with particular crystallographic orientations deform plastically under a given stress, whereas others deform elastically.

Although diffraction stress measurements usually refer to the measurement of residual stresses, the respond of materials to the applied stresses may also be measured.

In general, the internal stresses are commonly divided into three categories, or types, by the length scale over which they vary and over which they self-equilibrate, namely: macrostresses or Type I, microstresses or Type II, and Type III [98].

TYPE I stresses self-equilibrate over a length l_o^I, which is comparable to the macroscopic dimension of the structure or part in question. These stresses are typically a consequence of macroscopic misfits generated, for example, by macroscopic plastic deformations. They are assumed to be continuous from grain to grain and even from phase to phase, as illustrated in Figure 2.12.

TYPE II stresses self-equilibrated over a length scale of l_o^{II} comparable to that of the grain structure. They arise from the misfits having a characteristic length scale comparable to the grain size of polycrystalline solids, usually a few tens of microns. Type II stresses are discontinue from grain to grain as shown in Figure 2. 13.

TYPE III stresses self-equilibrate over a length scale l_o^{III}, which is smaller then the characteristics length scale of the microstructure; that is the grain size or the fiber/particle spacing for composite materials. These could be stresses varying within a specific grain, such as crystal defects, with a scale shorter than the grain scale shown in Figure 2.14. The Type III category typically includes stresses due to coherency at interfaces and dislocation stress fields.

Type II and III stresses are also sometimes referred to collectively as microstresses and can vary in the manner shown in Figure 2.15. The sampled gauge of neutron diffraction is usually too coarse to resolve these, so that they generally give rise to diffraction peaks broadening.

2.4.2.3. Measurements of Macrostresses and Microstresses

In general both macro- and micro-stresses are present in a manufactured component. Both type I and II give rise to shifts in the diffraction peaks. In addition, type II stresses also lead to line broadening because the response of different crystal orientations with a given plane normal in a certain direction could vary. Type III stresses contribute to line broadening only [99].

The diffraction methods for stress measurements use interplanar spacings as atomic level "strain gages". The basic measurement is a determination of lattice spacing, d_0, for the (hkl) plane of the crystal via Bragg's law,

$$\lambda = 2d_h \sin\theta_h \tag{2.7}$$

where λ is the known neutron wavelength and $2\theta_h$ is the angle of diffraction. The elastic strain, $\varepsilon_{h,}$ is given by

$$\varepsilon_h = (d_h - d_h^0) / d_h^0 \tag{2.8}$$

where d_h^0 is an appropriate stress-free lattice spacing. The relation between the principal residual stresses, σ_h^i and strains, ε_h^i is given by a generalized Hooke's law.

$$\sigma_h^i = \frac{E_h}{1+\nu_h}\left(\varepsilon_h^i + \frac{\nu_h}{1-2\nu_h}\left(\varepsilon_h^1 + \varepsilon_h^2 + \varepsilon_h^3\right)\right) \tag{2.9}$$

where i = 1, 2, and 3 stand for the principal components, and E_h and ν_h are diffraction elastic constants for the planes of interest.

The diffraction Young's modulus, E_h, is the ratio of an applied macroscopic stress to the strain measured by diffraction in the subset of grains whose plane normals (hkl) lie along the scattering vector. The diffraction elastic constant approach is the standard method of calculating a macroscopic field from the strain, and is generally accurate to within 20% [97].

2.4.2.4. Illustrative Examples: Measurements of Lattice Strain in Steel (fcc) and Zircaloy Alloys (hcp)

An example of measurements of a diffraction elastic constant in an alloy was given by Holden and his collaborators [97]. They carried out the experiments on a ferritic steel sample to measure the elastic constants for the [100], [110], and [111] directions. The diffraction elastic constants were also calculated from the single crystal [100] for pure iron using the method of Kroner [101], which assumes that the grains have a spherical shape and are orientated randomly. Between the experimental diffraction of the bulk elastic constants and the theory calculated for pure iron there is systematic 6 % difference, which is attributed to the intergranular effects that modify the measured strains. The same authors extended the investigation on the polycrystalline zirconium alloy, such as Zr-2. When such an alloy is cooled from the elevated temperatures, a specific grain, if unconstrained, would decrease in a linear dimension along the c-axis according to the coefficient of expansion. However, the grain is constrained by its neighbors in other crystallographic orientations with lower coefficients of expansion so that it cannot decrease the full amount and is left in residual tension. Polycrystalline alloys of zirconium are, thus, never stress-free. A complication associated with the zirconium alloy is that it is impossible to grow single crystals. Consequently direct measurements on single crystals cannot be performed.

Moreover, even if it were possible, the mechanical response of an isolated single crystal is not identical to that of the same crystal embedded in a polycrystalline aggregate and surrounded by grains with different orientations. The use of self-consistent (SC) models allows for the determination of single crystal properties that are characteristic of the behavior of a single grain in the presence of neighboring grains that interact with it under thermo-mechanical treatments. Tome et al. [102] employed an elastic-plastic self-consistent (EPSC) model to calculate the residual strains in the annealed and cold worked Zr-2 specimens and a visco-elastic self-consistent (VESC) polycrystalline model for the simulation of irradiation growth of these specimens. The residual stresses modify the mechanical response and the response under irradiation of the aggregate. Polycrystalline models are tools for predicting these stresses, and

comparison of the predications with experimental measurements provide the information about microstructural deformation mechanisms and properties, such as thermal dilatation coefficients, types of operating slip systems of dislocations, hardening mechanisms, etc. Tome and his collaborators use the elasto-plastic formulation for the interpretation of the measured crystallographic plane spacing, from which they had derived the residual stresses present in the annealed Zr-2. Lattice spacings were measured by neutron or x-ray diffraction, and the strain normal to specific crystallographic planes was calculated with:

$$\varepsilon^{[hkl]} = \left(a^{[hkl]} - a_{sf}^{[hkl]}\right) / a_{sf}^{[hkl]} \tag{2.10}$$

where $a_{sf}^{[hkl]}$ is the stress-free lattice spacing of planes [hkl], and $a^{[hkl]}$ is the actual lattice parameter of a grain in the polycrystalline aggregate, respectively.

As a result of its hcp structure, Zr-2 has only two independent lattice parameters: the prism and basal spacing a_{sf} and c_{sf}, respectively. They vary linearly with temperature when the two independent thermal expansion coefficients, α_a and α_c, are constant. As a consequence, if a_{sf} and c_{sf} are known for a reference temperature T_{sf}, they can be calculated for an arbitrary temperature using:

$$a_{sr}(T) = a_{sf}(T_{sf}) [1 + (T - T_{sf})\alpha_a], \tag{2.11}$$

$$c_{sf}(T) = c_{sf}(T_{sf}) [1 + (T - T_{sf})\alpha_c] \tag{2.12}$$

It was assumed that there is a temperature, T_{sf}, at which the aggregate is free of internal stresses and that the values of the thermal expansion coefficients are known. Then using the Equations (2.11) and (2.12) to find a_{sf}, c_{sf}, and T_{sf} which best fit the experimental data for this set of thermal coefficients. After such a fit, strains were calculated from measured lattice spacings using Equation (2.10). The result of the calculation is represented in Figure 2.16(a) for a particular set of thermal coefficients. Next, the cooling of the aggregate from T_{sf} to room temperature was simulated, after the orientations that could contribute to the experimental diffraction peak were identified, and consequently plot the average strain in the corresponding crystallographic planes as a function of temperature. Only the thermal coefficients and not the lattice parameters are required in the calculation and the result is shown in Figure 2.16(b). Repeating this procedure for different thermal coefficients, it was possible to find a set of values that

minimizes the difference between the predicted strains and the ones calculated from the measured lattice spacings. This application illustrates how SC models can be used to determine single crystal parameters from polycrystalline measurements. The EPSC model gives a very good description of the residual and *in-situ* strains in Zr-2, as well as the macroscopic stress-strain [102].

Later, Clausen et al. [103] reported on applied and residual lattice strains determined with neutron diffraction during a tensile test in a weakly textured austenitic stainless steel and compared them to the predictions of a self-consistent polycrystal deformation model. The *in-situ* lattice strains parallel and perpendicular to the tensile axis are presented in Figure 2.17. The measured and calculated elastic lattice strains are shown as a function of the applied stress. The comparison between the model and experimental measurement is simple to make due to the similarities for some of the assumptions in the modeling scheme and the characteristics of the neutron diffraction measurements. The dotted horizontal lines in Figure 2.17 at an applied load of 265 MPa marks the macroscopic 0.2% offset yield stress. It can be seen that the non-linear behavior of the lattice strain response starts before the macroscopic yield for most of the reflections. It appears that the 'truly' elastic regime before the reflections starts to show deviations from the linearity in the applied stress versus elastic lattice strain plot, extends only to about 200 MPa. It also can be seen in Figure 2.17 that the development of lattice strains is very non-linear once the specimen enters the plastic regime. As grain sub-sets become plastic, they do not accumulate elastic load at the same rate as when they were elastic, causing changes in the partitioning of an incremental load increase between the different grain orientations. The model predictions show a similar result.

Therefore, the comparison between neutron diffraction measurements and predictions of a self-consistent model had shown that the model predictions of the lattice strains under load show agreement with experiments to within the measurement accuracy of 150 x 10^{-6}. The residual lattice strains for both directions (parallel and perpendicular) generally show poorer agreement between model predictions and measurements than the lattice strains determined under load. The explanation for the poorer agreement may

derive from the fact that the used self-consistent model does not predict slip during unloading.

J. Smith et al [104] investigated the effect of fatigue pre-cracking stress intensity and monotonic loading on residual elastic strains and plastic deformation near the crack tips in compact-tension AISI 4340 steel specimens using neutron diffraction. Diffraction peak broadening, which correlates with extent of plastic deformation, was also measured near the cracks. Fracture toughness testing focuses on crack extension under plane strain conditions, which occurs in the middle thickness region of the specimen. The residual stresses in this region may be determined by measuring the stress-induced elastic strains using neutron diffraction. Figure 2.18 shows the configuration of the specimen for the strain measurements parallel to the loading directions near the crack-tip. This configuration was chosen to minimize the path length of neutrons through the material for measurement of strains in this direction, since absorption of neutrons increases exponentially with path length. The strain in the direction of the scattering vector can be determined by measuring the shift of the Bragg peak angular position relative to the unstrained condition.

Figure 2.19 shows the residual strains, $\varepsilon_{(110)}$, determined from (110) peak shifts in the plane of the crack. The mono-load specimens show maximum compressive strains within a distance of 1 mm from the crack-tip. Further from the crack tip, the strains rapidly become tensile, reaching a maximum at approximately 5 mm and then decreasing as the distance from the crack tip increases. The increase in the fatigue precracking stress intensity slightly increased the residual compressive strains at the monotonically loaded crack tips. Plastic-zone sizes extending from the monotonically loaded cracks were determined from residual elastic strain distributions and peak broadening. The results agreed with theoretically predicted plastic zone sizes. The effect of monotonic loading dominated over fatigue precracking in creating the plastic deformation.

Chapter 3

Experimental Approaches

3.1. Materials, Specimen Preparation, and Mechanical Testing

3.1.1. Material

Experiments were conducted on specimens of Zr-4, a zirconium alloy. The chemical composition (weight percent, wt. %) of the as-received Zr-4 is 1.4 Sn, 0.2 Fe, 0.1 Cr, and balance Zr. The oxygen content was 0.12 % by weight, Table 1.

Figure 3.1 shows the Zr-Sn binary alloy phase diagram [105]. The material fabrication reportedly includes: forging a slab, pre-heating the slab to hot rolling in the α-Zr – β-Zr two phases region, followed by hot rolling, air cooling then preheating in all β-phase, water quenching and air annealing in α-phase region. The slab was then blast cleaned, pickle cleaned, and machined to size [106].

For mechanical testing, two different specimen geometries were prepared: namely round-bar tensile specimens and compact-tension (CT) specimens.

TABLE 3.1 Chemical Composition of Zr-4 Alloy.

Element	Zr	Sn	Fe	Cr	O
Weight %	98.18**	1.4	0.2	0.1	0.12

** As balance

3.1.2. Tension Specimens

Figure 3.2(a) shows a drawing of the threaded-end round-bar tensile specimens, with a nominal gauge diameter of 8 mm and gauge length of 42 mm. The tensile specimens were used for macroscopic (bulk) and microscopic (lattice) strain measurements. The macrostrain, Type I strain, is obtained by attaching an extensometer to the tensile specimen, Figure 3.2(b). Figure 3.2(c) illustrates a typical macroscopic stress-strain curve. The microstrain, Type II strain, is obtained using neutron diffraction techniques. Figure 3.2(d) shows a typical lattice strain behavior under an applied load. In addition, the tensile specimens were charged with hydrogen gas to investigate the interaction between Zr-4 and hydrogen (e.g., zirconium hydride formation and distribution) in the bulk.

3.1.3. Fatigue Specimens

All CT specimens were designed in accordance with the American Society for Testing and Materials (ASTM) Standard E647–86 [107] with a width of 60.85 mm, length of 63.4 mm, and a thickness of 6.4 mm, Figure 3.3(a). The specimens were pre-cracked by fatigue loading in air, to crack length of 22.86 mm, using a servo-hydraulic Material Test System (MTS) testing machine interfaced with a Teststar IIs controller. Fatigue pre-cracking was performed under an increasing stress-intensity-factor range (K) control mode with a frequency of 10 Hz and a constant load ratio, R = 0.1. The maximum stress intensity, K_{max}, can be calculated using [108]:

$$K_{\max} = \frac{P_{\max}(2+\alpha)}{B\sqrt{W}(1-\alpha)^{3/2}}\left(0.886 + 4.64\alpha - 13.32\alpha^2 + 14.72\alpha^3 - 5.6\alpha^4\right) \qquad (3.1)$$

where P is the load, $\alpha = a/W$; a is the total crack length; W is the specimen width, and B is the specimen thickness. Test data were recorded periodically using a computer data-acquisition system. Crack length was measured by the crack-opening-displacement (COD) gauge using the unloading-compliance [109].

The CT specimens were used to investigate the localized strain and the hydride distribution around of the crack tip. Using a crack opening displacement (COD) gage

attached to the CT specimen, Figure 3.3(b), the fatigue behavior is obtained by plotting the fatigue crack growth rate (da/dN) as a function of stress intensity factor range (Δ K), Figure 3.3(c). The neutron diffraction experiments allow the measurements of Type I (bulk) and Type II (localized) strains around the crack-tip, Figures 3.3(d) and (e), respectively [110].

3.1.4. Correlation Between Tension and Fatigue

The correlation between the tension and fatigue specimens is presented in Figure 3.4 [111], where A is a tensile specimen and B is a CT specimen. The tensile specimens provide the macroscopic and homogeneous behavior of Zr-4, while the CT specimens allow the investigation of the localized strain gradient around the crack tip. Furthermore, data from these two specimen geometries allow us to study the interaction between the Type I and Type II strains around a crack tip in the plastically anisotropic Zr-4.

3.2. Hydrogen Charging

To charge specimens with hydrogen two methods were employed: an electrochemical cathodic charging and gaseous charging. In particular, the gas-charging technique simulates the operation environments of the zirconium alloy components in the nuclear reactor, i.e., the combination of temperature and hydrogen intake.

3.2.1. Electrochemical Charging

The surface of CT specimen was coated with an epoxy layer except an area of approximate 25 x 4 mm^2 along the fatigue crack, on both faces of the specimen; to ensure the hydrogen intake around the crack tip, Figure 3.5(a). A cell, consisted of the electrolyte, the Zr-4 sample (working electrode), a saturated calomel reference electrode (SCE), and a platinum counter electrode, was employed, to produce an electrochemical-hydrogen charged specimen, Figure 3.5(b). The electrolyte is a solution of 0.6 M sodium chloride (NaCl) and sulfuric acid (H_2SO_4) at pH = 2. Only the bottom half of the CT specimen was immersed in the charging solution, such that 2 mm of the crack was in the

solution, Figure 3.5(c). The specimen was charged with hydrogen for 4 hours at room temperature by holding the voltage at -2.5 V. The voltage used in this technique combined with the selected pH, allows the development of an oxide-free surface on the zirconium sample. During the charging a 263A Potentiostat/Galvanostat (Princeton Applied Research, Oak Ridge, TN) and PowerCorr Software were used to accurately control the voltage.

3.2.2. Gaseous Charging

Using a 12.5 vol. % hydrogen in argon mixture two round-bar tensile specimens were charged with hydrogen in a tube furnace at 430 °C under 13.8 kPa for 1/2 hour and 1 hour, respectively, using the setup shown in Figure 3.6. To promote the hydrogenation process, the Zr-4 specimens were coated with a Ni layer with a thickness of 0.15 μm, which dissociates the molecular H_2 to atomic H, $H_2 \xrightarrow{Ni} 2\ H$.

Note that the transitional metals have as a typical common feature among them, the presences of *d* electrons, and/or their unfilled *d* orbitals. As a result, transition metals form compounds of variable oxidation states. Thus, these metals are *electron banks* that lend out electrons at appropriate time, and store them for chemical species at other times. When hydrogen is absorbed by nickel, H_2 dissociates on Ni and the chemisorbed H is stable up to the room temperature. The breakage of the H-H bond is facilitated by a series of steps:

2 Ni + H_2 --->2 Ni...H_2----> 2 Ni-H
solid gas physisorption chemisorption

The chemisorption strength also varies with the metals, decreases for transition metals in a period as the atomic number increases [112].

Before Ni layer was applied, specimens were cleaned in acetone with a soft paper wipe according with the American Society for Testing and Materials (ASTM) Standard G2-88 procedure [113]. Each specimen was charged individually, by placing it in the tube furnace below an internal thermocouple. First, using the pressure regulator at the end of the tube, the pressure was fixed at 13.8 kPa. Keeping a flow rate constant at 8 cc/min, the gas mixture was flown through the alumina tube for 15 minutes to ensure an

oxygen free atmosphere. Then, the temperature was increased from room temperature to 430 °C, Figure 3.7. After the initial fluctuation of temperature (between 450 °C and 380 °C) for about 15 minutes, the thermocouple showed a constant temperature of 430 °C ± 1 °C. Subsequently, the specimens were charged for ½ hour and 1 hour, respectively. Then, the temperature and hydrogen gas flow were turned off and the samples removed from the furnace [114].

3.3. Metallography

Each specimen was examined by optical microscopy and scanning-electron microscopy (SEM) to study the microstructure (e.g., grain size and hydride distribution), chemical composition, and fracture surface.

Sample preparation is a critical part of a metallographic investigation. Mounting of specimens is usually necessary to allow them to be handled easily. It also minimizes the amount of damage likely to be caused to the specimen itself. Figure 3.8 shows a schematic of a specimen mounted in cold-setting epoxy. Mounted specimens were ground with rotating discs of abrasive paper. The grinding procedure involves several stages, using a finer paper (higher grit) each time, starting from 420 grit paper and finishing with 1200. Each grinding stage removes the scratches from the previous coarser paper. Between each grade the specimen was washed thoroughly with water to prevent contamination from coarser grit present on the specimen surface. Then polishing discs were covered with soft cloth impregnated with abrasive diamond particles and an oily lubricant. To enhance the contrast along the grains, each specimen was etched by immersing it in a solution of 45 ml nitric acid (HNO_3), 0.5 ml hydrofluoric acid (HF), and 50 ml water (H_2O).

3.3.1. Optical Microscopy

The macro- and micro-structures were investigated, using an optical microscope. First, an as-received Zr-4 sample (with the surface polished and etched) was investigated under an optical microscope with polarized light to determine the grain size. Then, the polished and etched cross-sectional surface of the specimen charged with

hydrogen gas for 1 hour was investigated for the hydride phase distribution through the thickness. The same type of study was conducted on a cross-section of a specimen electrochemically charged with hydrogen, to examine the phase distribution near the crack tip as shown in Figure 3.9. Areas (1) and (2) are close to each edge of the specimen and near the crack tip. Finally, using an optical microscope with a digital camera attached, a macroscopic study was performed on the fracture surface of the specimen charged with hydrogen gas for one hour. These images were compared with those obtained from the as-received specimen.

3.3.2. Scanning Electron Microscopy (SEM)

The fracture surfaces of specimens in as-received and hydrogen-gas charged conditions were investigated, using a Leo 1526 scanning-electron microscope (SEM). Images were taken at different positions through the thickness to examine the distribution of the hydride phase as shown in Figure 3.10, where area (1) is by the center of the specimen, area (2) is between center and edge, and area (3) is near its surface. The same areas were investigated on the as-received specimen, as well. In addition, the chemical composition of the specimens was examined, using a Leo 1526 scanning-electron microscope using the energy-dispersive spectroscopy (EDS).

3.4. X-ray Diffraction

X-ray diffraction measurements were performed, using Philips X'Pert x-ray Diffractometer at the University of Tennessee, on the samples charged with hydrogen (gaseous and electrochemical) for qualitative phase identification. Absolute scans were conducted in a 2θ range of 20° to 120°, with CuKα radiation (λ = 1.542 Å), 5-mm mask (which gives a beam size of 1 mm x 5 mm), 0.05°step size, and 20 sec/step scan rate.

In addition, a Rotating Anode x-ray Tube was used to investigate the surface of the electrochemically-charged specimen for phase identification and distribution around the crack tip, Figure 3.11(a). Measurements were performed at Los Alamos Neutron Science Center (LANSCE) in a Bragg Brentano geometry with CuKα radiation (λ = 1.542 Å), 0.05° step size, 20 sec/step scan rate, and 2.0-mm spot size. Diffraction patterns

were collected at 1 mm intervals, starting from the bottom of the notch and going towards the crack tip and beyond for a total length of 30 mm, Figure 3.11(b).

3.5. Neutron Scattering Techniques

There are two basic sources for neutron scattering research, steady-state reactors and pulsed-neutron sources. A primary difference is the spectral character of the neutron beam that strikes the sample. Reactors supply a single, fixed wavelength beam that is selected from a spectrum of wavelength and which is measured over range of diffraction angles. Pulsed sources, on the other hand, contain a range of neutron wavelengths. This spectrum is measured at a fixed diffraction angle by determining the intensity of neutrons of various wavelengths.

3.5.1. Pulsed Neutron Sources – Phase and Strain Mapping

Phase and strain measurements were conducted at two pulsed neutron facilities: ISIS, Rutherford Appleton Laboratory, UK, using ENGIN-X instrument [115]; and at the Manuel Lujan Jr. Neutron Scattering Center, Los Alamos National Laboratory, using SMARTS (Spectrometer for Materials Research at Temperature and Stress) instrument [116].

3.5.1.1. ENGIN-X Instrument: Tensile Behavior

Qualitative bulk phase mapping and intergranular strain measurements were performed on one as-received and two hydrogen-gas charged round-bar tensile specimens, using the ENGIN-X instrument.

The setup shown in Figure 3.12(a) was employed to identify the phases present in the hydrogenated Zr-4 and to study the hydride distribution in the bulk. Measurements were conducted using an incident and diffracted beam widths of 2 mm and the height of 9 mm, which gives a gauge volume of 2 x 9 x 2 mm^3, Figure 3.12(b). Mapping measurements were performed at intervals of 1 mm across the diameter of the sample, as shown in Figure 3.12(c), on all three tensile specimens and the neutron diffraction data were recorded in the two detectors available at ENGIN-X. Phase identification and

distribution through the thickness was investigated by Rietveld analyses [87] of the entire diffraction profile, using GSAS (General Structure Analysis System) [117]. Furthermore, several individual reflections were examined by Single Peak Fitting [115].

In addition to the phase study, a series of *in-situ* uniaxial tensile loads were applied sequentially to each tensile specimen. The strain measurements setup is shown in Figures 3.13(a) and (b). The gage volume employed for this study was defined by 4 mm incident and diffracted beam widths and 8 mm tall. The loading axis is horizontal at 45° to the incident beam, allowing simultaneous measurements of lattice-plane spacings (d-spacing) both parallel (axial direction) and perpendicular (transversal direction) to the loading direction in the opposing 90° detector banks, Figure 3.13(c) and Figure 3.13(d), respectively. Software control of the load frame was carried out through LabView on a standard PC, which allowed interfacing of neutron and stress aspects of the measurements [118]. The tests were carried out under constant load control at 15-MPa increments. Bulk strain was monitored on the samples using a dynamic extensometer clip gauge. The lattice parameters of the hexagonal-close-packed Zr-4 were obtained by Rietveld analyses of the measured diffraction patterns, using GSAS (General Structural Analysis System). The lattice strains, ε, were determined at each load, using:

$$\varepsilon = (a_i - a_0) / a_0 \tag{3.2}$$

where a_i and a_0 are the lattice parameters of the strained and unstrained conditions, respectively.

Furthermore, the d-spacing for several individual reflections were obtained at each load by Single Peak Fitting and strain for these reflections, ε_{hkl}, was calculated using:

$$\varepsilon_{hkl} = (d_i - d_0) / d_0 \tag{3.3}$$

where d_i and d_0 are the d-spacing parameters of the strained and unstrained conditions, respectively [119].

3.5.1.2. SMARTS Instrument: Fatigue Behavior

Qualitative bulk phase mapping and strain measurements were performed on one as-received and one hydrogen-electrochemical charged fatigue pre-cracked CT specimens, using SMARTS instrument.

A picture of the CT specimen mounted for the phase study is shown in Figure 3.14(a). Figure 3.14(b) illustrates a schematic of the specimen configuration used to investigate the phases present in the hydrogenated Zr-4 and the hydrides distribution around the crack tip. The phase mapping measurements were performed, using an incident and diffracted beam widths of 2 mm and height of 20 mm, which gives a gauge volume of 2 x 20 x 2 mm^3 and were conducted through the thickness of the CT specimen at 1 mm intervals. The phase identification was obtained by Rietveld analyses of the entire diffraction profile, using GSAS (General Structure Analysis System).

The elastic lattice strains in the CT specimens were measured *in-situ* with neutron diffraction to determine the strain distribution around the crack tip, Figures 3.15(a) and (b). The diffraction gauge volume was defined by 2-mm incident and diffracted beam widths and 1-mm height along the crack length in the center of the specimen. Figure 3.15(c) shows the neutron measurements at the crack-tip region for in-plane (IP - parallel to the loading direction) and through-thickness (TT – perpendicular to the loading direction) strain components. Strain mapping was conducted at 1-mm intervals along the crack, starting from 3 mm behind of the crack tip and finishing at 17 mm in front of the crack tip, Figure 3.15(d). About 30-minute counting time was used for each diffraction measurement point. The *in-situ* spatially-resolved lattice strain measurements along the crack length were performed on CT specimens at two different applied loads of 667 N and 4,444 N, using the load frame available on the SMARTS instrument. Bulk strain was monitored on the samples using a crack opening displacement (COD) gage. The lattice parameters of the hexagonal-close-packed Zr-4 were obtained by Rietveld analyses of the measured diffraction patterns, using GSAS (General Analysis System). Similarly, the lattice strains, ε, were determined at each measurement position, using Equation (3.2). The lattice strain free, a_0, was measured at

25 mm away of the crack, as shown in Figure 3.15(a) for each sample condition and for each stress level applied. Furthermore, the d-spacing for several individual reflections were obtained at each neutron measurement position by Single Peak Fitting and strain for these reflections, ε_{hkl}, was calculated using Equation (3.3) [110].

3.5.2. Steady State Research Sources - Incoherent Neutron Scattering

The quasielastic neutron scattering measurements were performed on the tensile bars charged with hydrogen-gas, using the fixed-incident energy triple-axis spectrometer, HB1A, operated by the Ames Laboratory at the High Flux Isotope Reactor (HFIR) at the Oak Ridge National Laboratory (ORNL) [123]. In neutron scattering experiments the hydrogen incoherent scattering can be a major source of background signal, thus measurements of background could provide reliable information of the hydrogen content in the specimen.

The assessment of the background scattering due to the elastic incoherent process was carried out by performing inelastic scans (energy scans) around the zero energy transfer. The inelastically scattered neutrons are discriminated and one can obtain, within the instrumental resolution, the purely elastic contribution to the background. Figure 3.16 (a) shows a picture of a specimen with polypropylene foils mounted in the front of the neutron beam and Figure 3.16(b) shows the setup of the incoherent measurements with the neutron beam size defined by masks, placed in front and behind the samples with the sizes of 30 mm height x 16 mm width and 35 mm height x 21 mm width, respectively.

To determine the relative amount of hydrogen in the Zr-4 samples, we calibrated the increase of the incoherent scattering with the hydrogen content, using standard samples for which the hydrogen content was known. A polypropylene film with a thickness of 0.02 mm was cut into several sheets in a size of 40 mm x 50 mm. These sheets in sets of three were successively wrapped around a Zr-4 specimen in as-received condition.

The amount of the hydrogen in each sheet was calculated from its weight. Neutron energy scans were performed on each set of polypropylene sheets in an energy

range from -1.5 meV to 1.5 meV, with a step of 0.2 meV, and a counting time of 60 seconds per point. Moreover, “incoherent scans”, were taken at a fixed two-theta value (2θ = 62 deg) from an angular range with flat background such that no coherent scattering is present.

Similarly, inelastic scans were carried out on the round-bar tensile specimens charged with hydrogen gas.

Chapter 4

Results and Discussion

4.1. Macro and Microstructures

4.1.1. As-received

The microstructure of the Zr-4 alloy consists of a single phase α-Zr (hexagonal-closed-packed, hcp, structure) with a random texture, and grains size with a mean diameter of approximately 700 μm, Figure 4.1. Scanning-electron microscopy with the energy-dispersive spectroscopy (EDS) indicates an homogenous chemical composition throughout the alloy. Figure 4.2(a) shows an optical image, (a side view), of the fractured tensile specimen in the as-received condition after a tensile test. A ductile behavior was observed by a reduction in the diameter of the specimen. The cross section of the fracture surface is shown in Figure 4.2(b). Figure 4.3 represents an example of a SEM fracture surface taken at the center of the cross section of the same specimen. A uniform ductile fracture throughout the cross section of the specimen was observed, showing dimples associated with ductile metallic ligaments.

4.1.2 Electro-chemically Charged

Figure 4.4 illustrates an example of an optical micrograph taken near the edge of the cross-section of the CT specimen electrochemically charged with hydrogen for four hours. Details of the specimen preparation and the measurements were given in Section 3.2 and 3.3, respectively. A microstructure similar to the as-received specimen was observed and no traces of hydrides could be identified using optical microscope.

4.1.3 Gas-charged

½ hour-charged specimen

Figure 4.5(a) represents an optical image, (a side view), of the fractured tensile specimen charged with hydrogen for 30 minutes. The sample does not show an obvious

reduction in the diameter. A thin layer of a brittle phase had been cleaved off from the surface of the specimen. The fracture surface of the same specimen is shown in Figure 4.5(b) where the remaining thin layer of the brittle phase is visible in a ring shape.

1 hour-charged specimen

The macroscopic investigation of the fracture surface of a specimen charged with hydrogen gas for one hour shows a thicker layer of the brittle phase, with a ring shape, on the surface of the specimen, Figure 4.6 (a). The dotted lines represent the outer and inner edges of the hydride layer. Note that this brittle phase layer is identified as zirconium hydride and the details will be discussed in the following sections. A closer inspection of the specimen reveals that this layer has a thickness of approximately 400 μm. Figure 4.6 (b) shows an optical micrograph of the polished and etched surface of a similar specimen, charged with hydrogen for one hour under the same conditions as previous sample. The hydride layer appears in the same ring shape and thickness. Within the layer one can observe cracks, which could be attributed to the residual stresses and brittle nature of the hydride phase. In Figure 4.6(c) is a magnified image of the hydride layer with more visible cracks shown. This hydride layer eventually cleaves from the specimen surface under an applied load, illustrating a typical structural damage of zircaloys in corrosive environments.

The fractographic observations of the specimen charged with hydrogen for 1 hour exhibits the influence of the hydride precipitates on the fracture path. The measurement positions are illustrated in Figure 3.10. Figure 4.7(a) shows a SEM image of an area near the center of the specimen (area 1) charged with hydrogen for one hour. A ductile fracture with dimples associated with ductile metallic ligaments around its center can be seen. In Figure 4.7(b), some brittle regions can be observed between the center and edge of the specimen (area 2). Near the surface, (area 3) as hydrogen (hydride) content increases, large brittle regions are more frequently observed, Figure 4.7(c).

While the as-received specimen exhibits a uniform ductile behavior, the hydrogenated specimen is ductile only around its center and brittle regions were observed near the surface of the specimen. Grange et al. [120] and Bertolino et al. [121] reported a

similar dependence of the fracture mechanisms on the hydrogen content in hydrided Zr-4. They observed that for a low hydrogen content, the ductile fracture occurs by the formation and growth of voids. For the area with high hydrogen content, brittle areas appeared, indicating fracture through hydrides.

4.2. Phase Studies Using Diffraction Techniques

4.2.1. As-received Condition

Figure 4.8 shows an example of a neutron diffraction pattern, intensity versus d-spacing, of Zr-4 alloy in as-received condition. This pattern was obtained at 1 mm distance from the surface of the specimen using the ENGIN-X instrument. The measured diffraction pattern (red circles) was fitted by Rietveld analyses, using GSAS (General Structure Analysis System) (continuous black line). Only a single phase corresponding to hcp α-Zr was observed. Within the d-spacing range observed the Zr reflections identified were the followings: Zr (100), Zr (002), Zr (101), Zr (102), Zr (110), Zr (103), Zr (200), Zr (112), Zr (201), Zr (004), Zr (202), as it can be seen in Figure 4.8.

In summary, Zr-4 alloy in the as-received condition contains a single phase corresponding to α-Zr. The α-Zr matrix has a hexagonal-closed-packed (hcp) crystallographic structure at room temperature, with a typical lattice parameters of a = 3.2364 Å and c = 5.1689 Å, c/a ratio = 1.597 and space group of P63/m m c.

4.2.2. Electrochemical Hydrogen Charged Condition

4.2.2.1. Surface Study

Figure 4.9 shows x-ray diffraction patterns, intensity versus 2 theta, obtained at the surface of a CT specimen in as-received condition, using the rotating anode x-ray diffractometer at Los Alamos National Laboratory. These diffraction patterns were taken at different measurement positions relative to the crack tip (shown on the right side of the graph), as illustrated before in Figure 3.11(b). The green arrow marks for the position of the crack tip (position “0”). Only α-Zr phase was observed in all positions. Within the 2

theta range employed, three Zr reflections were identified, namely Zr (100), Zr (002), and Zr (101).

Figure 4.10 shows x-ray diffraction patterns, intensity versus 2 theta, obtain at the surface of the CT specimen electrochemically charged with hydrogen, using the rotating anode x-ray diffractometer at Los Alamos National Laboratory. These diffraction patterns were taken at different measurement positions relative to the crack tip and the level of the charging solution. The numbers on the right side of the graph represent measurement points, as illustrated before in Figure 3.11(b). The green arrow marks the position of the crack tip and the red dotted arrow marks the level of the charging solution, which is at 2 mm behind the crack tip. By indexing the peaks present in the diffraction pattern it was observed the presence of two phases. Using the PowderCell, fitting program [124], these two phases were identified as α-Zr and delta (δ) zirconium hydride (ZrH_2). Therefore, within the 2 theta range examined in this study the following reflections were identified: Zr (100), ZrH_2 (111), Zr (002), Zr (101), and ZrH_2 (200). It also shows the evolution of zirconium hydride phase as a function of the distance from the charging solution level. First the ZrH_2 (111) peak starts to show at around 6 mm behind the crack tip and 4 mm above the solution line, and its intensity dramatically increases as the solution line is approached. When the charging solution level is reached, the hydride (111) peak intensity overwhelms the Zr (100) peak and a second hydride peak, ZrH_2 (200) appears at the shoulder of Zr (101) peak. Figure 4.11 shows the variations of the intensities of Zr (002), Zr (101), and ZrH_2 (111) peaks as a function of the location relative to the charging solution line and crack-tip. The red dotted line stands for the charging solution line and the continuous black line is the crack tip. The intensities of the Zr (002) and (101) peaks decrease close to the solution line and crack tip position while the intensity of the ZrH_2 (111) peak increases. The formation of hydrides above the solution line is useful information for the development of *in-situ* experiments, which will allow the measurement of the hydrides formation.

4.2.2.2. Bulk Study

Figure 4.12 shows a typical neutron diffraction pattern of the CT specimen electrochemically charged with hydrogen. This pattern was obtained from the middle of the thickness using the SMARTS instrument. Only one phase corresponding to α–Zr was observed at various measurement positions (illustrated in Figure 3.14). Within the d-spacing range observed the Zr (100), Zr (002), Zr (101) reflections were identified. Thus, no zirconium hydrides were observed through the thickness of the specimen. In addition, the background of diffraction patterns from different measurement positions were compared with one obtained from the as-received specimen. No changes in the background due to the hydrogen incoherent scattering were observed. Therefore, the CT specimen electrochemically charged with hydrogen showed hydrides only on the surface. A possible explanation for the presence of zirconium hydrides only on the surface of the specimen is the absence of the "poisons", H_2S or As_2O_3 [51], which prevent the hydrogen ion (H^+) resulted form the chatodic process to recombine to hydrogen molecular (H_2) gas which leaves the system instead of diffusing through the material.

4.2.3. Gas Hydrogen Charged Condition

4.2.3.1. Qualitative Bulk Study

An example of a neutron diffraction pattern from a tensile specimen charged with hydrogen gas for one hour is shown in Figure 4.13. This pattern was obtained at 1 mm from the surface using the ENGIN-X instrument. Details of the instrument and the experimental setup were given in Section 3.5.1. The measured diffraction pattern (red circles) was fitted by Rietveld analyses using the General Structure Analysis System (GSAS) (continuous black line), and two phases were identified, corresponding to α-Zr and zirconium hydride. From the fitted data, one can observe two ZrH_2 peaks, which were identified as ZrH_2 (111) and ZrH_2 (200). It is worth noting that the reflections corresponding to the δ-ZrH_2 are broad, most likely due to the hydrogen disorder. From the crystallographic point of view, the zirconium hydride has the face-centered-cubic

delta (δ)-ZrH_2 structure with the space group of F m -3 m and lattice parameter, a = b = c = 4.785 Å.

In the gas hydrogenated specimens (both 30 minutes and 1 hour), the presence of the hydrogen was identified in the hydride form. The variation of the hydride peak intensities across the diameter of the specimen is shown in Figure 4.14(a) for δ-ZrH_2 (200) and (b) for ZrH_2 (111). The intensity of δ-ZrH_2 peaks increases dramatically near the surface. It is worth noting that the through-thickness mapping measurements provide reliable information of the hydride location in the samples [92]. The neutron diffraction analysis suggests that the intensity of the hydrides is distributed near the surface to an average depth of about 2 mm, Figure 4.14, whereas the macroscopic study showed a layer of approximately 0.4 mm, Figure 4.6(a). This discrepancy is due to the large size of the gauge volume employed in this experiment (V = 2 x 9 x 2 mm^3, Figure 3.12 (c)) compared to the thickness of the hydride layer. Nevertheless, the neutron results qualitatively illustrate the distribution of the hydride layer which is consistent with the macroscopic observation. Moreover, the variation of the intensity of δ-ZrH_2 peaks is approximately similar across the diameter. However, some positions in the 30-minute case exhibit higher intensities than the 1-hour case. This trend could be attributed to the experimental setup, in which a large scattering volume was used to map small volume of specimen with possible irregular surface hydride layer thickness.

In this qualitative phase mapping study we were able to clearly identify the presence of hydrogen in the hydride form however the existence of hydrogen in the solution is more difficult to distinguish. Figure 4.15 illustrates a simple comparison of diffraction patterns, intensity versus d-spacing, obtained from the as-received specimen, 30-minute and one-hour charged specimens. These diffraction patterns were collected at similar location (1 mm from the surface) from each sample and with the same counting time (45 minutes). The comparison reveals a significant increase in the background for the charged samples due to hydrogen incoherent scattering. Moreover, the background for the one-hour charged specimen is the highest among them due to its enhanced incoherent scattering cross-section. Similarly, the 30-minute charged specimen exhibits an increased background with respect to the specimen without hydrogen but, as expected,

less than the specimen charged for one hour. In addition, a systematic increase in zirconium hydride peak intensity was observed with the increase in the charging time.

Furthermore, the through-thickness mapping reveals measurable changes in the background at different measurement points. Figure 4.16 shows the sum of counts as a function of the measurement positions across the diameter of the specimen. While the as received specimen shows a flat background across the diameter, the hydrogen-charged samples shows a significant increase in background near the surface. The position dependence of the variation of the scattered background is consistent with the intensity variation of zirconium hydride peaks shown in Figure 4.14.

4.2.3.2. Quantitative Study

Diffraction measurements have been carried out using the HB1A triple-axis spectrometer in the elastic configuration on Zr-4 specimens in the as-received and hydrogen-charged conditions. Details of the instrument and the experimental setup were given in Section 3.5.2. As presented in Figure 4.17, these measurements confirmed the presence of hydrogen in the sample in the form of δ-ZrH_2 of which intensities increased systematically with the increase in the charging time Due to the effect of the large incoherent scattering from the hydrogen, the backgrounds of the diffraction patterns exhibited a systematic and significant increase with respect to the specimen in the as-received condition.

In order to quantify the change in the incoherent scattering, energy scans around zero-energy transfer (elastic position) from -1.5 meV to 1.5 meV were performed and are shown in Figure 4.18, for (a) the hydrogenated samples and (b) the standard samples with different numbers of polypropylene sheets. The increase in the incoherent scattering with the increase in the hydrogen content was calibrated using standard specimens (sheets of polypropylene film wrapped around the Zr-4). Kvardakov et al [122] has quantitatively shown that the scattered intensity I is directly related to the hydrogen mass fraction "c". Assuming that an object of the mass, M, consisting of atoms with atomic weight, μ, and containing a mass of hydrogen, m, is placed in a neutron beam with the current density, J, then the incoherent scattering intensity, I, can be written as:

$$I = J \cdot N_A \cdot [m\sigma_i^H + (M/\mu)\sigma_i^{mat}] \cdot S/(4\pi R^2) \quad (4.1)$$

In this equation, σ_i^H and σ_i^{mat} are the incoherent scattering cross sections of hydrogen and the other atoms within the matrix; N_A is Avogadro's constant, S is the area of neutron counter, and R is the distance from the sample to the counter. This equation indicates a linear dependence on the hydrogen mass fraction, but disregards both absorption and multiple scattering and is only valid for small values of *c (= m/M)* when the total neutron attenuation is dominated by the matrix. At high hydrogen mass fractions (~1,000 μg/g), however, the hydrogen absorption gives rise to additional attenuation of the beam within the sample and a saturation effect is expected to appear in the experimental curve.

The amount of the hydrogen in each polypropylene sheet was calculated from its weight as follows: one mole of polypropylene with the molecular mass of 42 grams (g) contains 6 g of hydrogen, thus a sheet of polypropylene (C_3H_6) with the size of 40 mm x 50 mm, which weights 32.5 milligrams (mg) contains (32.5 x 6)/42 = 4.64 mg hydrogen. However, in the neutron beam an area of 40 x 30 mm^2 of film was exposed, which contains m = 2.79 mg hydrogen. The zirconium specimen was weighted and the exposed mass of zirconium to the neutrons was determined to be M =15.85 g. Therefore, we estimated that in a standard specimen, with one sheet of polypropylene, the hydrogen mass fraction, $c = m/M$, is approximately 176 ppm. Neutron incoherent scattering of the standard samples, containing from 1 to 27 sheets were measured using the same procedure and experimental setup as in the case of hydrogen charged specimens. In Figure 4.19(a), the experimental results obtained from the polypropylene samples are indicated by small black dots and in Figure 4.19(b) are shown the samples charged with different amount of hydrogen by larger light blue dots. The continuous line represents the fitted data. As observed in Figure 4.19(a), at approximately 1,000 ppm (1.0 mg/g) hydrogen mass fraction, the incoherent scattering starts to saturate due to the increase of removal of cross section by hydrogen absorption, which cannot be neglected anymore. In fact, this finding is in agreement with the results reported previously [122]. Similarly to [122] we have found that the experimental points for samples wrapped with polypropylene sheets can be fitted well (R = 99%) using the equation:

$$I = I_0 + A(1 - \exp(-c/c_0)) \quad (4.2a)$$

where A, c_0 , and I_0 are the fitting parameters. The value of I_0 has been fixed to 7,569 and represents the sum of counts for the incoherent scattering measured on the as-received sample. The fitting curve, Figure 4.19(b) has been used to determine the hydrogen content of the hydrogen-charged samples by substituting the measured intensities into the equation (4.2b).

$$c = c_0 \ln(1 - \frac{I - I_0}{A}) \tag{4.2b}$$

The calculated values for the hydrogen mass fraction are summarized in Table 4.1. For the standard samples both the effective (resulted from the weight) and the calculated values from the curve, are listed. By comparing these values one can observe that the precision of the detection decreases dramatically with the increases of hydrogen content. For a mass fraction of ≈ 176 ppm hydrogen the error is ± 37.6 ppm while for 4,750 ppm hydrogen the error increases to ± 316 ppm. It can be concluded that the specimen charged with hydrogen gas for 30 minutes contains approximately 1,600 ppm hydrogen, while the 1-hour specimen contains about 2,800 ppm hydrogen. The specimen containing about 5,200 ppm (charged for 1.5 hours) is currently being tested at ISIS for the strain measurements.

4.3. Strain Measurements

4.3.1. Tensile Behavior

4.3.1.1. Macroscopic Behavior

4.3.1.1.1. As-received Condition

The macroscopic stress-strain curve of the hexagonal-close-packed Zr-4 alloy in the as received condition is shown in Figure 4.20. The test was performed using the ENGIN-X instrument and details about the instrument and the experimental setup were discussed in Section 3.5.1. The extensometer data, represented by a continuous black line, indicates that some creep was produced because the test was conducted in a load control. The red circles represent the positions where neutron diffraction strain measurements were collected during the loading and unloading.

TABLE 4.1. Calculated hydrogen mass fraction for hydrogen-gas charged Zr-4 samples.

Hydrogen charging time	Effective H content (mg/g)	Deduced H content (mg/g)	Deduced H content (ppm)
as received	--	0	0
30 min	--	1.591645	1,592
1 hour	--	2.802998	2,803
1.5 hour	-	5.193509	5,194
1 sheet film	0.175914	0.138379	138
2 sheet films	0.351828	0.324829	325
3 sheet films	0.527743	0.593555	595
6 sheet films	1.055485	1.135777	1,136
9 sheet films	1.583228	1.477601	1,478
12 sheet films	2.110971	2.216871	2,217
15 sheet films	2.638714	2.574762	2,575
21 sheet films	3.694199	3.422091	3,422
27 sheet films	4.749685	5.065144	5,065

The tensile behavior shows that the elastic modulus (E), 0.2% yield stress (σ_y), and hardening exponent (n), are about 121 GPa, 242 MPa, and 1.06, respectively, Table 4.2.

4.3.1.1.2. Gas Hydrogen Charged Condition

Figure 4.21 shows the macroscopic behavior of the tensile specimen containing about 1,600 ppm hydrogen (30 minutes of hydrogen-gas charging, blue dotted line) (a) extensometer data in comparison with the as-received specimen profile (black continuous line) and (b) the positions where neutron diffraction strain measurements were collected during the loading and unloading (the red circles). Similar to the as-received condition, the specimen charged with hydrogen shows some creep deformation, which can be seen in the extensometer data. From the stress-strain curve, it was calculated that the elastic modulus, 0.2% yield stress, and hardening exponent are about 109 GPa, 216 MPa, and 1.06, respectively, Table 4.2.

As can be seen in Table 4.2, the specimen charged with hydrogen is more compliant (about 9.9 % smaller E than the as-received specimen) and has smaller yield strength. The hardening exponent is the same for both specimen conditions. An explanation for this trend could be the overestimation of stress due to the presence of the zirconium hydride layer at the surface which makes the exposed zirconium area to the same stress level smaller than in the as-received case.

TABLE 4.2 Macroscopic stress-strain parameters.

Specimen	E (GPa)	σ_y (MPa) 0.2%offset	n
As-received (Zr-4)	121	242	1.06
30 min. H charged	109	216	1.06

4.3.1.2. Microscopic Behavior

4.3.1.2.1. As-received Condition

Figure 4.22 shows the lattice-strain anisotropy in the elastic and plastic regimes. The in-situ evolution of the elastic lattice strains (με) are presented as a function of the applied stress for six zirconium reflections: Zr (100), Zr (002), Zr (101), Zr (102), Zr (110), and Zr (103) on both axial (plane normal is parallel to the tensile axis) and transverse (plane normal is perpendicular to the tensile axis) directions. The dotted horizontal line at an applied load of 242 MPa marks the macroscopic 0.2 % yield stress (σ_y). In the elastic regime, all of the lattice strains have a linear behavior, while as the specimen enters the plastic regime a non-linear behavior can be seen.

Elastic regime

Below the 0.2 % yielding the lattice strain behavior is linear but anisotropic as shown in Figure 4.23(a) axial and (b) transverse. The elastic moduli for each reflection in both axial and transverse directions are shown in Table 4.3. They were obtained by linear fitting in the elastic regime for each reflection. It can be observed that (002) orientation is about 15% stiffer than about the (100) orientation in axial direction (E_{100}^{ax} =102 GPa, E_{002}^{ax} = 120 GPa) and only about 7% in transverse direction. The Poisson ratio (ν) is obtained from the ratio between the axial and transverse elastic moduli and it can be seen that the (002) exhibits the highest value, Table 4.3.

Slip System

The crystallography of the hcp lattice makes use of the four Miller-Bravais indices, *hkil*, attached to the four axis system $\{ \vec{a}_1, \vec{a}_2, \vec{a}_3, \vec{c} \}$, where c is the axis of six-fold symmetry and the three other axes are lying in the basal plane, Figure 4.24. Prediction of the preferred slip system in hcp materials is not an easy task and depends on the *c/a* ratio. In the case of Zr-4, the *c/a* ratio = 1.597 and thus the {0001} prism slip would be preferred in the $<11\bar{2}0>$ close-packed direction [34].

TABLE 4.3 Elastic modulus and Poisson's ratio for Zr-4 in as-received condition for both axial and transverse directions

E (GPa)	Zr(100)	Zr(002)	Zr(101)	Zr (102)	Zr(110)	Zr(103)
Axial	102	120	103	101	105	103
Transverse	-285	-305	-300	-297	-307	-297
ν	0.36	0.39	0.34	0.34	0.34	0.35

Plastic regime I

Figure 4.22 shows that the development of lattice strain is very non-linear once the specimen enters the plastic regime. The in-situ evolution of a- and c- axes strains are presented in Figure 4.25(a), in axial direction (closed symbols) and transverse direction (open symbols). ε_a^{ax}, ε_c^{ax}, ε_a^{tr}, and ε_c^{tr} represent the measured elastic lattice strains in axial *a* axis, axial *c* axis, transverse *a* axis, and transverse *c* axis, respectively.

In axial direction both lattice strains *a* and *c* increase (tensile). However, ε_a^{ax} increase more rapidly than ε_c^{ax}. In the transverse direction, ε_a^{tr} and ε_c^{tr} increases (compressive). The ε_a^{ax} and ε_c^{tr} are measured from one grain set (G1 where *a* axis is near parallel to the loading direction and *c* axis is near perpendicular to the loading direction); while ε_c^{ax} and ε_a^{tr} are measured from another grain set (G2 where *c* axis is near parallel to the loading direction and *a* axis is near perpendicular to the loading direction), Figure 4.25(b).

In the axial direction, ε_c^{ax} increases in the elastic regime and as it enters the plastic regime the slip system is activated on {0001} planes along $<11\bar{2}0>$ directions. When such slip system is active, ε_c^{ax} seems to saturates (the curve inflection is towards the vertical) in the plastically deformed grain set (G2) while ε_a^{ax} (G1) must accumulate a proportionally larger increment in strain (tensile) for balance along the loading direction. The increase in ε_a^{ax} (G1) in turn, results in a further increase (compressive) in ε_c^{tr} (G1) due to Poisson's effect in the same grain set. Note that when axial *c* is favorable orientated to slip the transverse *c* is not able to slip. Similarly, ε_a^{tr} (G2) increases (compressive) in the elastic regime, then as the plastic regime is entered and ε_c^{ax} (G2)

starts to slip, ε_a^{tr} does not accumulates more strain and eventually saturates, due to Poisson's effect in the same grain. The saturation of ε_a^{tr} in the plastically deformed grain set (G2) means that ε_c^{tr} (G1) must accumulate a proportionally larger increment of strain (compressive) for balance along the loading direction.

Residual strains

Residual lattice strain $\varepsilon_{a,}$ in axial and transverse directions is shown in Figure 4.26. The lattice strain evolution containing both the loading and unloading components is shown in Figure 4.26(a). Circled data are residual strains obtained by unloadings to a stress of approximately 5 MPa. The development of the residual lattice strain ε_a at the unloads, is presented in Figure 4.26(b). It can be seen that in transverse direction only tensile residual stain accumulates reaching the maximum value of approximately 1,100 με, around an applied strain of 5 %. In the axial direction first a compressive residual strain of about 280 με is accumulated which transforms to tensile, at 1% applied strain, reaching a maximum of approximately 300 με when strain is abut 5 %.

Residual lattice strain ε_c in axial and transverse directions is shown in Figure 4.27(a), containing both the loading and unloading components and where the circled data are residual strains obtained by unloadings to a stress of approximately 5 MPa. The development of the residual lattice ε_c at the unloads, is shown in Figure 4.27(b). It can be seen that in both directions compressive residual stains accumulate in *c-axis*. In the axial direction it reaches the maximum value of approximately 1,200 με while in the transverse direction the compressive residual strain accumulated reaches a maximum of approximately 4,000 με, at an applied strain of approximately 5 %.

Finally, the residual lattice strains for six different Zr reflections in both axial and transverse directions are presented in Figure 4.28. It can be seen that the residual strain qualitatively varies from a maximum of 1,800 με tensile residual strain in Zr (110) in transverse direction to a compressive residual strain of 4,000 με in Zr (002) in transverse direction, as well. It can be concluded that the high plastic anisotropy present in this Zr-4 alloy leads to significant residual strains in different crystallographic orientations.

4.3.1.2.2. Gas Hydrogen Charged Condition

Figure 4.29 shows the lattice strain anisotropy in the elastic and plastic regime for the specimen with 1,600 ppm hydrogen. The applied stress (MPa) is represented as a function of elastic lattice strain (με) for six zirconium reflections, Zr (100), Zr (002), Zr (101), Zr (102), Zr (110), and Zr (103) on both axial and transverse directions. The dotted horizontal line at an applied load of 216 MPa marks the macroscopic 0.2 % yield stress (σ_y). Similarly to the as-received specimen, the hydrogenated specimen shows the same linear behavior in the elastic regime and a non-linear behavior with high anisotropy in the plastic regime.

Elastic regime

Figure 4.30 shows the lattice strain behavior of the specimen containing 1,600 ppm hydrogen in the elastic regime (below the 0.2 % offset yielding) for (a) axial direction and (b) transverse direction. The elastic moduli for each reflection in both directions are shown in Table 4.4. It can be observed that *c* axis is about 20% stiffer than *a* axis in axial direction (E_a^{ax} = 97 GPa, E_c^{ax} = 117 GPa). The Poisson ratio (ν) values for (100) and (002) are larger than the rest of the reflections. Therefore, the Poisson ratio for (100) for the 30-minute specimen is larger (approximately 20%) than in the case of the specimen without hydrogen. Note that (002) shows similar values of the Poisson ratio for both conditions.

However, it can be concluded that overall, specimen in hydrogenated condition is qualitatively similar to the as-received specimen.

Plastic regime I

The in-situ evolution of a- and c- axes strains are presented in Figure 4.31 in axial direction (closed symbols) and transverse direction (open symbols). It can be seen that ε_a^{ax}, ε_c^{ax}, ε_a^{tr}, and ε_c^{tr} follow the same trend as in the case of the specimen without hydrogen.

TABLE 4.4 Elastic modulus and Poisson's ratio for 30 minutes hydrogen charged condition (30-min) and as-received condition (AR) in both axial and transverse directions.

E (GPa)	Zr(100)	Zr(002)	Zr(101)	Zr(102)	Zr(110)	Zr(103)
Axial-30-min	97	117	99	100	103	103
Transverse-30-min	-222	-292	-281	-294	-313	-284
ν -30-min	0.43	0.4	0.35	0.34	0.33	0.36
Axial-AR	102	120	103	101	105	103
Transverse-AR	-285	-305	-300	-297	-307	-297
ν-AR	0.36	0.39	0.34	0.34	0.34	0.35

Residual strains

The comparison of the residual lattice strains ε_a between the 30-minute and as-received specimens are shown in Figure 4.32(a) axial and (b) transverse directions. It can be seen that in the axial direction, the a-axis of the specimen with hydrogen (red closed dots) develops only compressive residual strain while in the as-received specimen (black closed squares) the residual strain is first compressive and changes to tensile under approximately 0.75 % applied strain. In the transverse direction, Figure 4.32(b) residual lattice strain ε_a is tensile for both conditions, 30-minutes (red open dots) and as-received (black open squares).

Note that, in both axial and transverse directions, the difference in the residual strains between the two specimens is approximately 300 με.

In addition, the development of the residual lattice strain ε_c in the two cases is shown in Figure 4.33(a) axial and (b) transverse directions. In both directions the residual strains in c-axis are compressive. In the axial direction, residual lattice strain ε_c in the specimen containing 1,600 ppm hydrogen (red closed stars) is overall larger with about 400 με than in the as-received specimen (black closed triangles). On the other hand, in the transverse direction the overall residual strain in c-axis for the 30-minute case (red open stars) is smaller (approximately 600 με) than the as-received condition (black open triangle).

Finally, the residual lattice strains for six different Zr reflections in both axial and transversal directions for the specimen with hydrogen are presented in Figure 4.34. It can be seen that the residual strain varies from a maximum of 1,750 με tensile residual strain in Zr (110) (similar to the as-received specimen) to a compressive residual strain of 3,000 με in Zr (002).

4.3.2. Fatigue Behavior

4.3.2.1. Macroscopic Behavior

4.3.2.1.1. As-received Condition

Figure 4.35 exibits the evolution of the average lattice strains as a function of the distance from the crack tip (a) parallel to the loading direction, in-plane strain (IP) and (b) perpendicular to the loading direction, trough-thickness strain (TT).

The average strain was obtained using the following formula:

$$(2\varepsilon_a + \varepsilon_c)/ 3 \qquad (4.3)$$

where ε_a and ε_c are the a- and c- axes lattice strains, respectively.

In the in-plane direction, when a load of 667 N is applied, the average strain is compressive behind the crack tip and became tensile at the crack tip, an increases to a maximum of 400 με at 1 mm ahead the crack tip. When the load is increase to 4,444 N the lattice strain increases as well, and follows the same trend. The maximum strain reached in this case is approximately 1,700 με at 1 mm ahead the crack tip.

In the trough-thickness direction, when a load of 667 N is applied, the macroscopic strain is tensile behind the crack tip and became compressive at 1 mm ahead of the tip, reaching a maximum of 300 με. However, at 7 mm in front of the crack tip strain profile changes again from compressive to tensile. When the load is increased to 4,444 N, the strain is compressive along the crack and the maximum of approximately 1,600 με is attained at 3 mm in front of the crack tip.

In summary, it can be observed that the average strain profile evolution around the crack tip for the specimen in as-received condition corresponds to the effect of in-situ applied loading.

4.3.2.1.2. Electrochemically Hydrogen Charged Condition

In Figure 4.36 is shown the comparison between the evolution of average lattice strains for the specimen electrochemically charged with hydrogen (red dots) and as-received specimen (black squares) as a function of the distance from the crack tip, (a) in-plane strain (IP) direction (closed symbols) and (b) trough-thickness strain (TT) direction (open symbols), when a load of 4,444 N was applied. The average lattice strains were obtained using formula (4.3). The comparison between these two specimens, hydrogen charged (red stars) and as-received (black triangles), under 667 N load is shown in Figure 4.36(c) IP strain direction (closed symbols) and (d) TT strain direction (open symbols).

The electrochemically-charged CT specimen, as described in Section 4.2, shows zirconium hydride only on its surface. The average lattice strains in both directions, IP and TT, for this specimen follow a similar pattern as the specimen in as-received condition. However, the average lattice strains for the charged specimen is overall larger except the TT direction and under a load of 4,444 N, Figure 4.36(b) when as-received specimens exhibits a compressive strain about 300 με larger at the crack tip.

4.3.2.2. Microscopic Behavior

4.3.2.2.1. As-received Condition

Lattice strains, ε_{100} and ε_{002} as a function of the distance from the crack tip, for the specimen in as-received condition under a load of 667 N are shown in Figure 4.37(a) in-plane direction (closed symbols) and (b) through-thickness direction (open symbols).

In the in-plane direction, strain in Zr (100), ε_{100}^{IP} (black squares), has a small magnitude, varying between compressive and tensile in a range of approximately 450 to 700 με. In turn, strain in Zr (002), ε_{002}^{IP} (red dots), is compressive along the crack; reaching a maximum of 1,500 με, except at 8 mm ahead the crack tip when strain becomes tensile at a value of 150 με.

For the through-thickness direction, under the 667 N load, ε_{100}^{TT} is tensile behind the crack tip (900 με, max.) and compressive at 1 mm ahead the tip reaching a maximum of 1,350 με at 6 mm. On the other hand, ε_{002}^{TT} starts compressive from a maximum of 1,100 με behind the crack tip and becomes tensile at 2 mm in front of it.

When the load is increased to 4,444 N, lattice strains show cleaner trend, Figure 4.38. For the in-plane direction (closed symbols), Figure 3.38(a), ε_{100}^{IP} (black triangles) increases from 450 με (compressive) to 2,400 με (tensile) at the crack tip. It decreases to 0 με at 8 mm in front of the crack tip, compression to 900 με at 13 mm, and eventually becomes zero again. In turn, ε_{002}^{IP} follows a similar pattern except the maximum values. Lattice strain ε_{002}^{IP}, (red stars) is compressive (900 με) at 3 mm behind the crack tip and reaches a maximum tensile of 750 με at 2 mm ahead the tip.

Figure 4.38 (b), shows the lattice strains ε_{100}^{TT} and ε_{002}^{TT} in the through-thickness direction (open symbols), when a load of 4,444 N was applied. Strain in the Zr (100) (black triangles), is mostly compressive with a maximum of 1,650 με at 7 mm in front of the crack. On the other hand, strain in Zr (002) increases (compressive) dramatically from 750 με, behind the crack tip to a maximum of 2,250 με at the crack tip then became tensile at 6 mm in front of the tip

4.3.2.2.2. Electrochemically Hydrogen Charged Condition

Note that because the as-received specimen showed under the stress level of 667 N a small magnitude in strain a comparison with the charged specimen it will not be discussed here. A comparison of lattice strain ε_{100} as a function of the distance from the crack tip between the specimen electrochemically charged with hydrogen (red dots) and as-received specimen (black triangles) and when a load of 4,444 N was applied is shown in Figure 4.39(a) in-plane direction (closed symbols) and (b) trough-thickness direction (open symbols). The lattice strains ε_{100} develops overall similar pattern with the specimen in as-received condition.

In addition, the comparison of lattice strain ε_{002} as a function of the distance from the crack tip between the latter specimens and when a load of 4,444 N was applied is shown in Figure 4.40(a) in-plane direction (closed symbols) and (b) trough-thickness direction (open symbols). The difference between Zr (002) strains in the two conditions is more significant in the IP direction.

In summary, for the IP direction, strain for both a-and c-axes is larger in the case of the specimen charged with hydrogen and also there is a consistent 2 mm deviation

from the initial crack-tip length (as-received specimen) which may be explained by the crack propagation due to the brittle nature of the zirconium hydride layer on the surface.

Chapter 5

Conclusions

From this investigation, the following conclusions are drawn:

The starting Zr-4 alloy (as-received condition) has a ductile fracture behavior, the grain size with a mean diameter of approximately 700 μm, random texture and a hexagonal-closed-packed crystallographic structure at room temperature. Moreover, Zr-4 shows high elastic-plastic anisotropy which lead to significant residual strains in different crystallographic orientations and different specimen directions (axial and transverse).

In the tensile specimens charged with a mixture of hydrogen gas at 430 °C for ½ hour and 1 hour the presence of a second phase was identified as the face-centered-cubic delta (δ)-ZrH_2, in the bulk, using neutron diffraction. The zirconium hydride peak intensities were higher near the surface of the specimens in agreement with their distribution in a thin layer on the surface. In addition, a significant increase in the background of the neutron diffraction patterns was observed which is due the incoherent scattering of hydrogen which allows the quantification of the hydrogen content in the specimen. Therefore, using incoherent neutron scattering, it was determined that the 30-minute charged specimen contains 1,600 ppm hydrogen and 1-hour charged specimen has 2,800 ppm hydrogen. Moreover, it was observed that the zirconium hydrides form a layer in a ring shape and thickness of approximately 0.4 mm (1-hour specimen) on the surface of the specimens, using optical microscopy. Further, the fractographic investigation showed that while the as-received specimen exhibits a uniform ductile behavior, the hydrogenated specimen (1-hour charged) is ductile only around its center and brittle regions were observed near the surface of the specimen.

The hydride layer is brittle and it is believed to affect the mechanical behavior of Zr-4 specimens. Studies of the macrostrains showed that the elastic modulus and the yield stress are smaller for the specimen charged for 30 minutes with hydrogen gas compared to the as-received condition, however they have similar hardening exponent.

The microstrains investigation indicates that anisotropic behavior is similar in both specimens and the residual strains are overall larger in the hydrogenated specimen.

A compact tension (CT) specimen, fatigue pre-cracked to a crack length of 22.86 mm in as-received condition, was tested by *in-situ* monotonic loading and a significant increase in average lattice strain around the crack tip was observed when the stress was increase from 667 N to 4,4444 N.

Another CT specimen was charged electrochemically with hydrogen for 4 hours at room temperature. This specimen shows the presence of a second phase, delta (δ)-ZrH_2 only on its surface. Note that using x-ray diffraction, the zirconium hydrides were identified above the solution line which is encouraging for the *in-situ* corrosion study experiments. The bulk phase study, using neutron diffraction showed no detectable amounts of hydrides or changes in the background of diffraction patterns. This trend is believed to be due to the absence of any promoters during the charging process. The same monotonic loading, similar to the as-received specimen, was applied to this specimen as well. It was observed that the average lattice strains are overall larger for the specimen charged with hydrogen.

Chapter 6

Future Work

Continued work in this Zr-4/Hydrogen system should be undertaken to further investigate the mesoscopic (hkl-specific) strains as a function of the applied load and hydrogen content.

The mechanical properties of a tensile specimen containing a higher amount of hydrogen than the 30-minute specimen should be investigated. Moreover, compact tension specimens should be charged with hydrogen gas containing the same amounts as the tensile specimen. In-situ neutron diffraction strain measurements will provide details related to the phase distribution and internal strain profile at the crack tip. By comparing data from the hydrogenated specimens with those collected from the as-received specimen the effects of hydrogen can be quantified.

It is also planned that a computational model, such as polycrystalline finite-element modeling of the in-situ tensile tests and the monotonic loading tests will correlate the uniaxial behavior with fracture mechanics characteristics of the hydrogen-charged Zr-4 at continuum and mesoscopic length scales. The computation modeling work is already underway with Dr. Sarma at Oak Ridge National Laboratory.

LIST OF REFERENCES

1. H. K. Birnbaum and P. Sofronis, *Mat. Sci. Eng.*, A 176 **(1994)**: p. 191.
2. H. K. Birnbaum, I. M. Robertson, P. Sofronis, and D.Teter, "*Proceedings of the Conference on Corrosion Deformation Interactions". edited by T. Magnin (London: Institute of Materials)*, Nice, France **(1997)**: p. 172-195.
3. J. P. Hirth, *Met. Trans. A*, 11 **(1980)**: p. 861.
4. R. A. Oriani, *Acta met.*, 18 **(1980)**: p. 147.
5. N. W. Ashcroft, *Nature*, 340 **(1989)**: p. 345.
6. H. K. Mao and R. J. Hemley, *Science*, 244 **(1989)**: p. 1462.
7. A. I. Safonov, S. A. Vasilyev, I. S. Yasnikov, I. I. Lukashevich, and S. Jaakkola, *Phys. Rev. Lett. B*, 81 **(1998)**: p. 4545.
8. L. Schlapbach, A. Züttel, P. Gröning, and P. Aebi, *Appl. Phys. Let.*, 72A **(2001)**: p. 245-253.
9. R. B. McLellan, "*In Phase Stability in Metals and Alloys".* 393 **(1967)** P.S. Rudman, J. Stringer, and R. I. Jaffee, eds.
10. R. A. Oriani, "*Hydrogen in Metals".* **(1967)**: p. 32.
11. J. Bergsma and J. A. Goedkoep, *Physica B*, 26 **(1960)**: p. 744.
12. J. E. Worsham, M. K. Wilkinson, and C. G. Shull, *J. Phys. Chem. Solids*, 3 **(1957)**: p. 303.
13. V. A. Somenkov, V. F. Petrunin, S. S. Shilfshtein, and A. A. Chertkov, *Sov. Phys. Cryst.*, 14 **(1960)**: p. 522.
14. W. R. Heller, *Acta Met.*, 9 **(1961)**: p. 600.
15. R. Gibala, *Trans. Met. Soc. AIME*, 239 **(1967)**: p. 1574.
16. C. C. Baker and H. K. Birnbaum, *Acta Met.*, 21 **(1973)**: p. 865.
17. J. A. Peterson, R. Gibala, and A. R. Troiano, *J. Iron Steel Inst.*, 207 **(1969)**: p. 86.
18. A. S. Nowick and B. S. Berry, "*Anelastic Relaxation in Crystalline Solids". Academic Press, New York*, **(1972)**.
19. K. V. Ravi and R. Gibala, *Met. Trans.*, 2 **(1971)**: p. 1219.
20. D. G. Westlake, *Trans. Met. Soc. AIME*, 245 **(1969)**: p. 287.
21. Y. Sasaki and M. Amano, *Trans. Jap. Inst. Metals*, 10 **(1969)**: p. 29.
22. C. A. Wert, *J. Phys. Chem Solids*, 31 **(1970)**: p. 1771.
23. H. K. Birnbaum and C. A. Wert, "*In Proc. Internat. Meeting Hydrogen In Metals". Julich, Jul-Conf-6*, II **(1972)**: p. 626.
24. E. E. Fletcher and A. R. Elsa, "*Hydrogen Movement in Steel-Entry, Diffusion, and Elimination". DMIC Report, Battele Memorial Institute, Columbius, OH*, 219 **(1965)**.
25. R. B. McLellan, *Mat. Sci. Eng*, 9 **(1972)**: p. 121.
26. A. D. McQuillan, "*In Phase Stability in Metals ans Alloys".* McGraw-Hill, New-York **(1967)**: p. 375.
27. R. Gibala, *Proc. Internat. Symp. Stress Corrosion Cracking and Hydrogen Embrittlement of Iron Base Alloys*, France, 244-245 **(1973)**.
28. S. S. Sidhu, L. Heaton, and D. D. Zauberies, *Acta Cryst.*, 9 **(1956)**: p. 607.
29. C. Hagg, *Z. Phys. Chem.*, II **(1931)**: p. 433.
30. H. L. Yakel, *Acta Cryst.*, II **(1958)**: p. 46.
31. G. M. Bond, I. M. Robertson, and H. K. Birnbaum, *Acta met.*, 35, 36, 37 **(1987, 1989, 1989)**: p. 2289, 2193, 1407.

32. E. P. George, C. T. Liu, and D. P. Pope, *Scripta met.*, 27 **(1992)**: p. 365.
33. A. W. Thomson and I. M. Bernstein, *Advances in Corrosion Science and Technology*, 7 **(1980)**: p. 145.
34. R. W. Hertzberg, " *Deformation and Fracture Mechanics of Engineering Materials".* 3-rd Edition **(1937)**: p. 425-427.
35. P. Sofronis and I. M. Roberston, *Philos. Magazine A*, 82 **(2002)** 17/18: p. 3405-3413.
36. R. A. Oriani and P. H. Josephic, *Acta met.*, 22, 25 **(1974, 1977)**: p. 1065, 979.
37. C. D. Beachem, *Metall. Trans. A*, 3 **(1972)**: p. 437.
39. M. A. V. Devanathan and Z. Stachurski, *J. Electrochem. Soc.*, 111 **(1964)**: p. 619.
38. G. M. Bond, I. M. Robertson, and H. K. Birnbaum, *Acta met.*, 35, 36, 37 **(1987, 1989, 1989)**: p. 2289, 2193, 1407.
40. R. M. Barrer, " *Diffusion In and Through Solids".* England: Cambridge Univ. Press. **(1981)**.
41. H. H. Johnson, *Met. Trans.*, 19A **(1988)**: p. 2371.
42. R. A. Oriani, *Acta Met.*, 18 **(1970)**: p. 147.
43. A. McNabb and P. K. Foster, *Trans. Met. Soc. AIME*, 227 **(1963)**: p. 618.
44. M. Koiwa, *Acta Met.*, 22 **(1974)**: p. 1259.
45. B. G. Pound, *Corrosion*, 45 **(1989)**: p. 18.
46. J. Volkl and G. Alefeld, "*Topics in Applied Physics". Hydrogen in Metals I*, 28 New York **(1978)**: p. 321-348.
47. H. H. Johnson and R. W. Lin, "*Hydrogen Effects In Metals".* I. M. Bernstein and A. W. Thompson eds. **(1981)** TMS-AIME, New York: p. 3-25.
48. C. A. Wert, "*Topics in Applied Physics". Hydrogen in Metals II*, 29 New York **(1978)**: p. 305-330.
49. R. N. Iyer, H. W. Pickering, and M. Zamanazadeh, *Scripta Met.*, 22 **(1988)**: p. 911-916.
50. R. N. Iyer, H. W. Pickering, and M. Zamanazadeh, *J. Electrovchem. Soc.*, 136 **(1989)**: p. 2463.
51. R. N. Iyer and H. W. Pickering, "*Hydrogen Effects on Material Behavior". Proc. Internat. Conf. On the Effect of Hydrogen on the Behavior of Materials*, Wyoming **(1989)**: p. 195-201.
52. H. K. Birnbaum, M. L. Grossbeck, and M. Amano, *Less Comm. Met.*, 49 **(1976)**: p. 357-370.
53. S. Gahr, M. L. Grossbeck, and H. K. Birnbaum, *Acta Met.*, 25 **(1977)**: p. 125-134.
54. M. L. Grossbeck and H. K. Birnbaum, *Acta Met.*, 25 **(1977)**: p. 135-147.
55. D. S. Shih, I. M. Robertson, and H. K. Birnbaum, *Acta Met.*, 36 **(1988)**: p. 111.
56. D. G. Westlake, *Trans. ASM*, 62 **(1969)**: p. 1000-1006.
57. T. B. Flannagan, N. B. Mason, and H. K. Birnbaum, *Scripta Met.*, 15 **(1981)**: p. 109-112.
58. M. P. Puls, *Acta Met.*, 32, 30 **(1984)**: p. 1259-1269
Sol. (a) 107-116.
59. J. C. M. Li, R. A. Oriani, and L. S. Darken, *Z. Physik Chem. Neue Folge*, 49 **(1966)**: p. 271-291.
60. M. M. McMeeking and A. G. Evans, *J. Am. Ceram. Soc.*, 65 **(1982)**: p. 242-246.

61. B. Budiansky, J. W. Hutchinson, and J. C. Lambropoulos, *Int. J. Solids Struct.*, 19 **(1983)**: p. 337-355.
62. J. P. Hirth, "*Chemistry and Physics of Fracture". (Proc. the NATO Advanced Research Workshop on Chemistry and Physics of Fracture, Bad Reichenhall, FRG, 23 June-1 July, 1986)*, (ed. by R. M. Latanision and R. H. Jones) **(1987)** Martinus Nijhoff Publishers, The Netherlands: p. 538-551.
63. S. Gahr, B. J. Makenas, and H. K. Birnbaum, *Acta Met.*, 28 **(1980)**: p. 1207-1213.
64. L. A. Simpson and M. P. Puls, *Met. Trans.*, 104 **(1979)**: p. 1093-1105.
65. R. Dutton, K. Nuttall, M. P. Puls, and L. A. Simpson, *Met Trans.*, 8A **(1977)**: p. 1553-1562.
66. R. Dutton and M. P. Puls, "*Effect of Hydrogen Behavior of Materials". Met.Soc. AIME NY*, **(1976)** (ed. by A. W. Thompson and I. M. Bernstein): p. 516-525.
67. R. Dutton, C. H. Woo, K. Nuttall, and L. A. Simpson, "*Hydrogen in Metals". (Proc. of the 2nd International Congress, Paris, France, 6-10 June, 1977)*, 1 **(1978)** Pergamon Press, NY: p. 3C6 1-8.
68. A. J. White, A. Sawatzky, and C. H. Woo, "*Atomic Energy of Canada Limited Report"*. **(1969)** AECL-8386, Pinawa, Manitoba.
69. A. F. Shalabi and D. A.Meneley, *Eng. Mater. Tech.*, 113 **(1991)**: p. 443-448.
70. F. Ellyin and J. Wu, *Acta Met.*, 42 **(1994)**: p. 2709-2717.
71. S. Q. Shi, M. Liao, and M. P. Puls, "*Atomic Energy of Canada Limited Report"*. **(1994)** CoG-I-94-276, Pinawa, Manitoba.
72. J. Lufrano and P. Sofronis, Int. J. Solids Structures **(1995)**.
73. J. Lufrano, P. Sofronis, and H. K. Birnbaum, . *Mech. Phys. Solids*, 44 **(1996)** 2: p. 179-205.
74. J. Lufrano, P. Sofronis, and H. K. Birnbaum, *J. Mech. Phys. Solids*, 46 **(1998)** 9: p. 497-1520.
75. H. G. Rickover, L. D. Geiger, and B. Lustman, "*History of the development of zirconium alloys for use in nuclear reactors"*. **(1975)** US Report, Division of Naval Reactors, Washington, DC, TID-26740.
76. D. E. Thomas, "*Metallurgy of Zirconium". McGraw-Hill, National Nuclear Energy Series*, VIII-4, New York (Chapter 11, Pt. II) **(1955)** B. Lustman, F. Kerze (Eds.).
77. R. A. Ploc, *J. Nucl. Mater.*, 28 **(1968)**: p. 48.
78. S. Kass, *Proceedings of the Symposium on the Corrosion of Zirconium Alloys New York*, **(1963)** ASTM-STP-368, American Soc. for Testing and Materials, Philadelphia, PA,: p. 3040.
79. B. Cox, *Advances in Corrosion Science and Technology*, 5, Plenum,NY **(1976)** M.G. Fontana, R.W. Staehle (Eds.): p. 173.
80. B. Cox and T. Johnston, *Corrosion*, 18 **(1962)**: p. 33t.
81. A. M. Garde, G. P. Smith, and R. C. Pirek, *Proceedings of 11th International Symposium on Zr in the Nucl. Industry, Garmisch-Partenkirchen, Germany*, American Society for Testing and Mater., W. Conshohocken, ASTM-STP-1295, PA, USA **(1996)** E.R. Bradley, G.P. Sabol (Eds.): p. 407.
82. T. Kido, *Proceedings of 6th International Symposium on Environmental Degradation of Materials in Nuclear Power Systems - Water Reactors,*, San

Diego, CA, USA, American Society for Testing and Materials, Philadelphia, PA, USA **(1988)** R.E. Gold, E.P. Simmons (Eds.): p. 449.
83. M. Blat, L. Legras, D. Noel, and H. Amanrich, *Proceedings of 12th International Symposium on Zr in the Nuclear Industry, Toronto, ON, Canada*, ASTM-STP-1354, American Soc. for Testing and Mater., W. Conshohocken, PA, USA **(2000)** G.P. Sabol, G.D. Moan (Eds.): p. 563.
84. O. N. Pierron, D. A. Koss, A. T. Motta, and K. S. Chan, *J. of Nucl. Mater.*, 322 **(2003)**: p. 21-35.
85. G. Bertolino, G. Meyer, and J. P. Ipina, *J. Nucl. Mater.*, 322 **(2003)**: p. 57-65.
86. A. D. Krawitz, "*Introduction to Diffraction in Materials Science and Engineering*". **(2001)**.
87. H. M. Rietveld, *J. Appl. Cryst.*, 2 **(1969)**: p. 65-71.
88. Y. N. Choi, H. S. Oh, V. T. Em, V. A. Somenkov, C.-H. Lee, and S. D. Park, *Appl. Phys. A*, 74 **(2002)**: p. 1710-1712.
89. F. Couvreur and G. Andre, "*In-Situ Neutron Scattering Study of Hydrogen-Containing Zircaloy-4 Alloys*". *http://www-llb.cea.fr/activ9798/materiau/hydrogen-contaning_Zircaloy.pdf*: p. 72-73.
90. S. S. Sidhu, N. S. S. Murthy, F. P. Campos, and D. D. Zauberis, *Adv. Chem. Ser.*, 39 **(1963)**: p. 87.
91. G. E. Bacon, "*Neutron Diffraction, 3rd. ED. (Clarendon, Oxford)*". **(1975)**.
92. J. H. Root and R. W. L. Fong, *J. Nucl. Mat.*, 232 **(1996)**: p. 75-85.
93. D. Khatamian and V. C. Ling, *J. Alloys Compounds*, 253 **(1997)**: p. 162.
94. D. Khatamian, I. P. Swainson, M. J. W. Lucas, and J. H. Root, *Physica B*, 241-243 **(1998)**: p. 1225-1257.
95. E. Zuzak, J. P. Abriata, A. San-Martin, and F. D. Manchester, *Bin. Alloy Phase Diag.*, 11 **(1982)**: p. 1171.
96. A. I. Kolesnikon, A. M. Balaqurov, I. O. Bashkin, A. V. Belushkin, E. G. Pnyatovsky, and M. Prager, *J. Phys. Condens. Matter*, 6 **(1994)**: p. 8977- 8988.
97. T. M. Holden, J. H. Root, R. A. Holt, and M. Hayashi, *Physica B*, 213 & 214 **(1995)**: p. 793-796.
98. M. T. Hutchings, P. J. Withers, T. M. Holden, and T. Lorentzen, "*Introduction to the Characterization of Residual Stress by Neutron Diffraction*". **(2005)**.
99. T. M. Holden, R. A. Holt, and J. W. L. Pang, *Met. and Mat. Trans. A*, 33A **(2002)**: p. 749-755.
100. D. J. Dever, *J. Appl. Phys.*, 43 **(1972)**: p. 3293.
101. E. Kroner, *Z. Physik.*, 151 **(1958)**: p. 504.
102. C. N. Tome, N. Christodoulou, P. A. Turner, M. A. Miller, C. H. Woo, J. H. Root, and T. M. Holden, *J. Nucl. Mater.*, 227 **(1996)**: p. 273-250.
103. B. Clausen, T. Lorentzen, M. A. M. Bourke, and M. R. Daymond, *Mat. Sci. Eng*, A 259 **(1999)**: p. 17-24.
104. J. Smith, M. N. Bassim, C. D. Liu, and T. M. Holden, *Eng. Fract. Mech.*, 52 **(1995)** 5: p. 843-851.
105. J. Abrata, J. C. Bolcich, and D. Arias, *Binary Alloy Phase Diagrams*, **(1983)**: p. 2088.

106. www.wahchang.com, *Wah Chang Company*, Technical Department.
107. ASTM, *Annual Book of ASTM Standards, ASTM Standard E647-86, Philadelphia, PA*, 3.01 **(1986)**: p. 714-736.
108. H. Tada, P. C. Paris, and G. R. Irwin, *The stress analysis of cracks handbook*, (2nd Ed.) Paris Productions, Inc., St. Louis **(1985)**.
109. L. J. Chen, P. K. Liaw, R. L. Mcdaniels, and D. L. Klarstrom, *Metallurgical and Mateials Transactions A*, 34 A **(2003)**: p. 1451-1460.
110. E. Garlea, H. Choo, D. W. Brown, S. Park, L. L. Daemen, B. Yang, A. Ionita, M. L. Morrison, R. A. Buchanan, P. K. Liaw, H. F. Letzring, and C. R. Hubbard, " *Internal-Strain Profile Around the Crack Tip in Zircaloy-4 Alloy". in-preparation*, **(2005)**.
111. L. F. Coffin, *Annual Review of Materials Science*, 2 **(1972)**: p. 313-348.
112. J. Harris and S. Andersson, *Phys. Rev. Lett.*, 55 **(1985)** 15: p. 1583-1586.
113. ASTM, *ASTM, G 2-88, Standard Test Methods for Corrosion Testing of Products of Zirconium, Hafnium, and Their Alloys in Water at 680 ° F or in Steam at 750 ° F.*, **(Reaproved 2002)**.
114. E. Garlea, H. Choo, P. K. Liaw, E. C. Oliver, J. R. Santisteban, D. A. Smith, P. D. Rack, R. A. Buchanan, and C. R. Hubbard, "*Phase Mapping Study on Hydrogen Gas-Charged Zircaloy-4". in-preparation*, **(2005)**.
115. www.isis.rl.ac.uk/engineering/.
116. http://lansce.lanl.gov/lujan/ER1ER2/SMARTs/index.html.
117. A. C. Larson and R. B. V. Dreele, "*General Structure Analysis System (GSAS)". Los Alamos National Laboratory Report LAUR 86-748*, **(2004)**.
118. M. R. Daymond and H. G. Priesmeyer, *Acta Mater.*, 50 **(2002)**: p. 1613-1626.
119. E. Garlea, H. Choo, P. K. Liaw, E. C. Oliver, J. R. Santisteban, R. Rucker, P. D. Rack, R. A. Buchanan, and C. R. Hubbard, "*Elastic-Plastic Anysotropy of a hcp Zr-4 Alloy". In-Preparation*, **(2005)**.
120. M. Grange, J. Benson, and E. Andrew, *Met. and Mat. Trans A*, 31 A **(2000)**: p. 679-690.
121. G. Bertolino, G. Meyer, and J. P. Ipina, *J. of. Nucl. Mater.*, 320 **(2003)**: p. 272-279.
122. V. V. Kvardakov, H. H. Chen-Mayer, and D. F. R. Mildner, *J. Appl. Phys.*, 83 **(1998)** 7: p. 3876-3879.
123. http://hb1a.ornl.gov/
124. http://www.ccp14.ac.uk/tutorial/powdcell/

APPENDIX

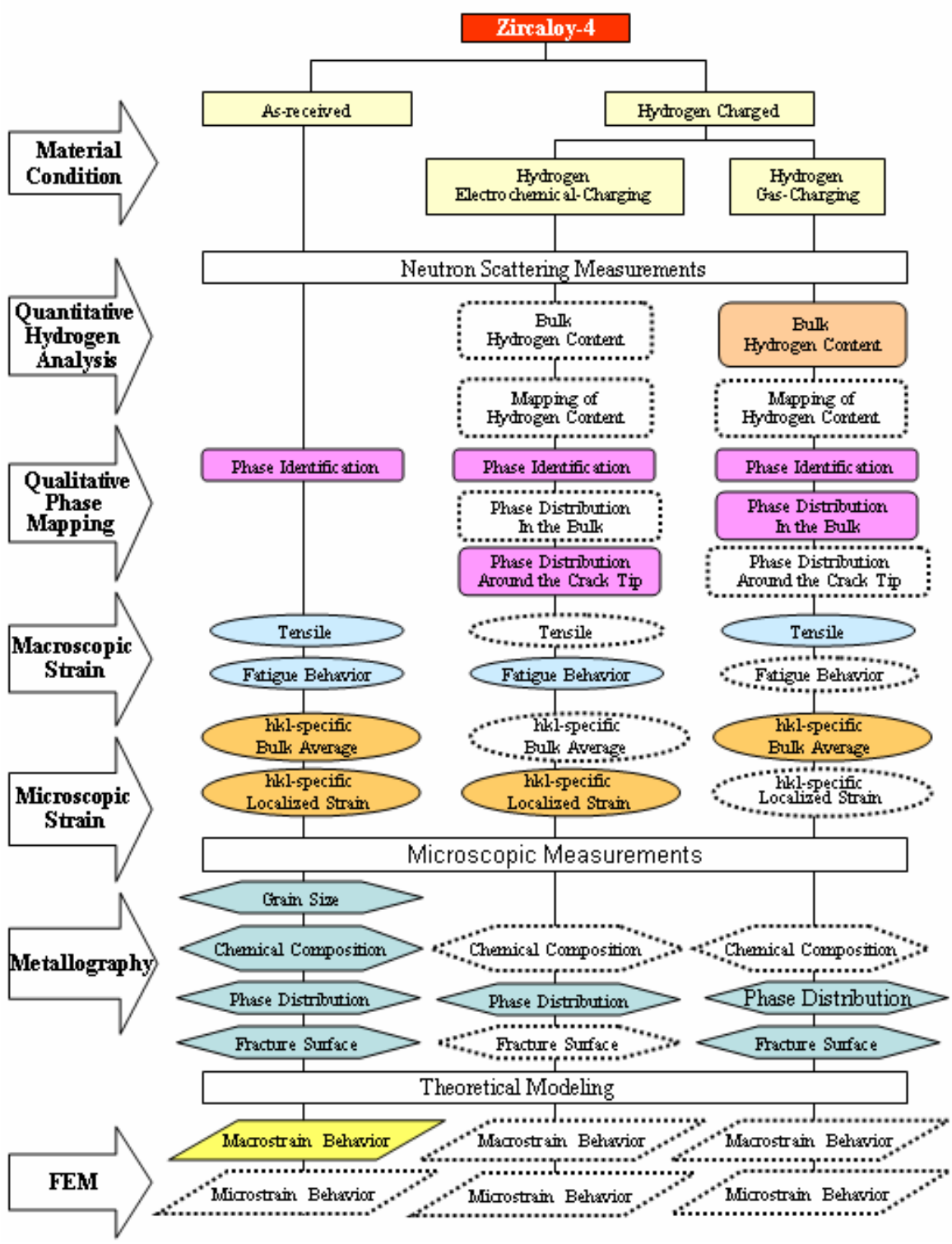

FIGURE 1.1 Flow chart of the detailed research plan. The boxes with dotted lines represent the research that need to be performed in the future.

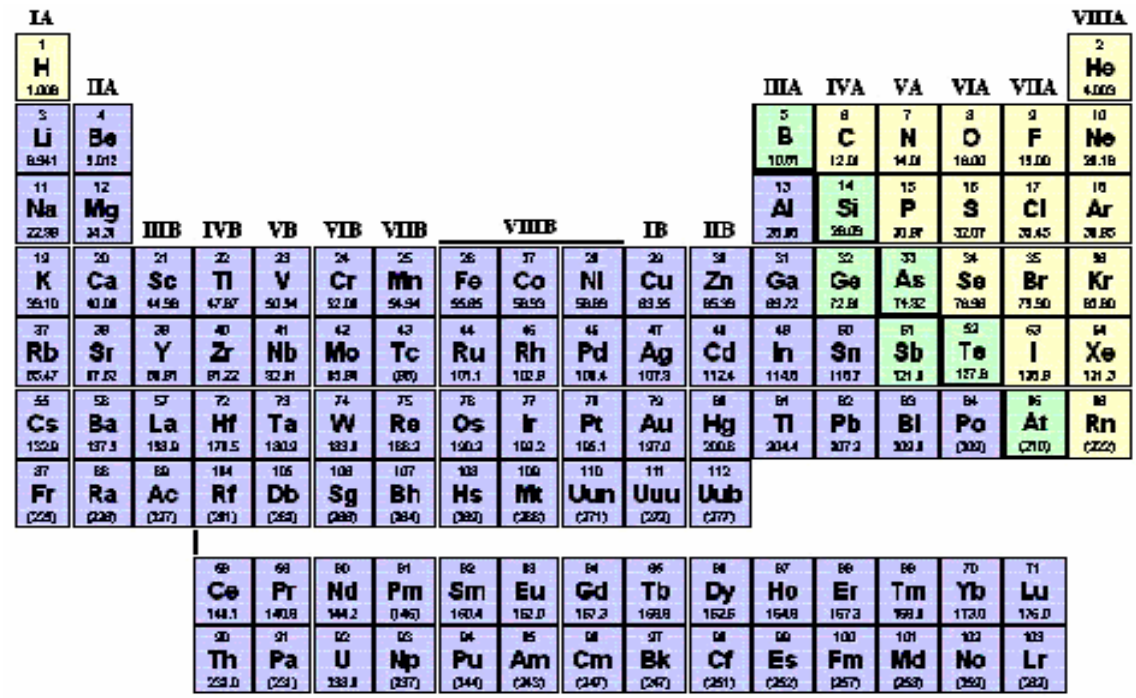

FIGURE 2.1 The periodic table of the elements.

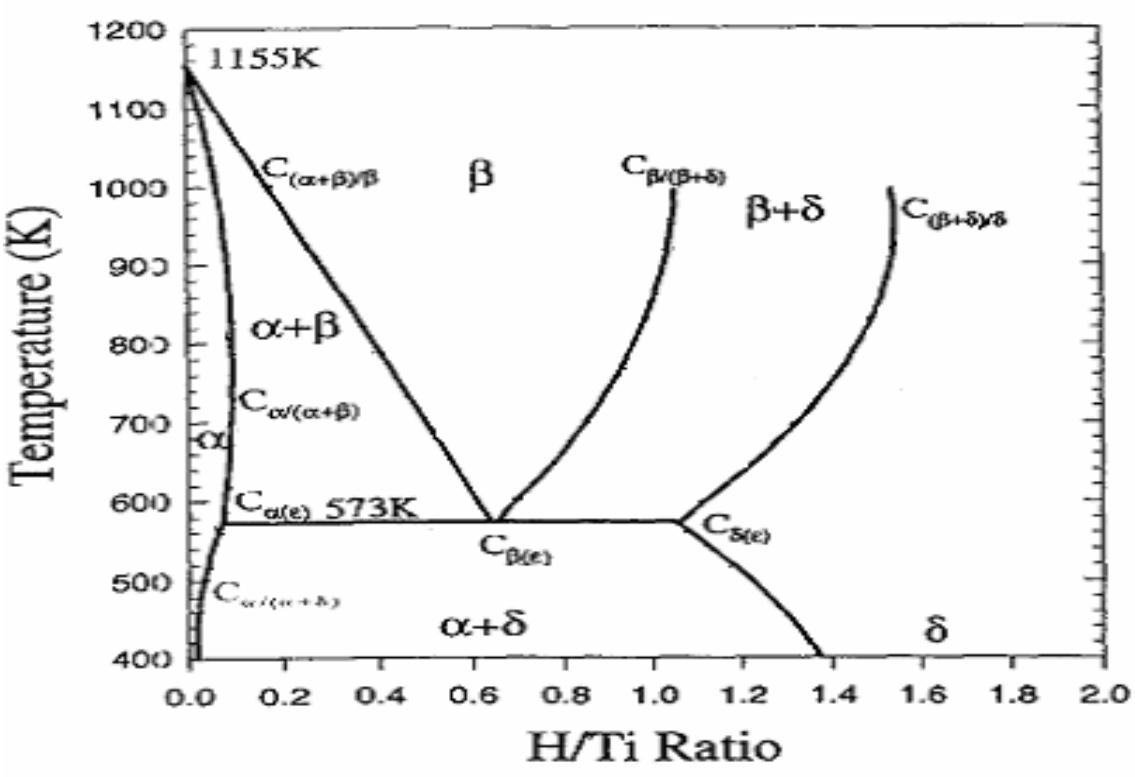

FIGURE 2.2 Metal-hydrogen phase diagrams a) titanium-hydrogen and

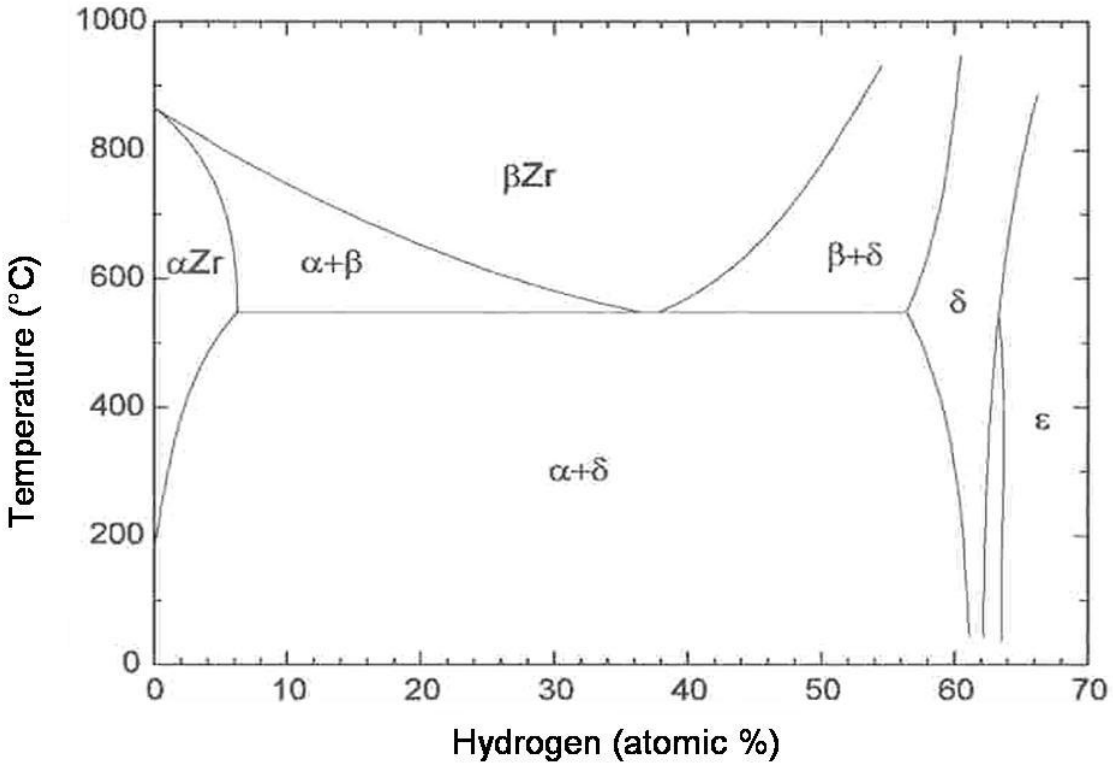

FIGURE 2.2 **Continued** b) the zirconium-hydrogen [30].

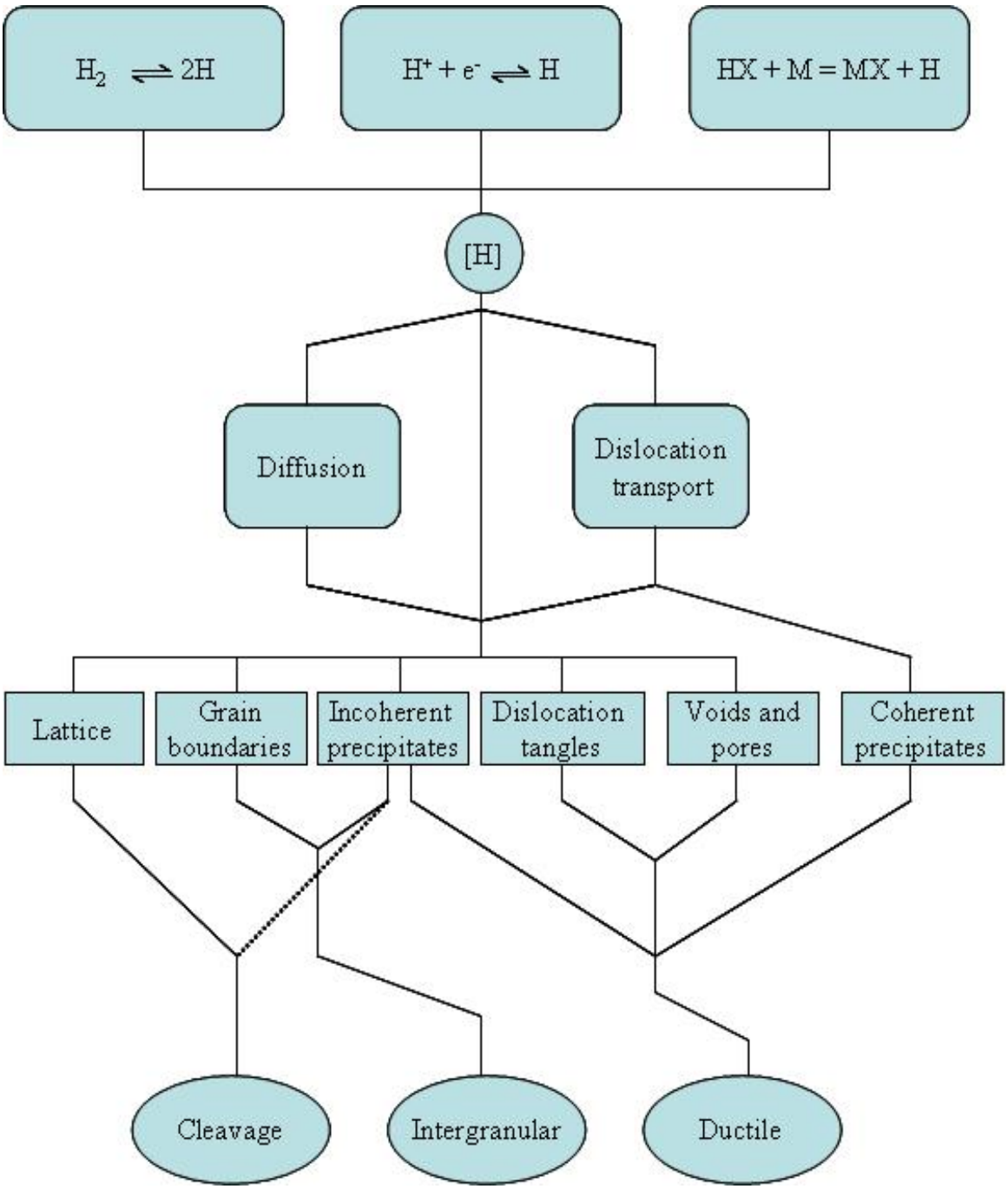

FIGURE 2.3 A flow diagram depicting hydrogen sources, transport paths, destinations, and induced fracture micromechanisms [34].

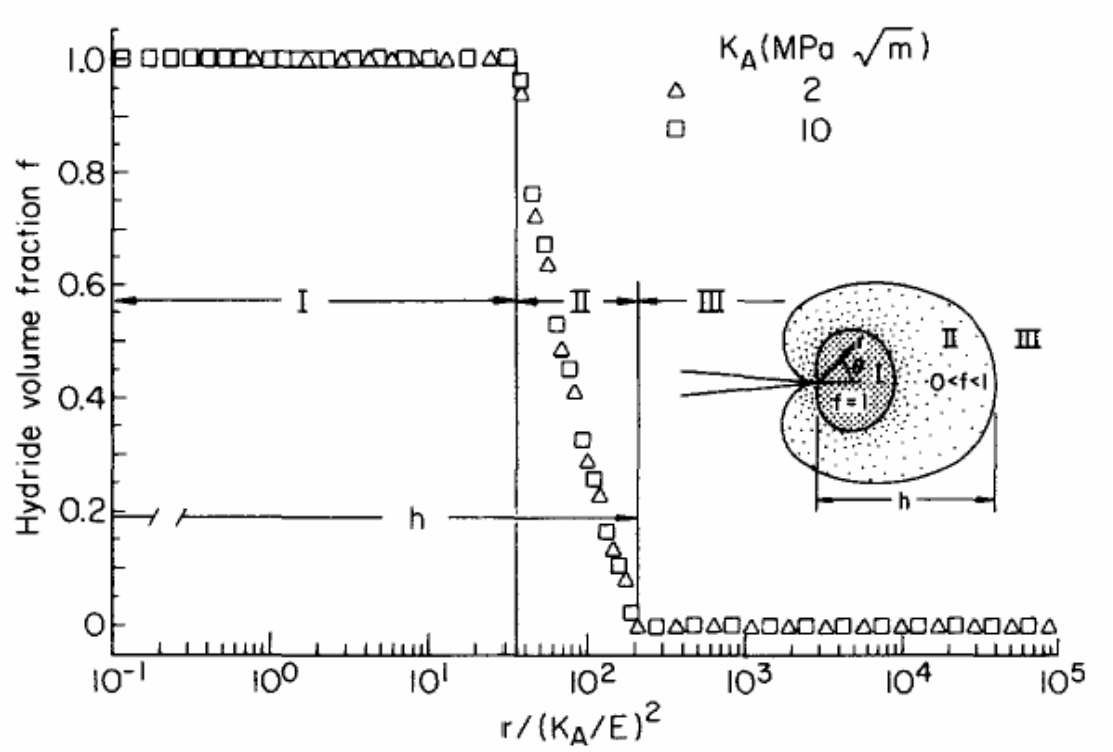

FIGURE 2.4 Plot of the hydride volume fraction, f, versus normalized distance $r/(K_A/E)^2$ ahead of the crack tip at $\theta = 0$ after 100 s when hydride formation reached equilibrium with local stress due to applied loads of $K_A = 2$ and 10 MPa$\sqrt{m}$ and an initial hydrogen concentration of 10^{-3} H/M [73].

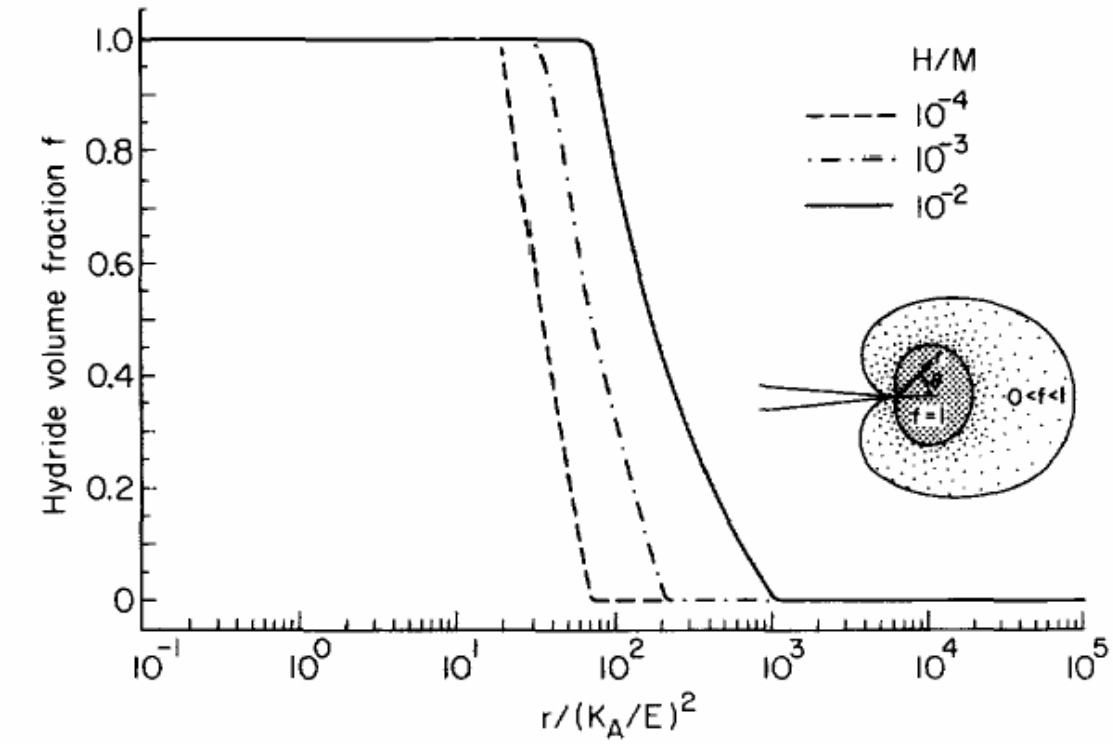

FIGURE 2.5 Plot of the hydride volume fraction, f, in equilibrium with local stress versus normalized distance $r/(K_A/E)^2$ ahead of the crack tip at $\theta = 0$ at various initial concentrations of hydrogen, H/M [73].

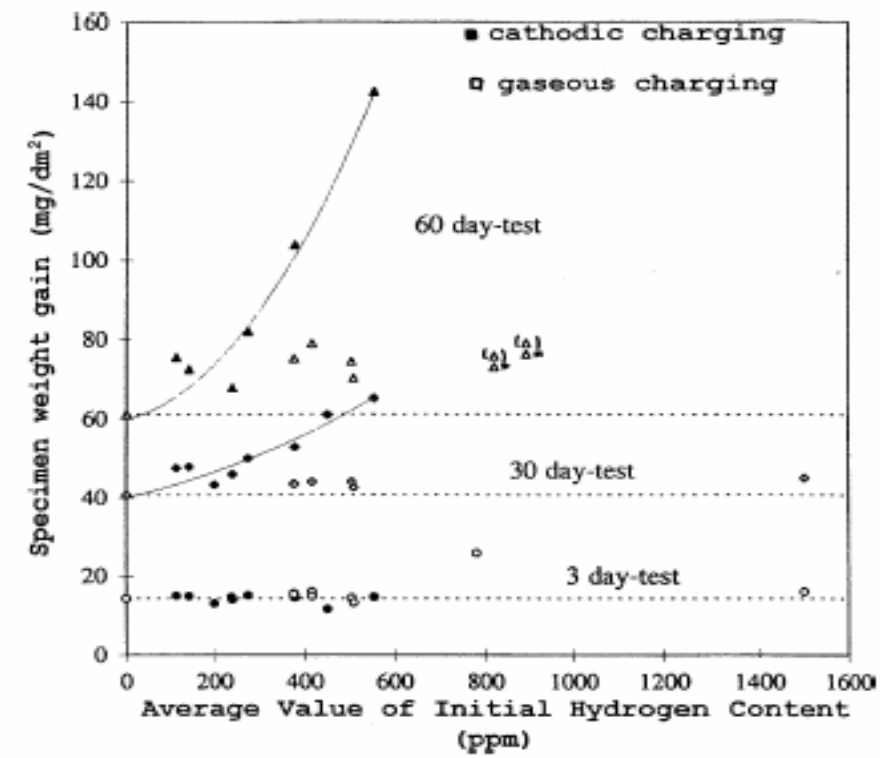

FIGURE 2.6 Influence of the initial hydrogen content on the weight gain of Zr-4 after 400 °C steam corrosion tests [83].

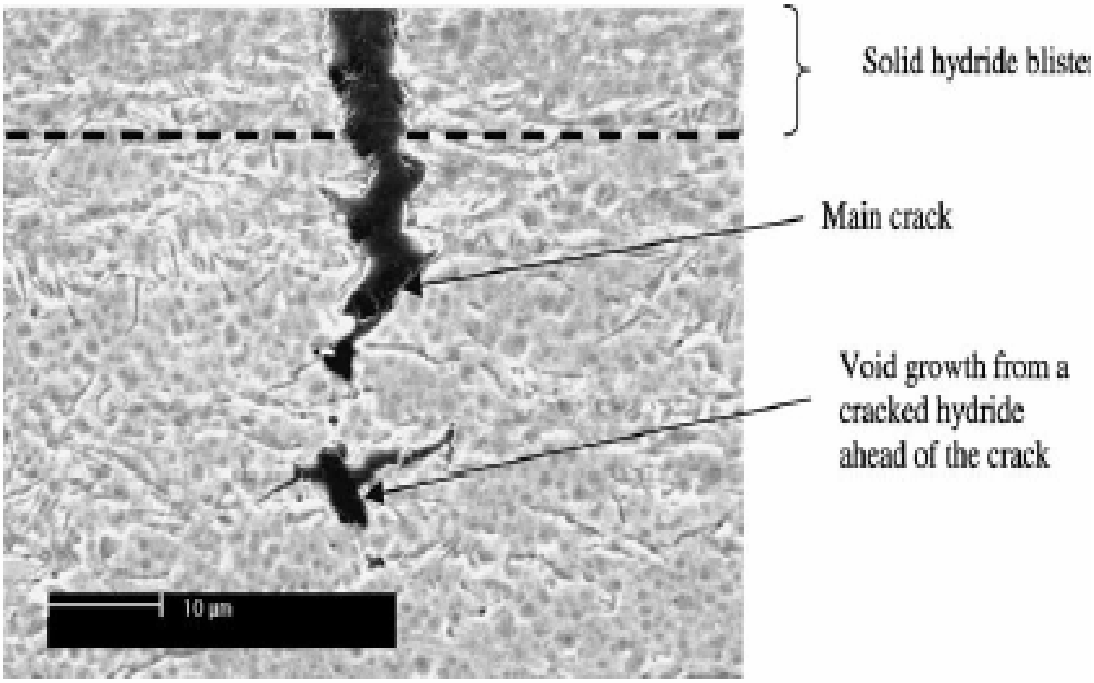

FIGURE 2.7 A light micrograph showing fractured hydrides and void nucleation near the tip of a crack beneath a 200 μm blister in cold worked and stress-relieved (CWSR) Zr-4 deformed at room temperature [84].

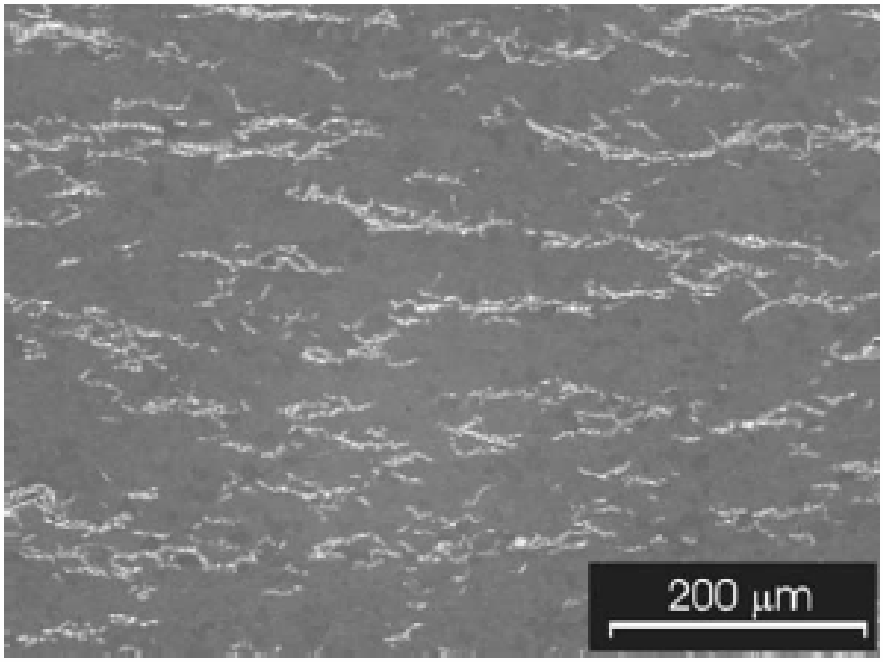

FIGURE 2.8 Distribution of Zr-hydrides platelets [85].

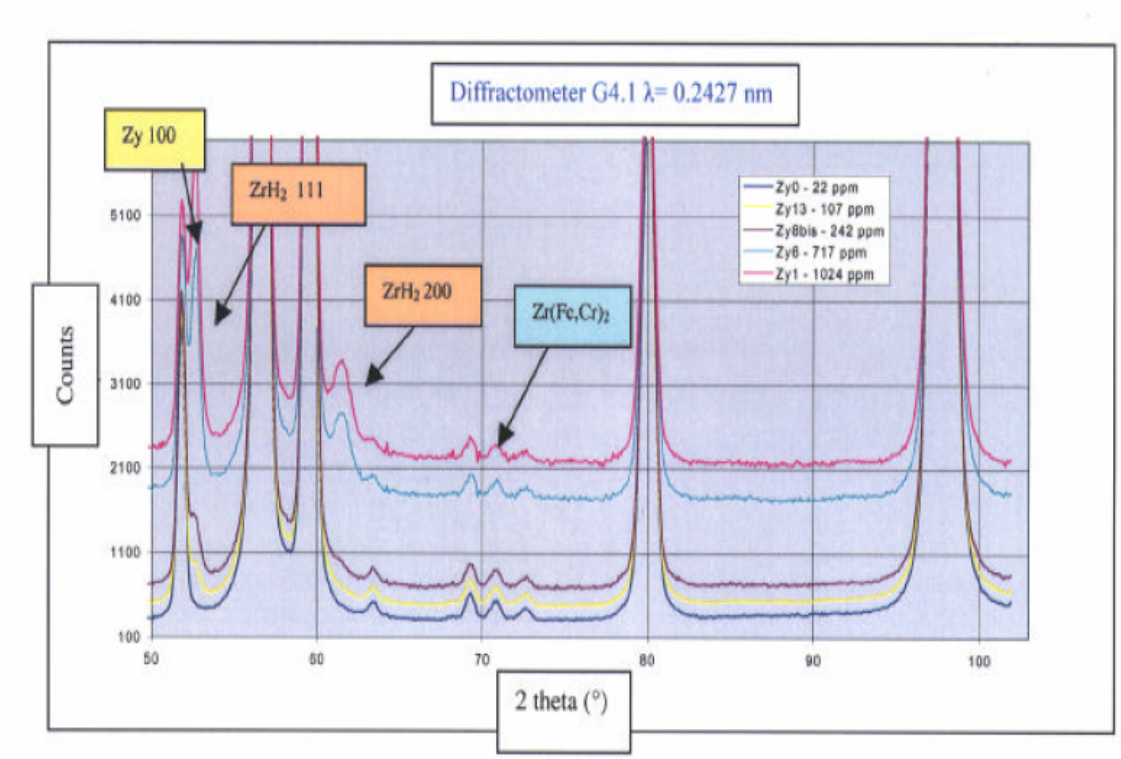

FIGURE 2.9 Powder diffraction diagrams measured for several Zircaloy samples [89].

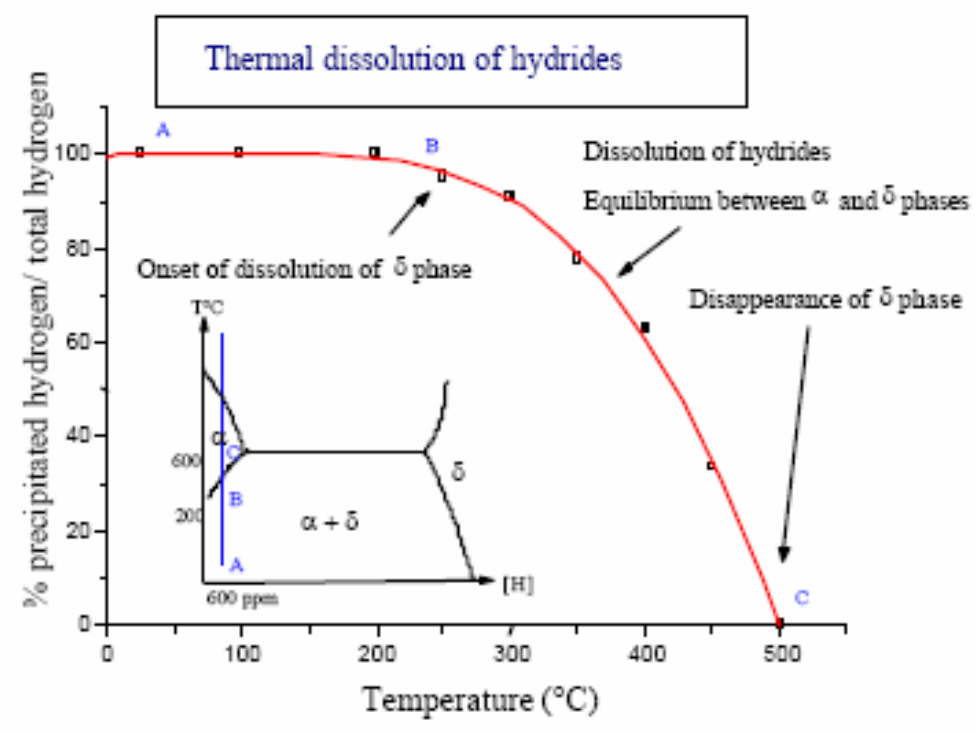

FIGURE 2.10 Proportion of hydrogen content in hydride form (δ-phase) versus temperature for a sample containing 642 ppm weight hydrogen [89].

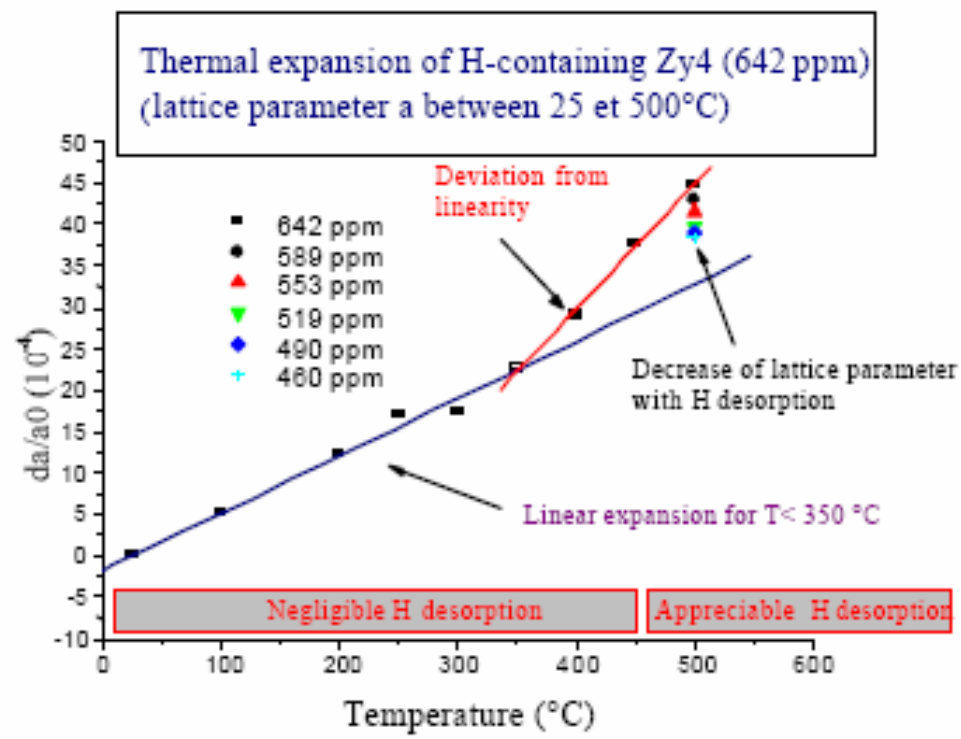

FIGURE 2.11 Temperature dependence of the lattice parameter *a* of Zr-4 (sample containing 642 ppm weight hydrogen) [89].

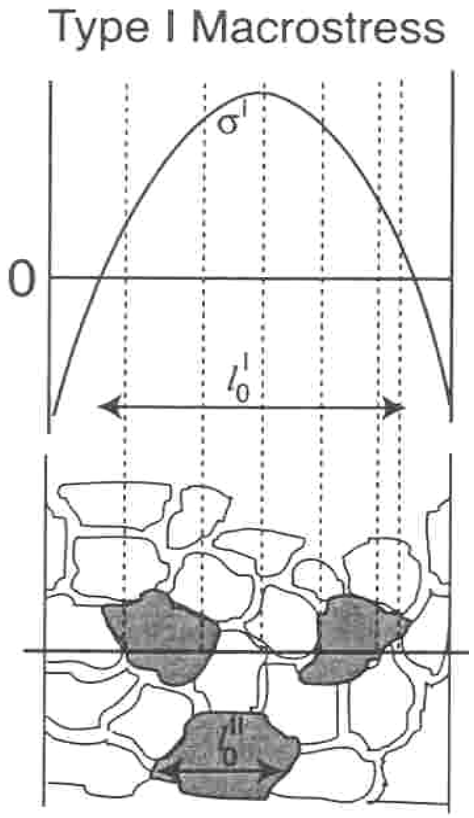

FIGURE 2.12 Type I stress varies on a length scale l_o^I, which is a considerable fraction of the sample size. Type I stresses are considered to be continuous even across grains and phase boundaries [98].

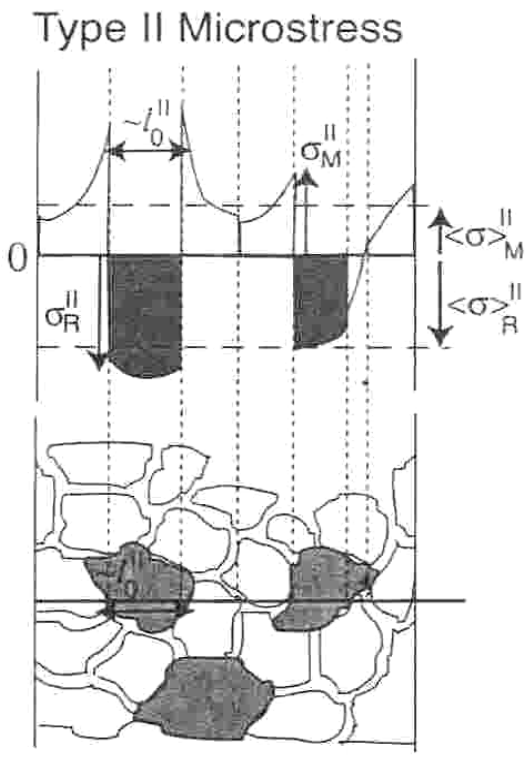

FIGURE 2.13 Type II stress varies on a length scale l_o^{II}, which is on the order of the grain size [98].

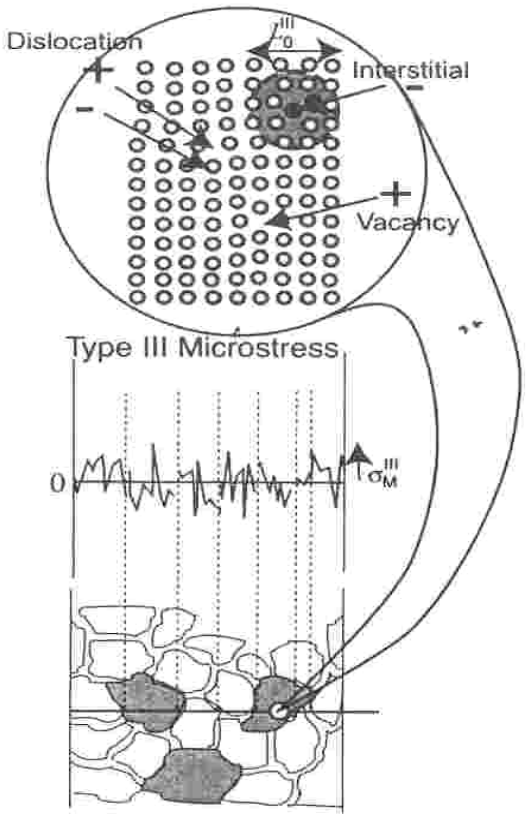

FIGURE 2.14 Type III stress varies on a subgrain scale l_o^{III}, which is smaller than the grain size [98].

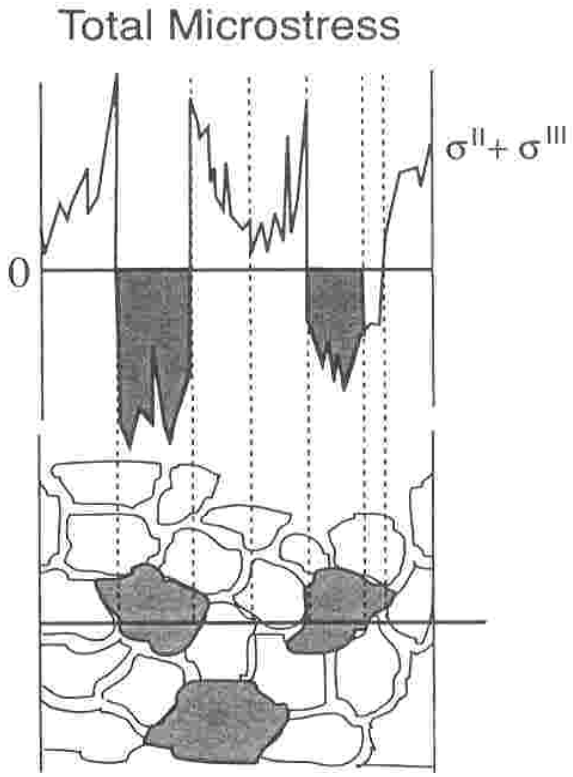

FIGURE 2.15 Type II and Type III stresses are often grouped together and termed microstresses as shown here [98].

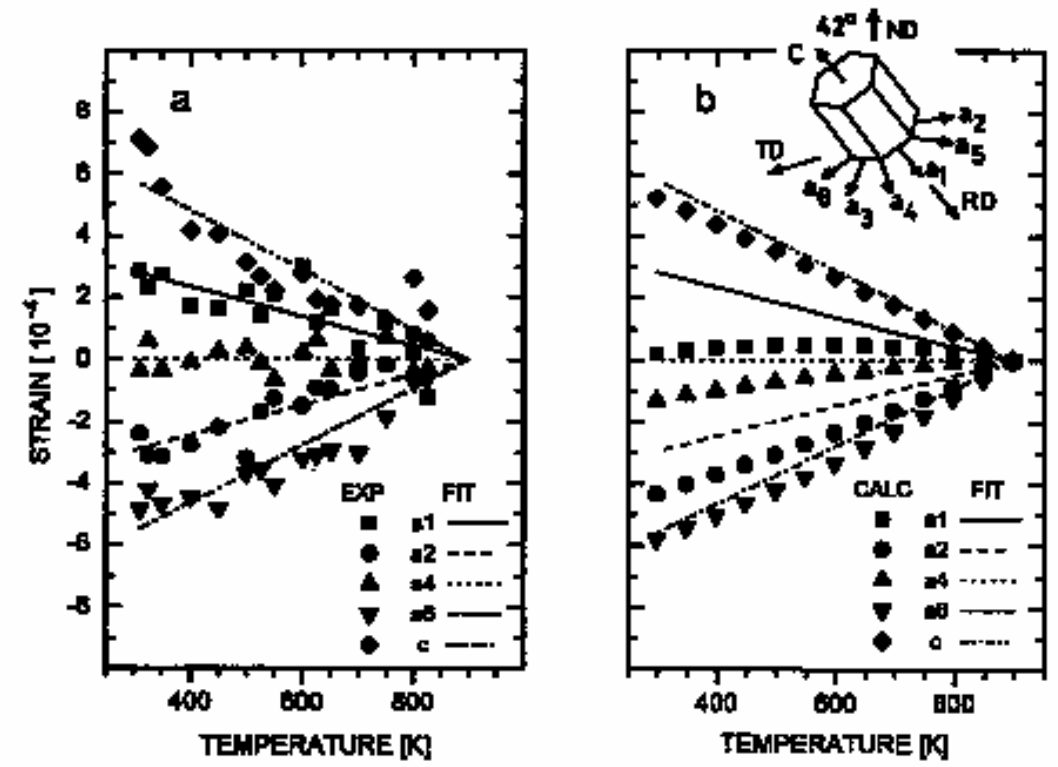

FIGURE 2.16 Elastic strain versus temperature in basal and prismatic planes oriented along the directions indicated in the inset (a) calculated from experimental measurements of spacings and (b) predicted by the self-consistent thermo-elastic formulation. Parameters used in the calculation: a_{sf} (298 K) = 0.323056 nm, c_{sf} (298 K) = 0.514960 nm, $\alpha_a = 5.7$ and $\alpha_c = 10.3 \times 10^{-6} K^{-1}$ [102].

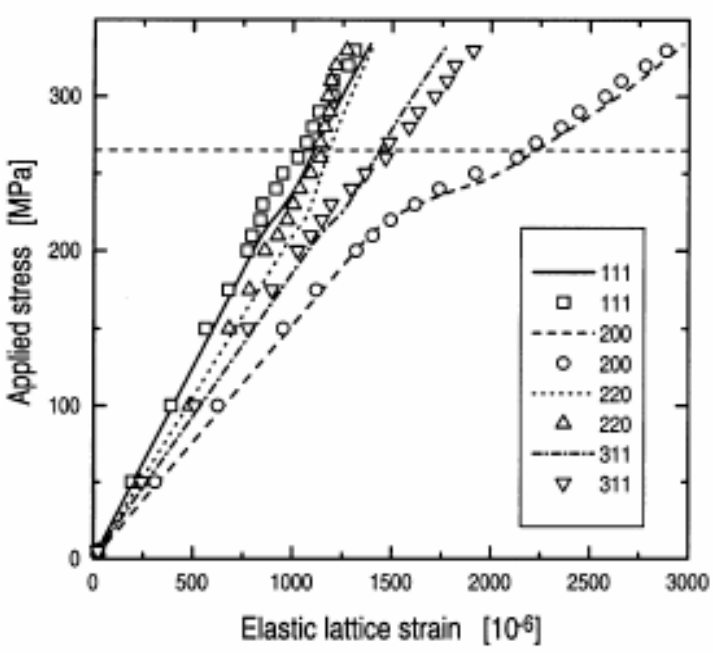

(a) Parallel to the tensile axis

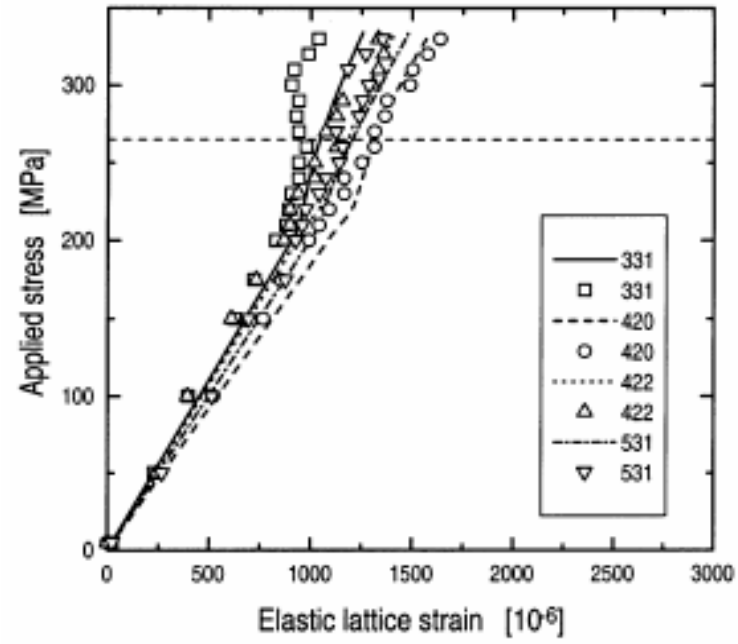

(b) Parallel to the tensile axis

FIGURE 2.17 The applied stress versus the elastic lattice strain. Symbols are measured and lines are calculated. For clarity the data is presented in two graphs for parallel (a, b) to the tensile axis. The horizontal dotted line represents the macroscopic 0.2% yield limit,

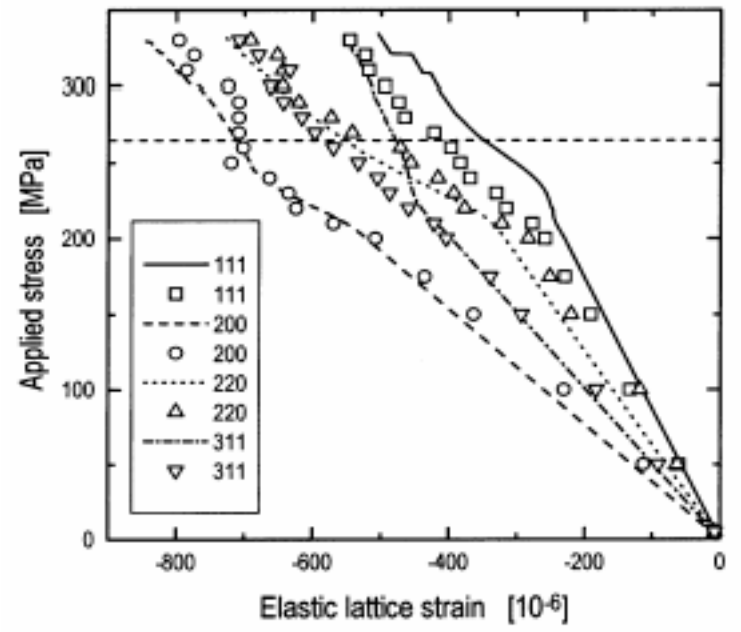

(c) Perpendicular to the tensile axis

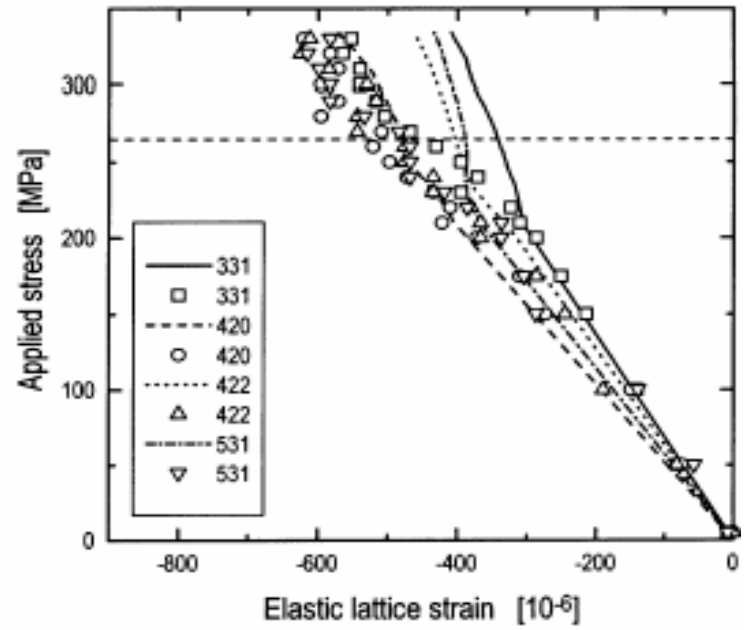

(d) Perpendicular to the tensile axis

FIGURE 2.17 Continued (c, d) two graphs for perpendicular to tensile axis [103].

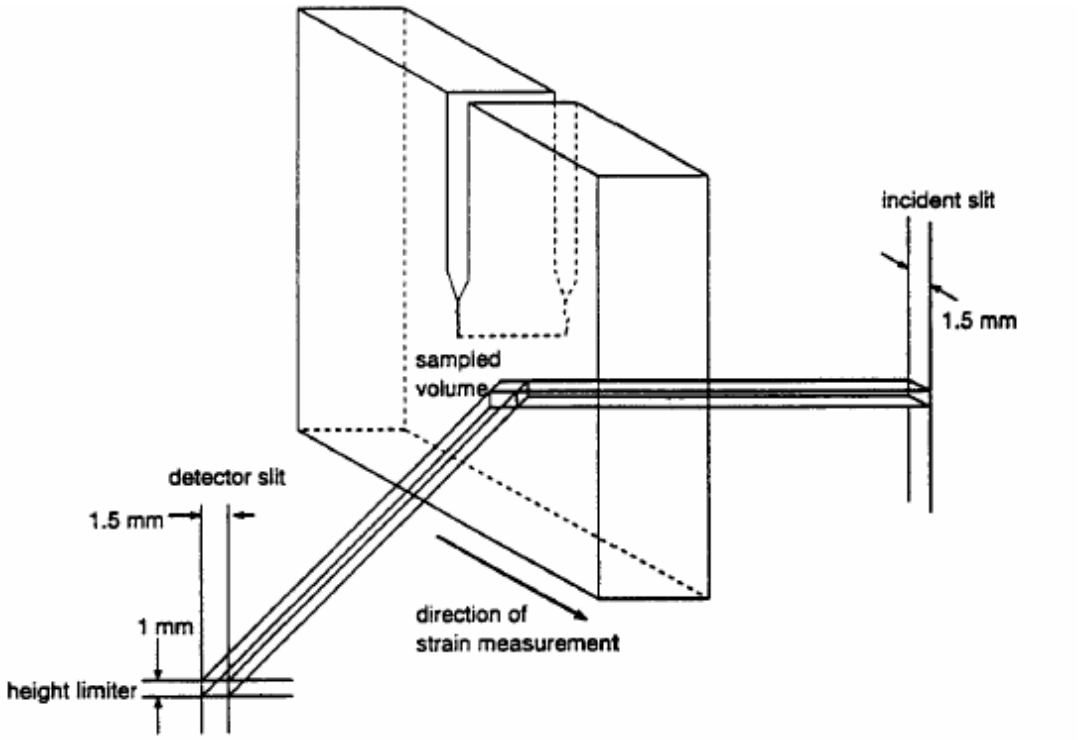

FIGURE 2.18 Specimen configuration for strain measurement parallel to the load line [104].

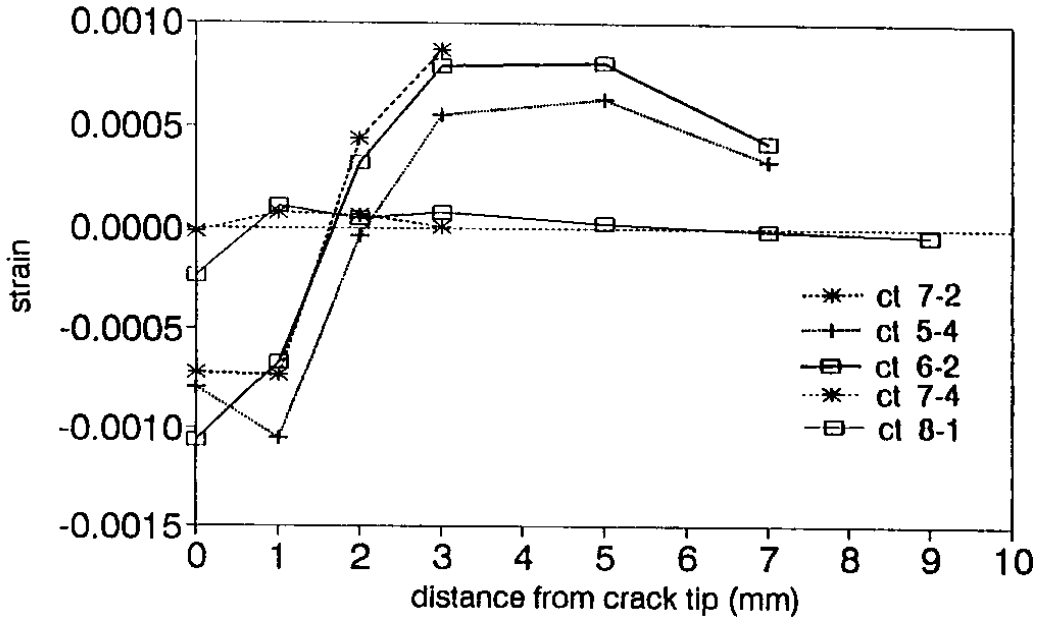

FIGURE 2.19 Residual elastic strains [104].

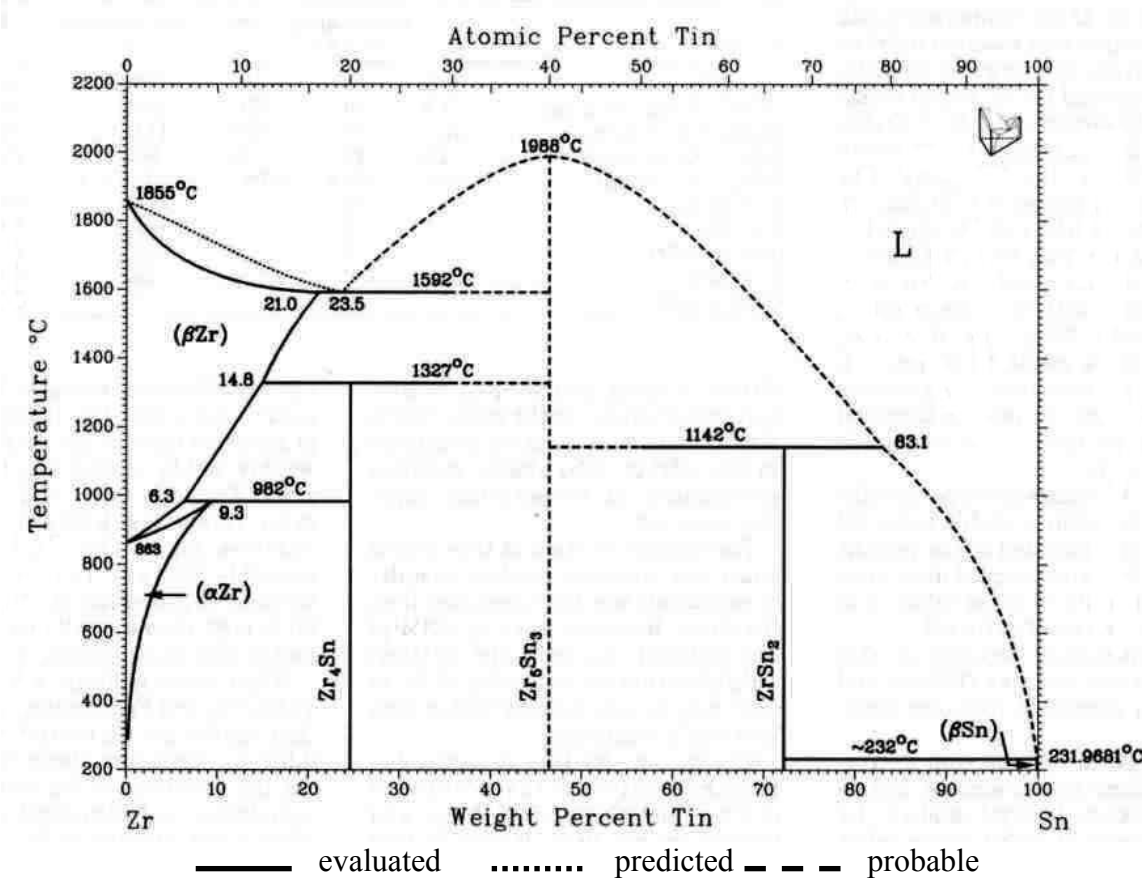

FIGURE 3.1 Zirconium-tin phase diagram [105].

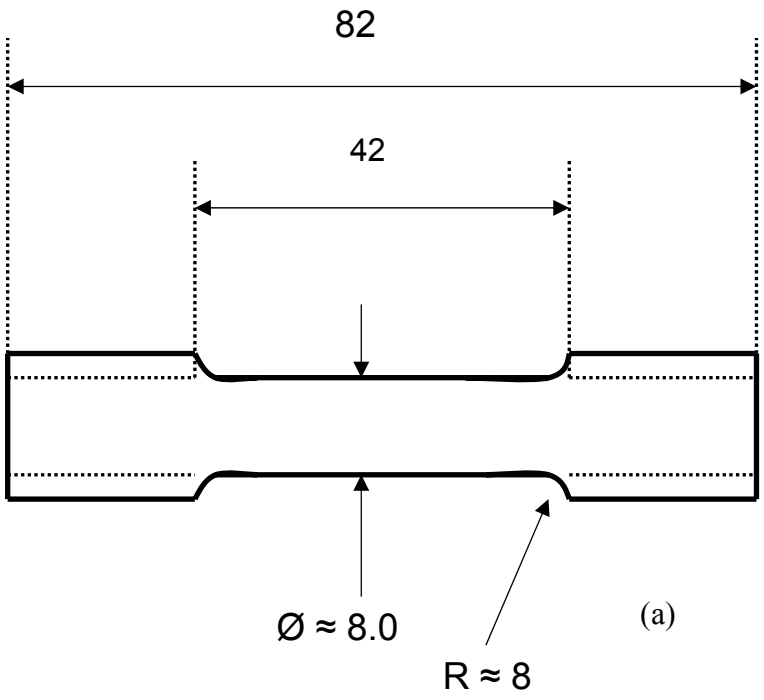

FIGURE 3.2 Round-bar tensile specimen (a) drawing and dimensions (units in mm),

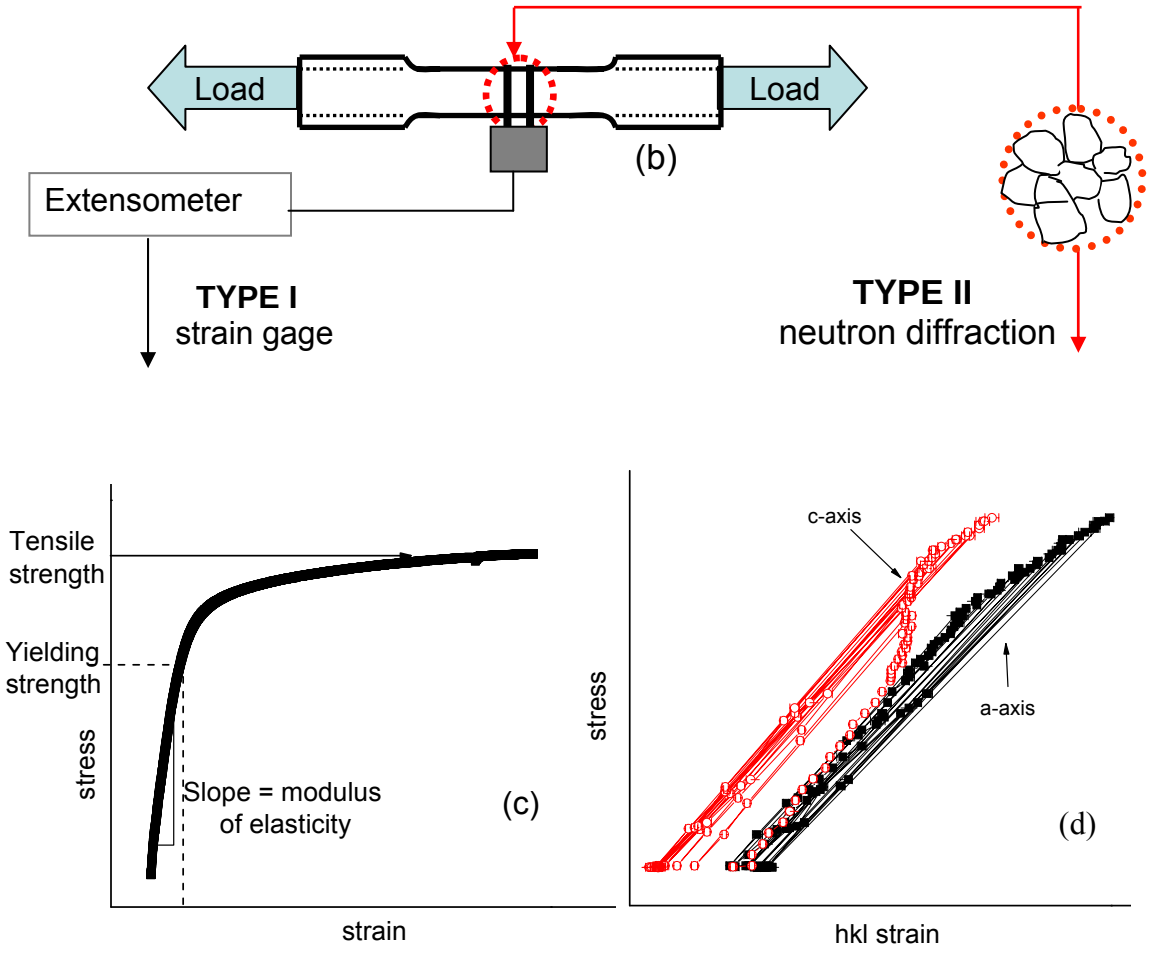

FIGURE 3.2 Continued (b) schematic of a tensile specimen with an extensometer attached, (c) typical macroscopic stress-strain curve obtained from a tensile test, and (d) typical microstrain development for two reflections corresponding to lattice stains *a* and *c*.

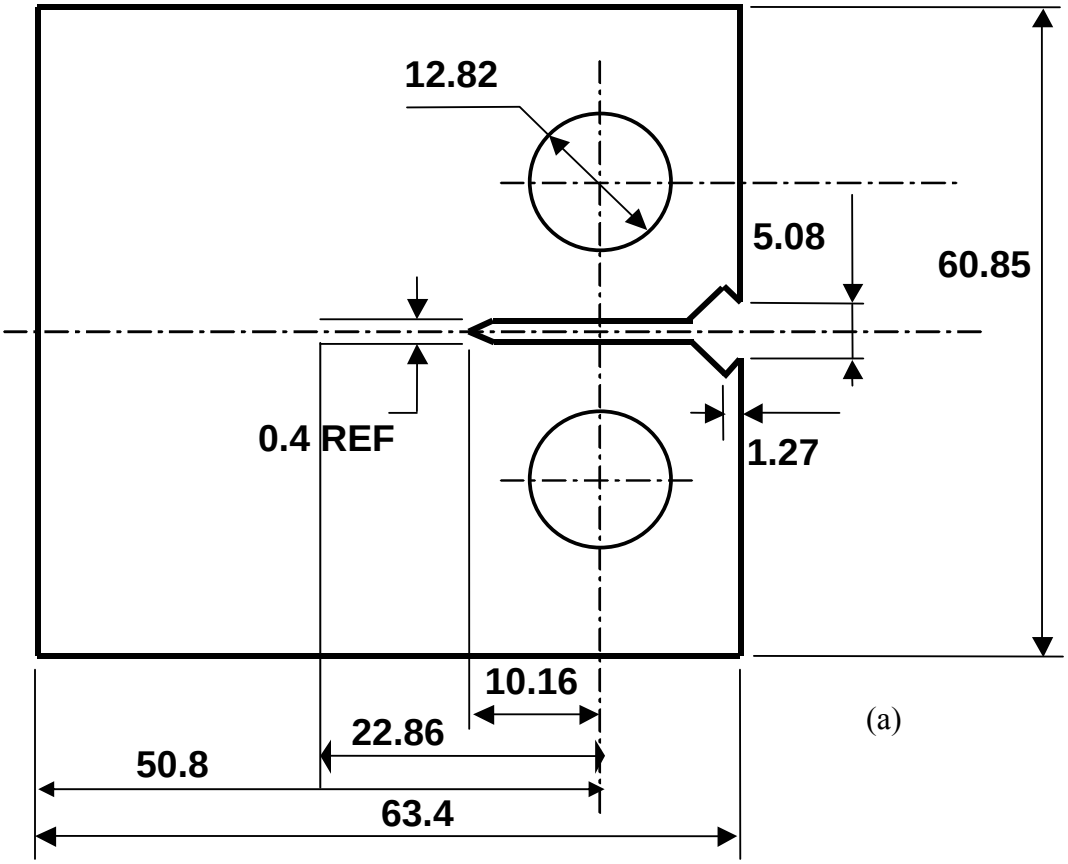

FIGURE 3.3 Compact-tension (CT) specimen (a) drawing and dimensions (units in mm). Thickness = 6.4 mm,

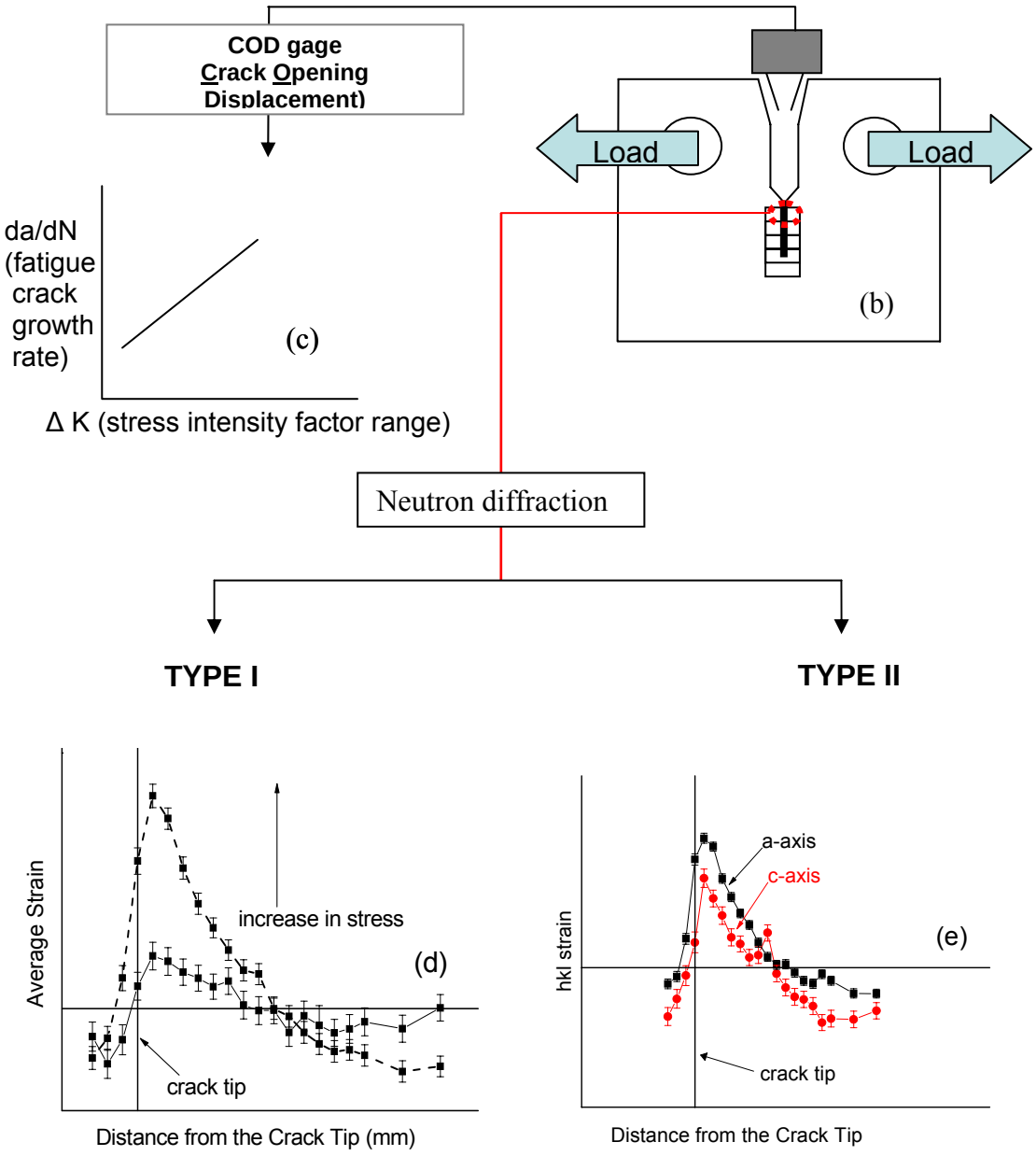

FIGURE 3.3 **Continued** (b) schematic of a CT specimen with a COD gage attached (c) fatigue behavior, represented by the fatigue crack growth rate with respect to the stress intensity factor range, (d) average strain profile in front of a crack tip, and (e) microstrain development for two reflections corresponding to lattice stain *a* and *c*.

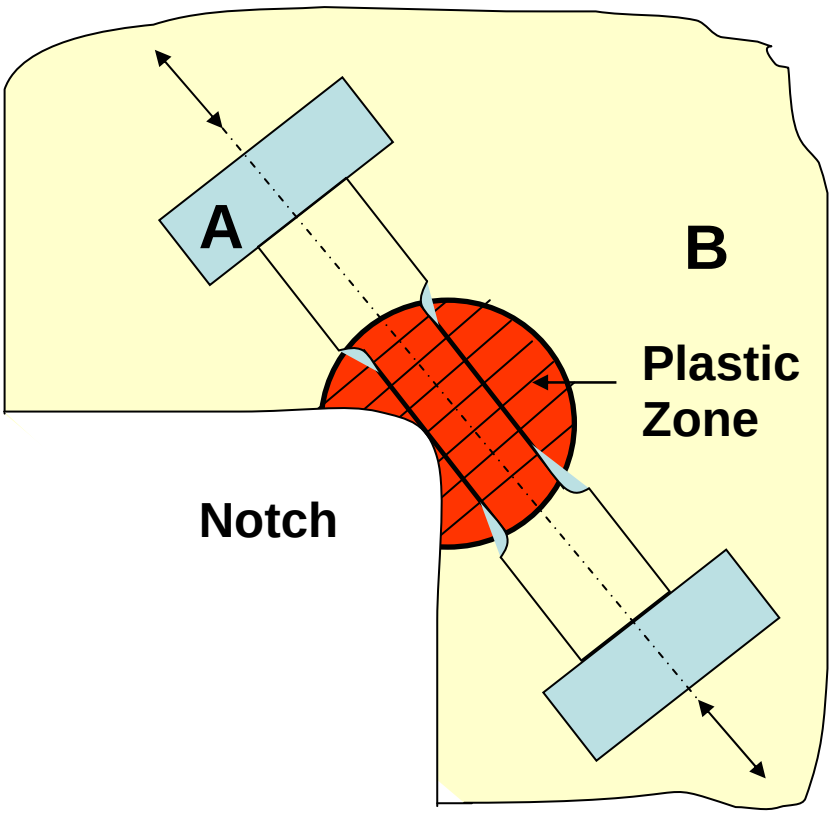

FIGURE 3.4 Model of plastic deformations in tensile specimen (A), CT specimen (B), and their correlation.

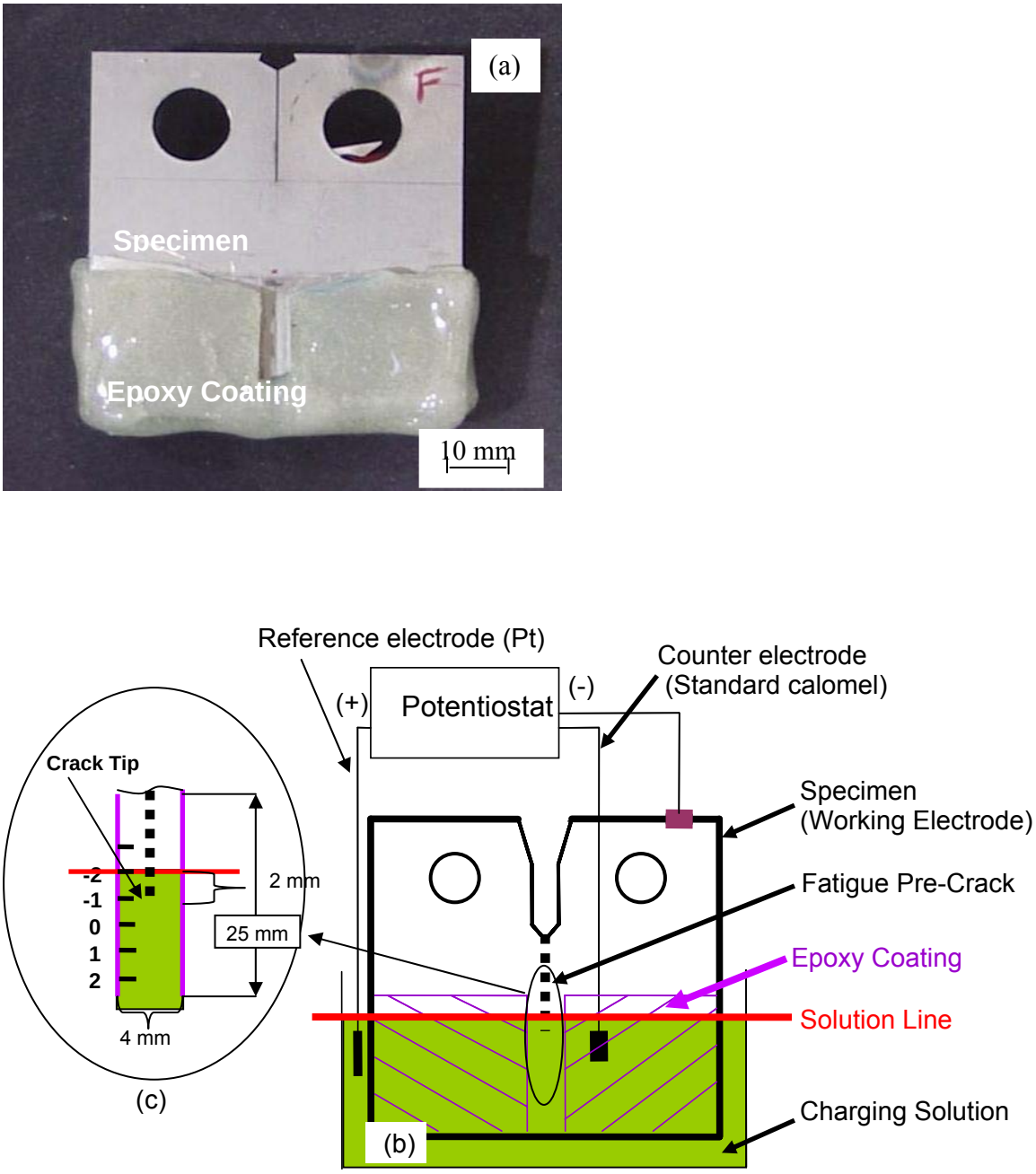

FIGURE 3.5 Electrochemical hydrogen charged setup (a) picture of CT specimen with epoxy coating, (b) schematic of the electrochemical cell, and (c) magnified image showing the crack in the electrolyte.

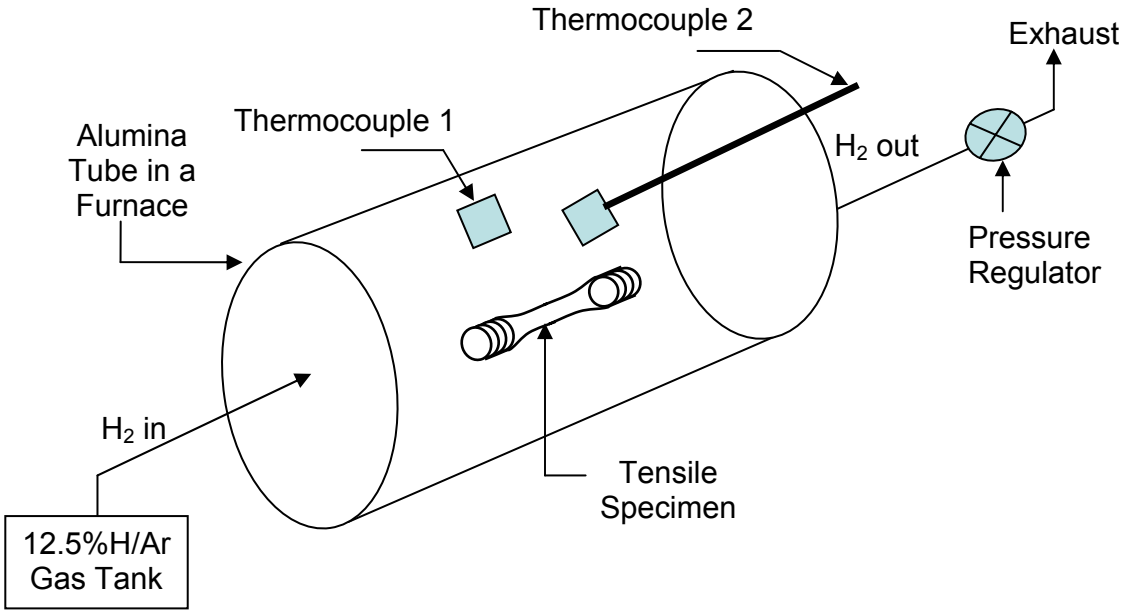

FIGURE 3.6 Schematic of the tube furnace setup for hydrogen-gas charging.

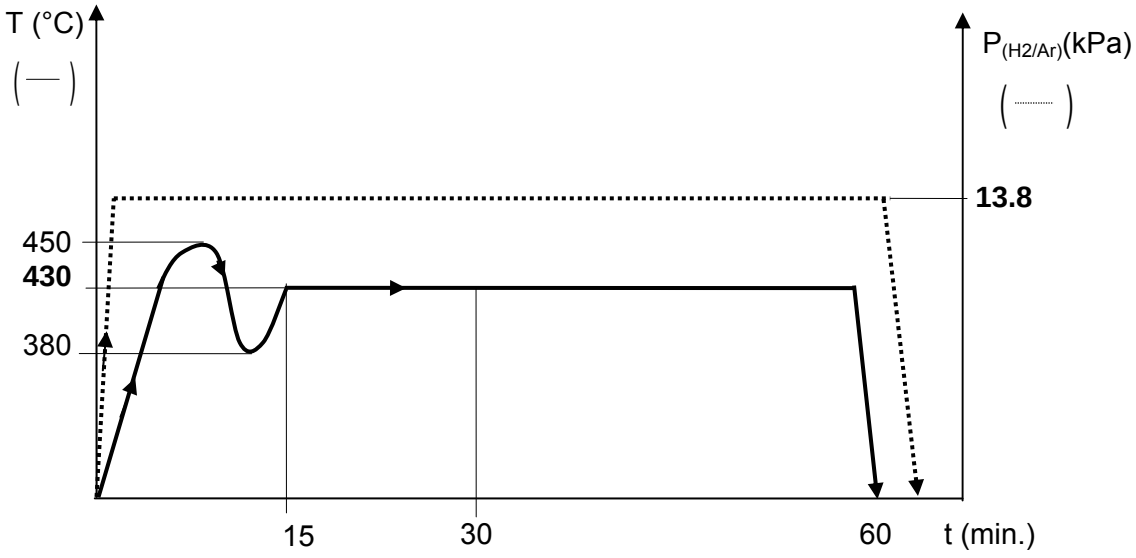

FIGURE 3.7 Temperature-time-pressure diagrams for the hydrogen-gas charging.

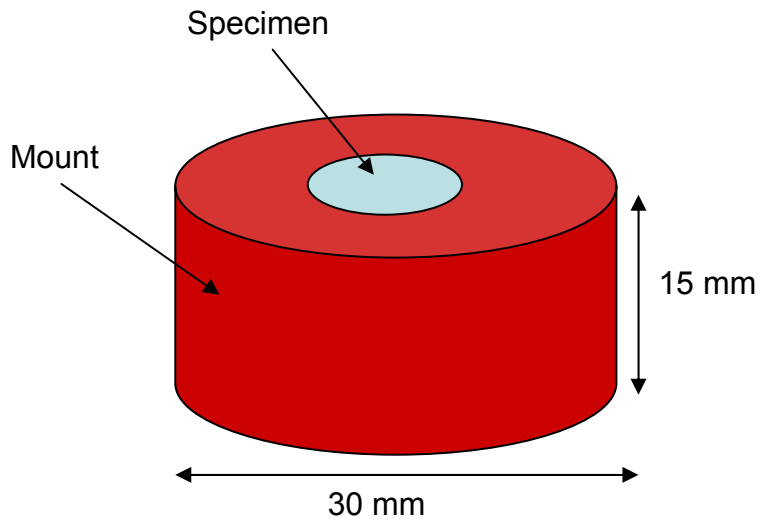

FIGURE 3.8 A mounted specimen in cold-setting epoxy (shows typical dimensions).

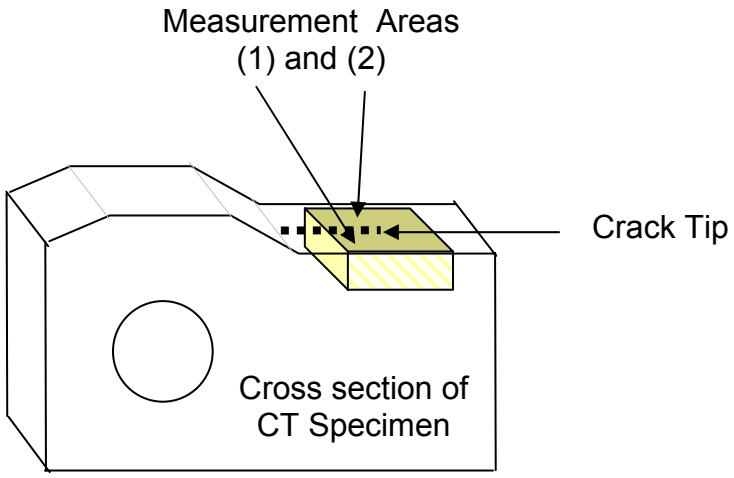

FIGURE 3.9 Optical microscopy measurement area on a cross-section of specimen charged electrochemically with hydrogen.

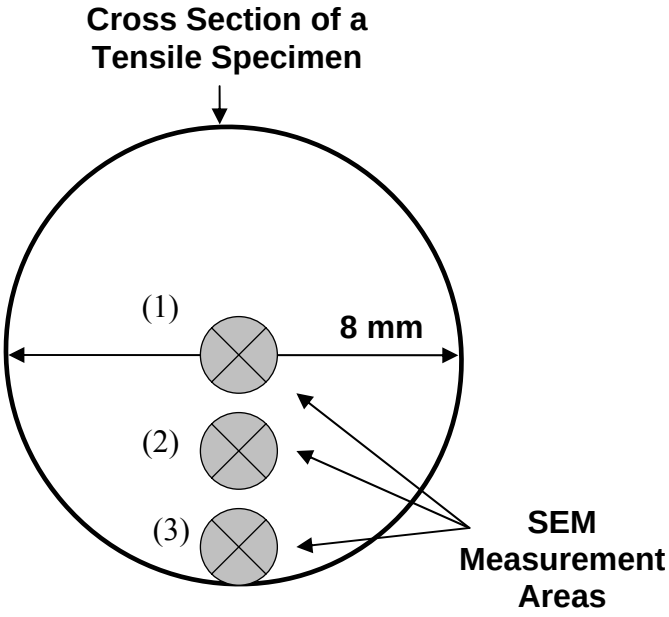

FIGURE 3.10 Top view of SEM measurement positions on a cross-section of specimen charged with hydrogen gas.

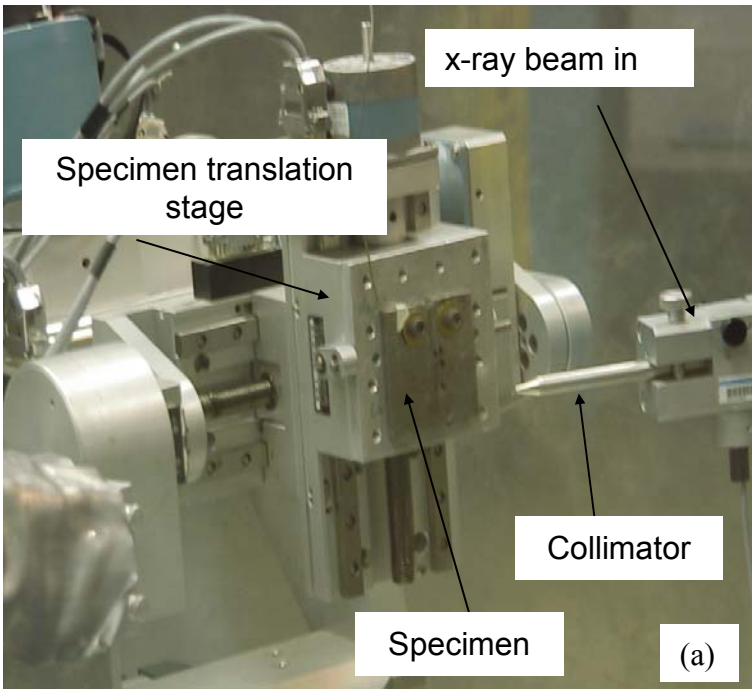

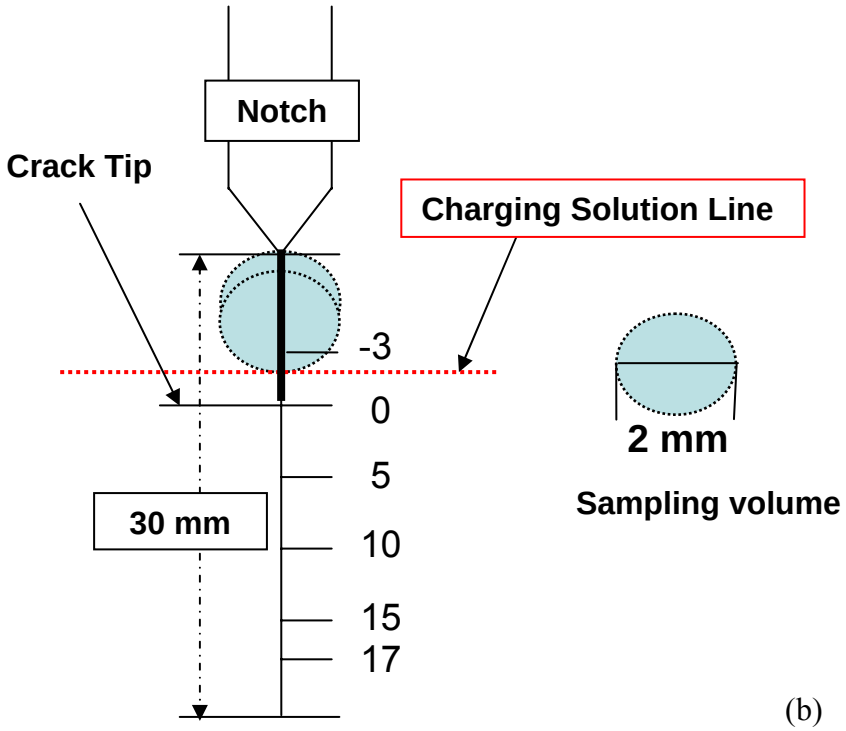

FIGURE 3.11 X-ray diffraction measurement setup (a) picture of the CT specimen mounted on the Rotating Anode Diffractometer at Los Alamos Neutron Science Center and (b) x-ray diffraction measurement positions along the crack.

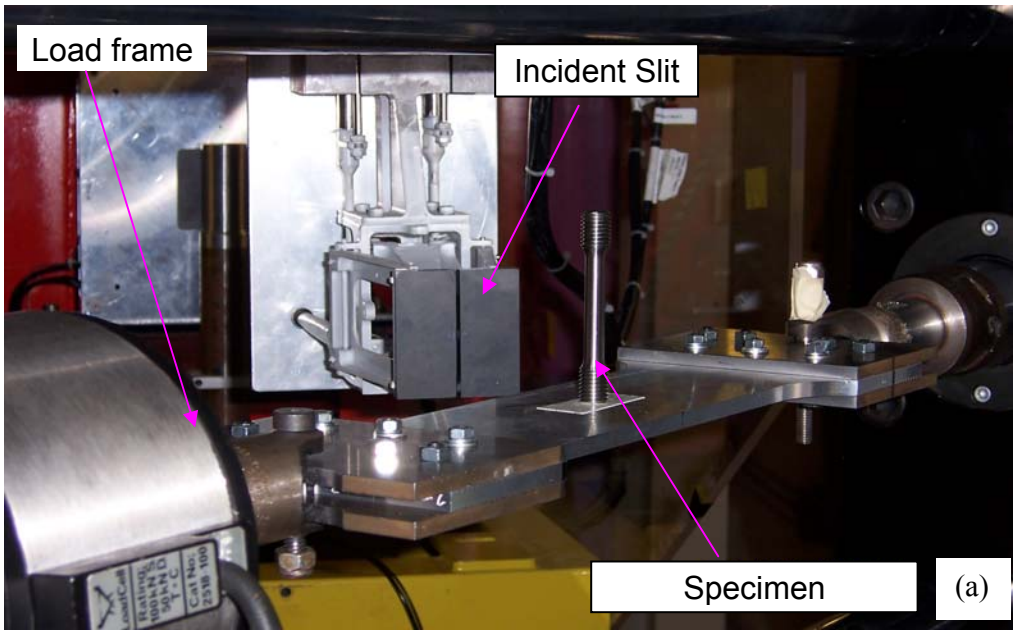

FIGURE 3.12 Phase mapping of the tensile specimens using ENGIN-X instrument (a) picture of neutron-diffraction phase mapping measurement setup,

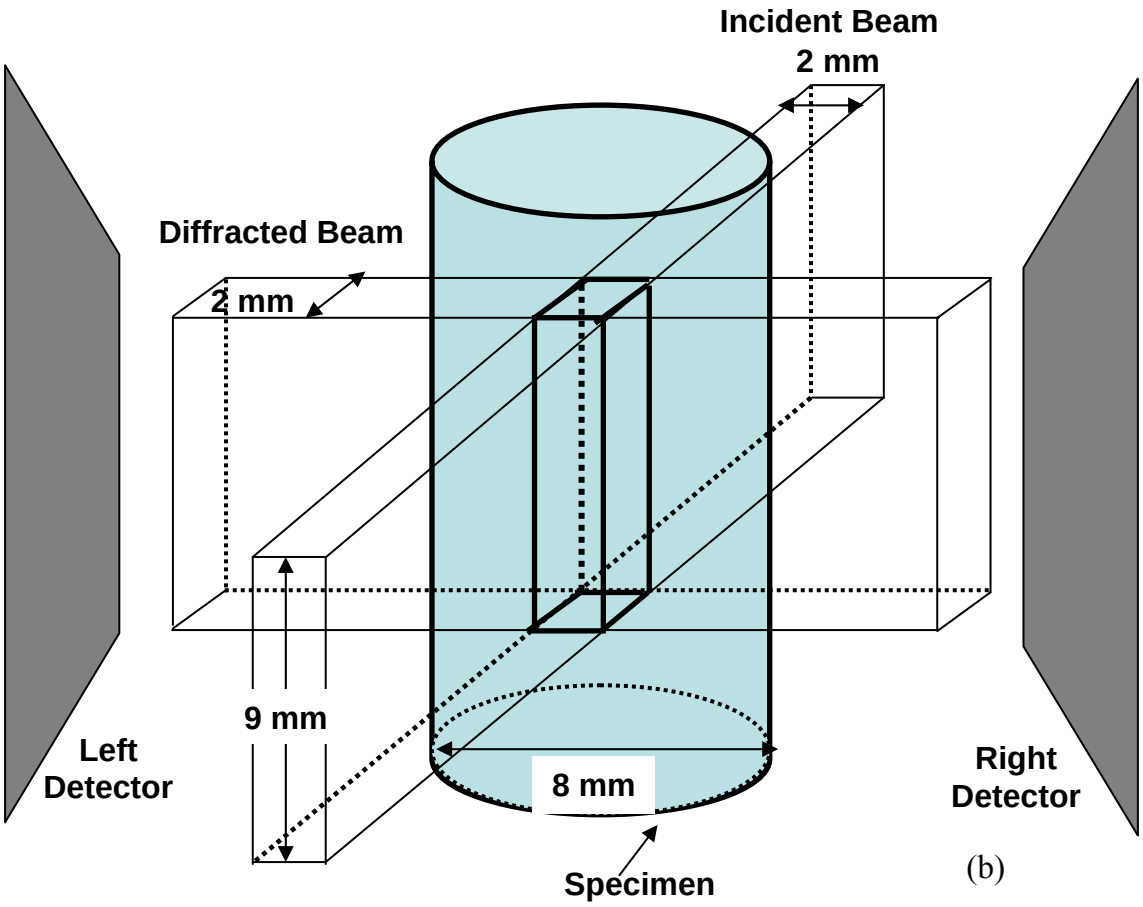

FIGURE 3.12 Continued (b) perspective view of the sample with the neutron sampling volume of 2 x 9 x 2 mm^3, and

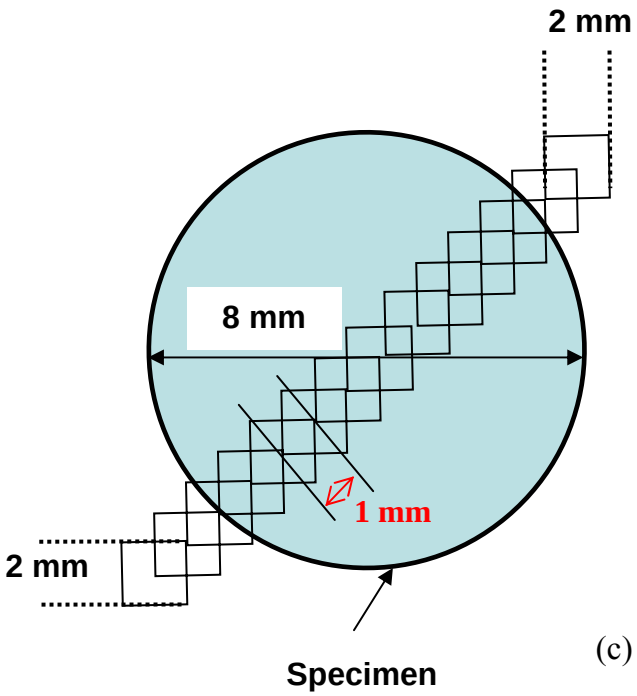

(c)

FIGURE 3.12 **Continued** (c) top view of the measurement points across the diameter at 1-mm interval.

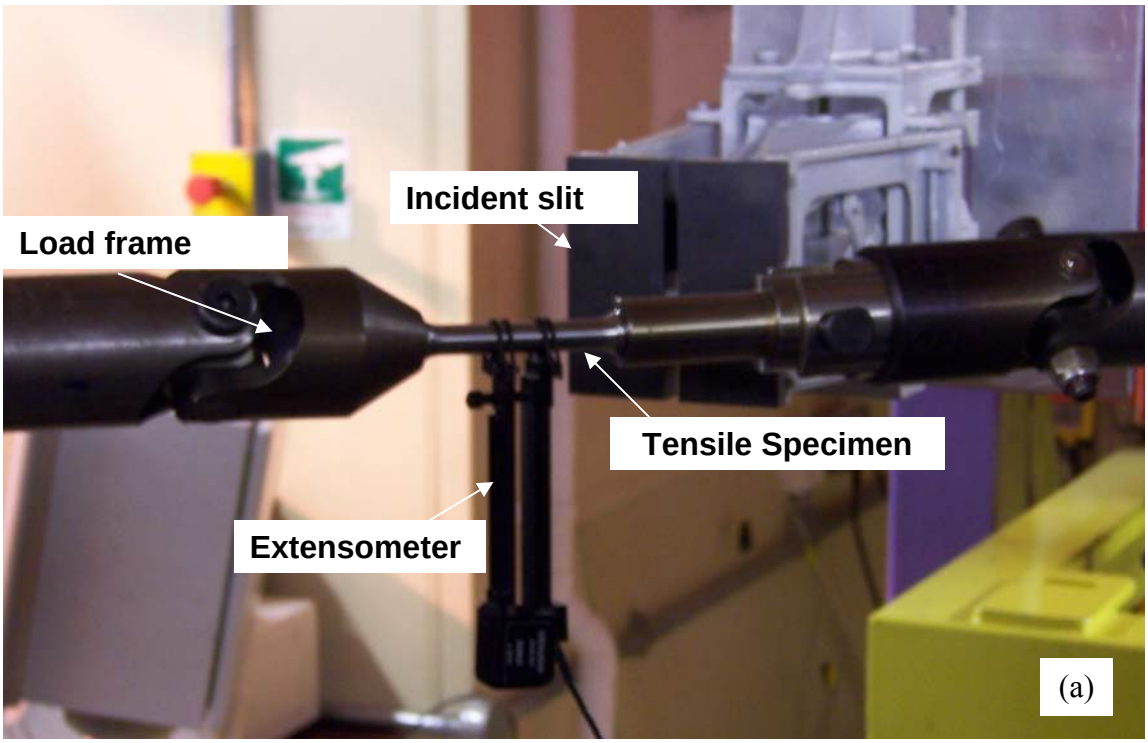

FIGURE 3.13 Tensile strain measurement using ENGIN-X instrument (a) picture of the tensile specimen with an extensometer attached,

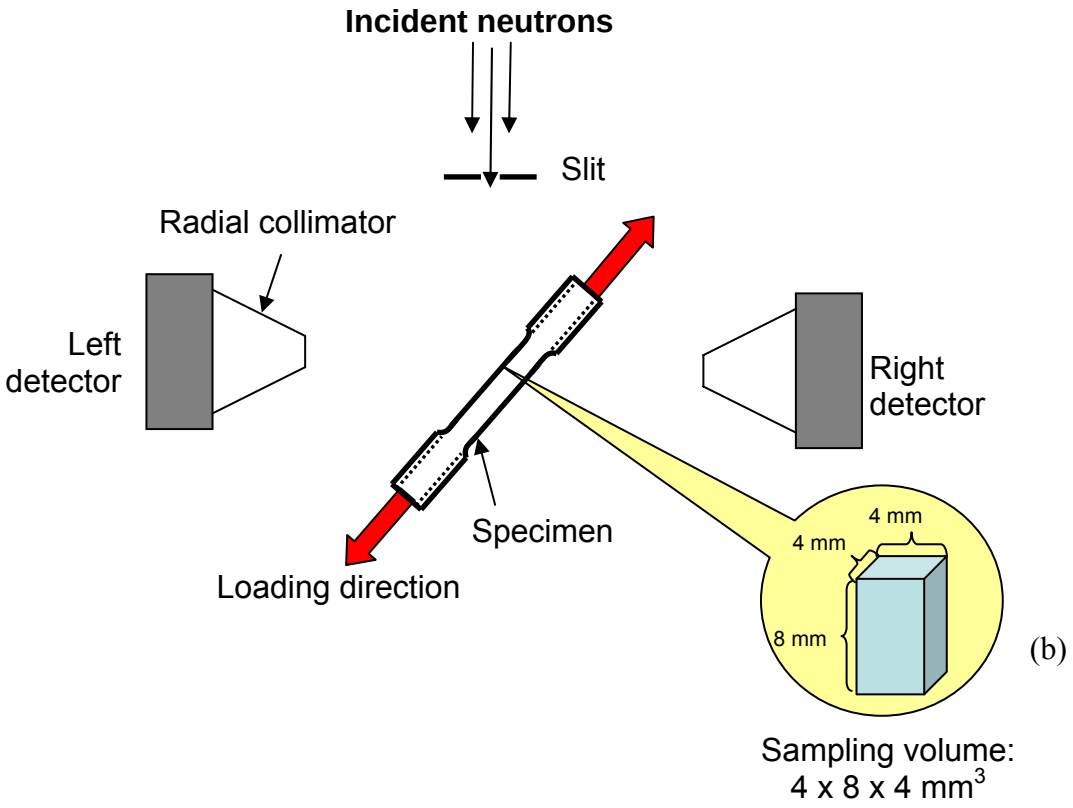

FIGURE 3.13 **Continued** (b) plan view of the schematic strain measurement setup with the sampling volume of 4 mm x 8 mm x 4 mm,

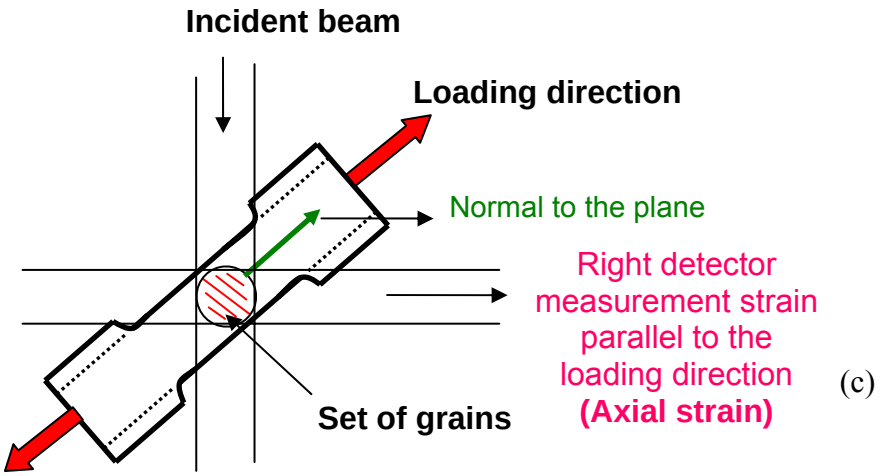

(c)

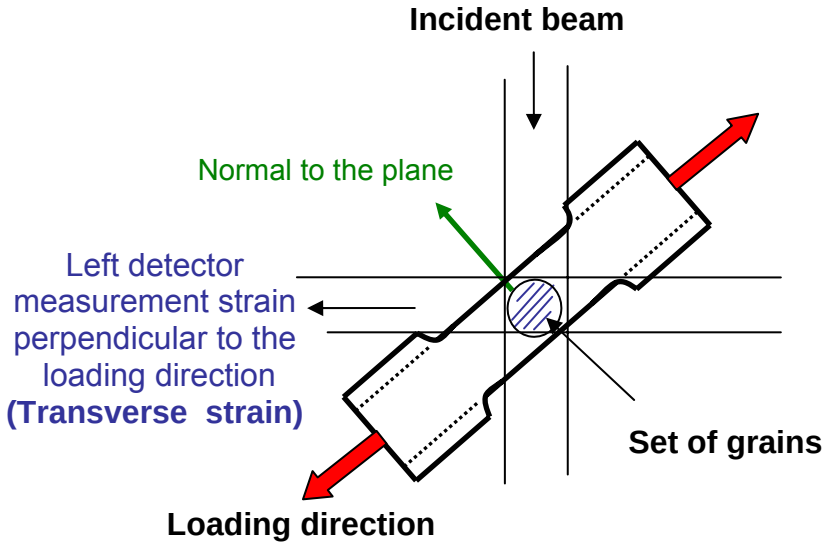

(d)

FIGURE 3.13 **Continued** (c) axial strain measurement, and (d) transverse strain measurement.

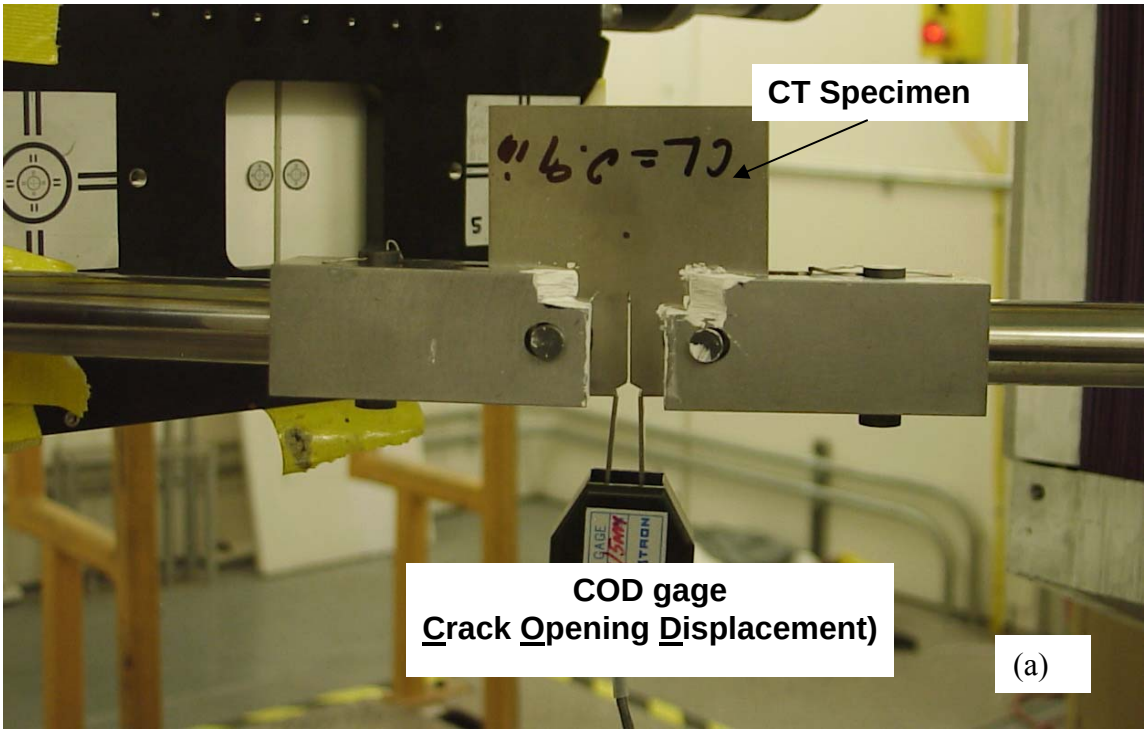

FIGURE 3.14 Phase mapping of the CT specimens using SMARTS instrument, (a) picture of the CT specimen in front of the neutron beam and

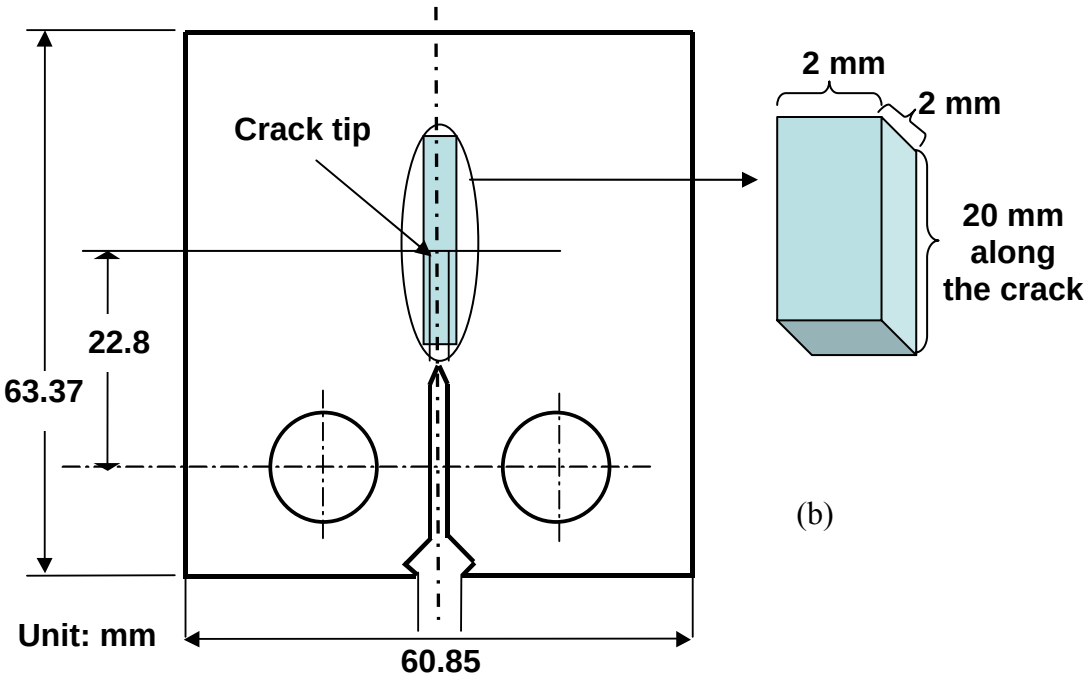

FIGURE 3.14 Continued (b) schematic of specimen configuration for neutron phase mapping through its thickness with a sampling volume of 2 x 20 x 2 mm^3.

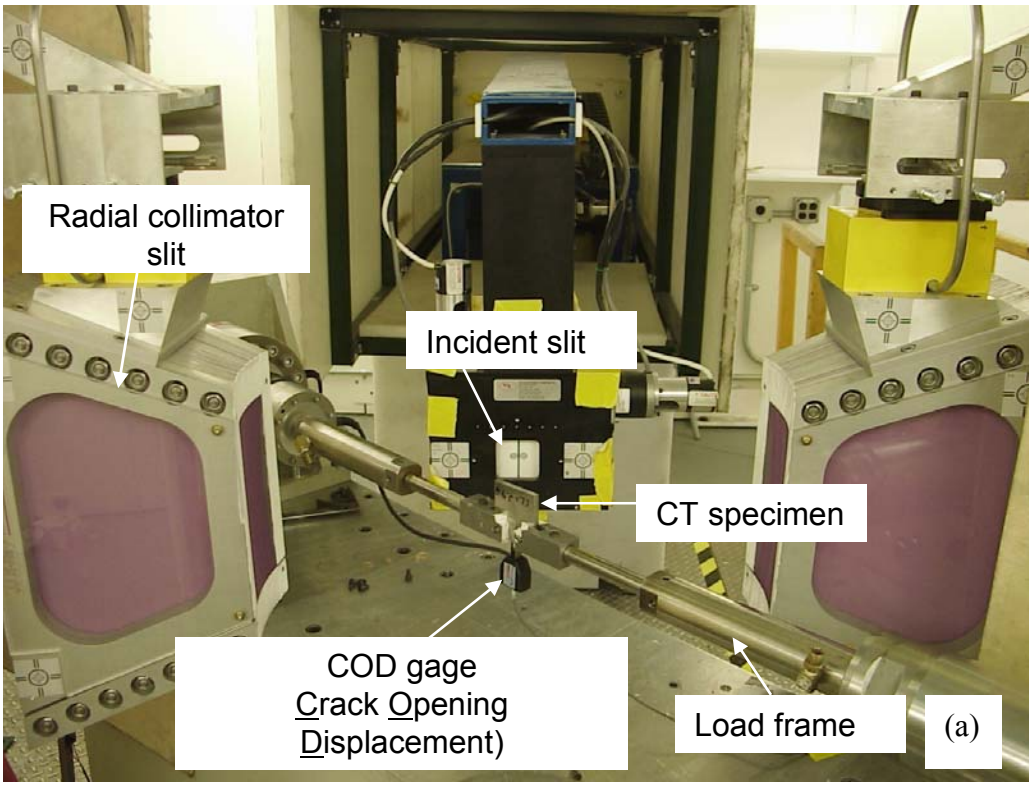

FIGURE 3.15 Fatigue strain measurements using SMARTS instrument (a) picture of the CT specimen mounted in the loading frame in the neutron beam,

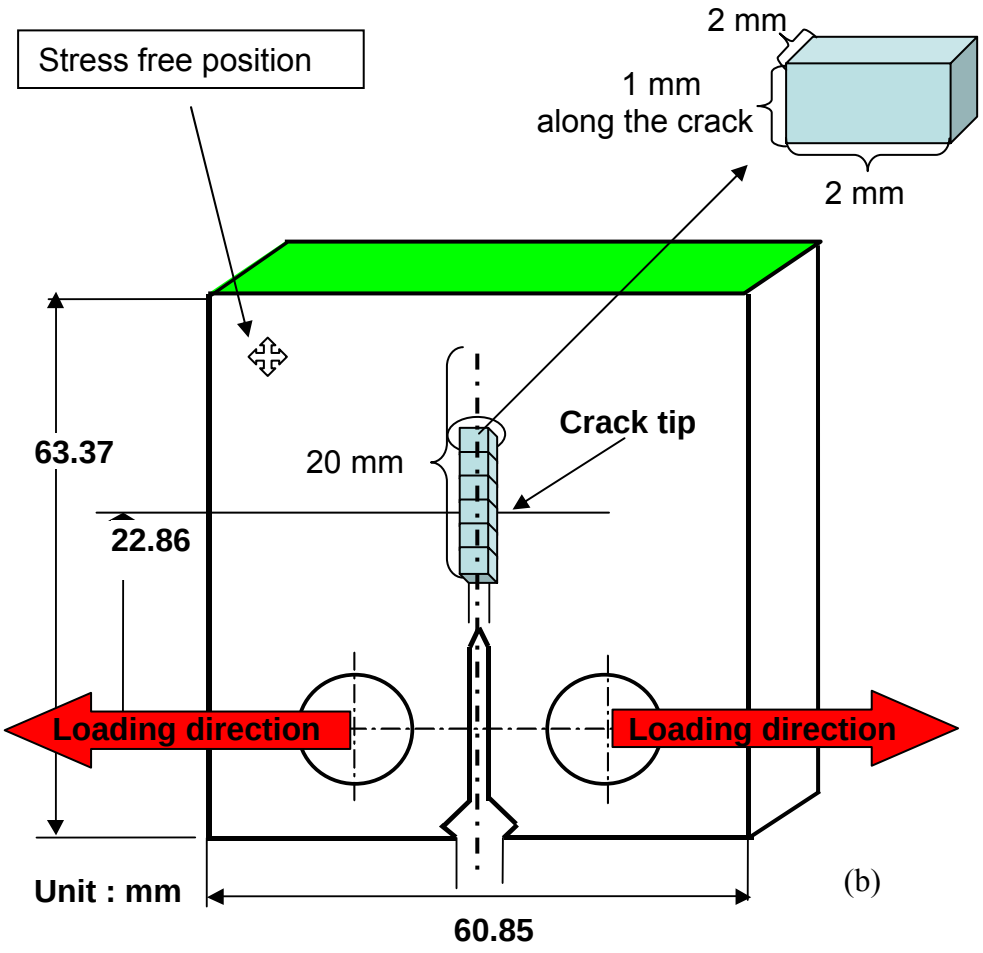

FIGURE 3.15 **Continued** (b) specimen configuration for the spatially-resolved neutron strain measurement with sampling volume: 2 x 1 x 2 mm^3,

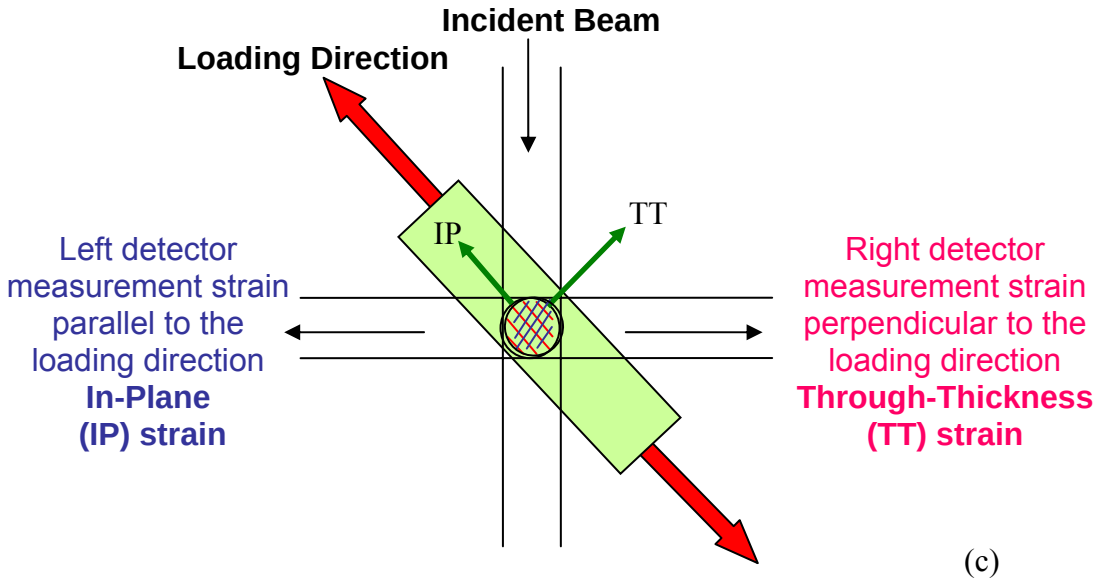

(c)

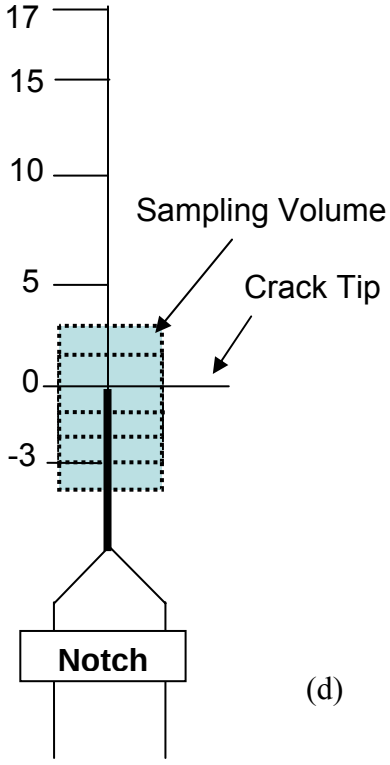

(d)

FIGURE 3.15 **Continued** (c) strain measurement directions: in plane (IP) parallel to the loading direction, through thickness (TT) perpendicular to the loading direction, and (d) neutron strain measurement positions along the crack.

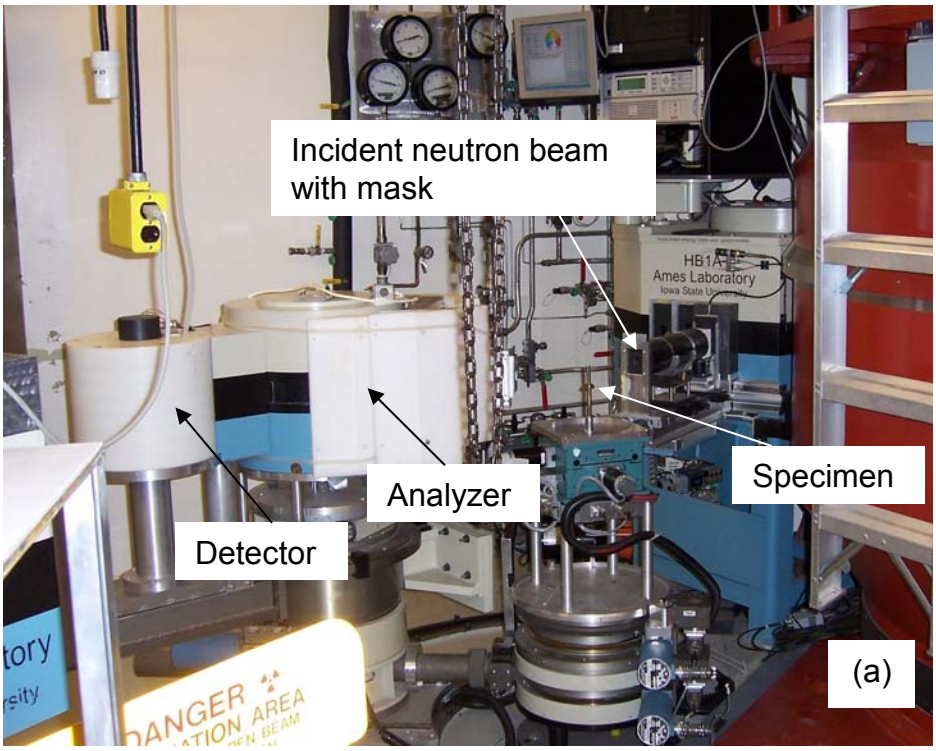

FIGURE 3.16 Quantitative phase study using HB1A instrument (a) picture of the specimen with polypropylene film in the beam and

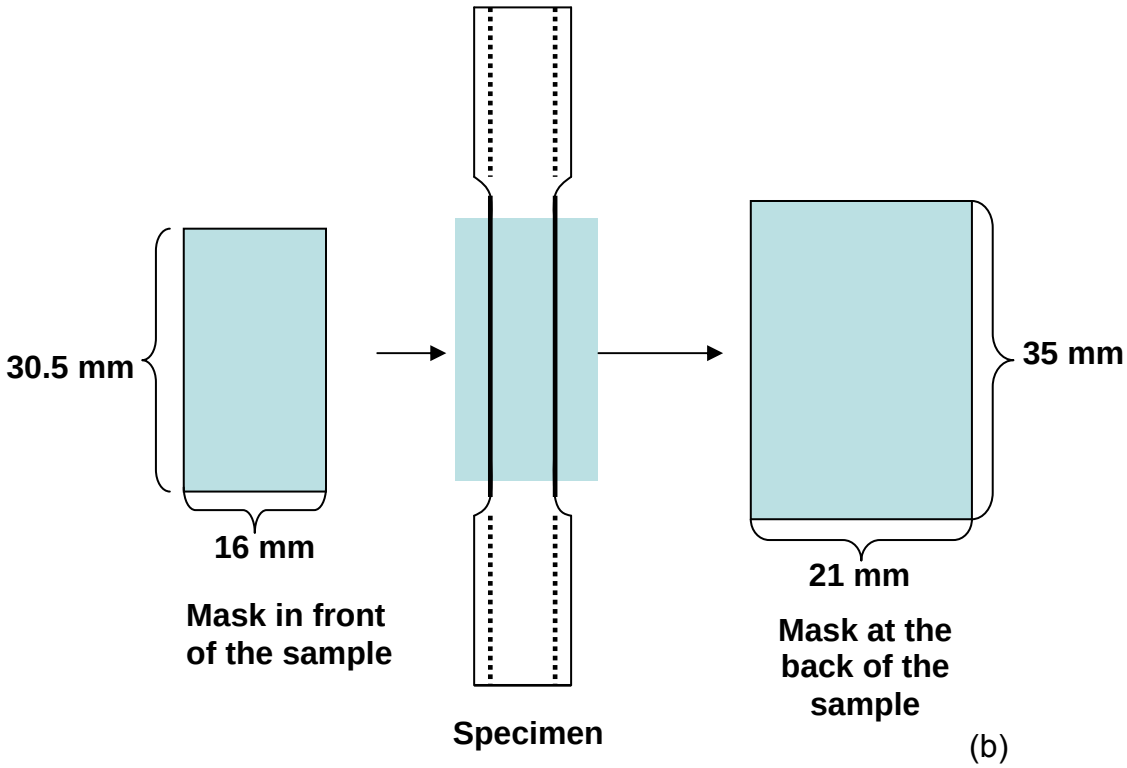

FIGURE 3.16 **Continued** (b) setup of the incoherent neutron scattering measurements.

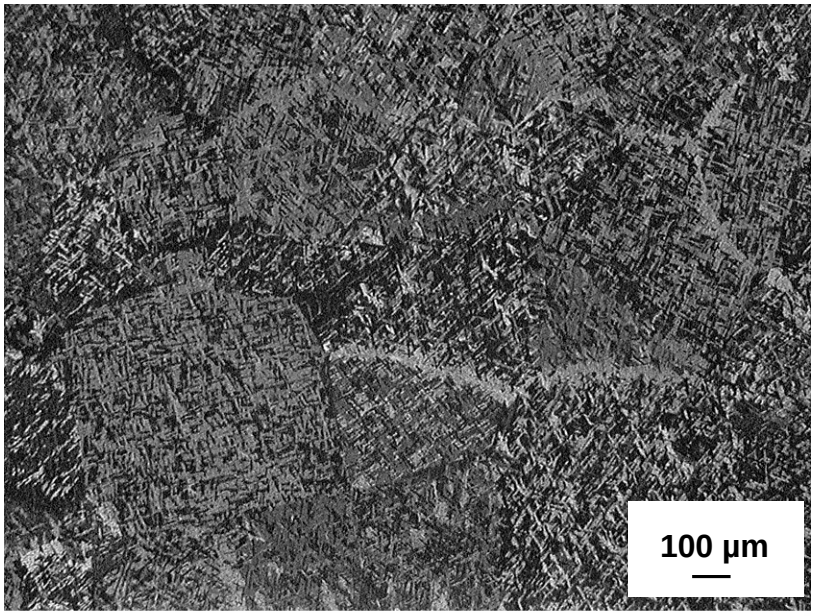

FIGURE 4.1 Microstructure of mechanically polished and etched Zr-4 showing α-Zr grains with a mean diameter of approximately 700 µm. (Micrograph was taken using polarized light optical microscope).

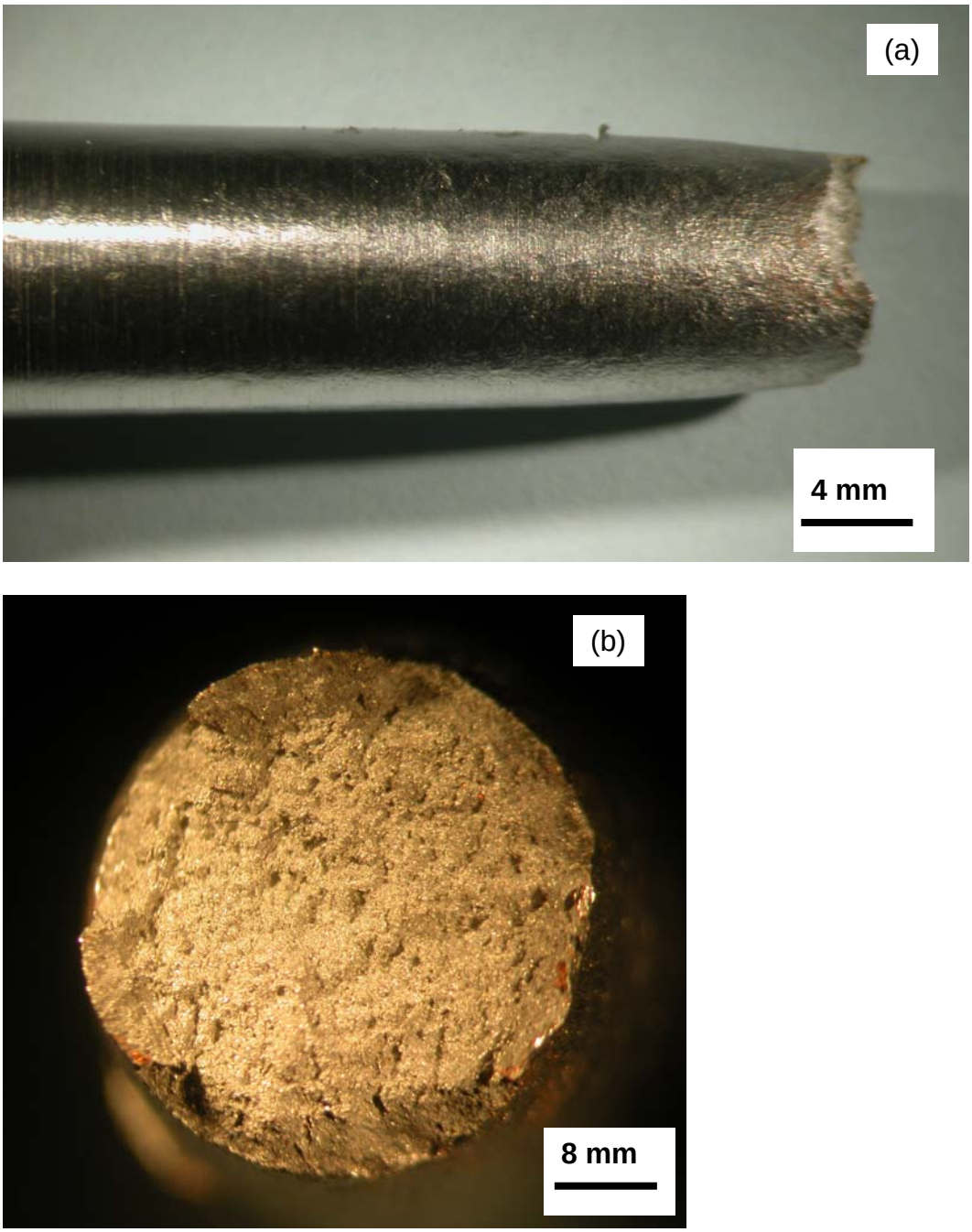

FIGURE 4.2 Optical images of the fracture surface of the round-bar tensile specimen in the as-received condition. A tensile test shows a ductile behavior (a) side view and (b) cross sectional view.

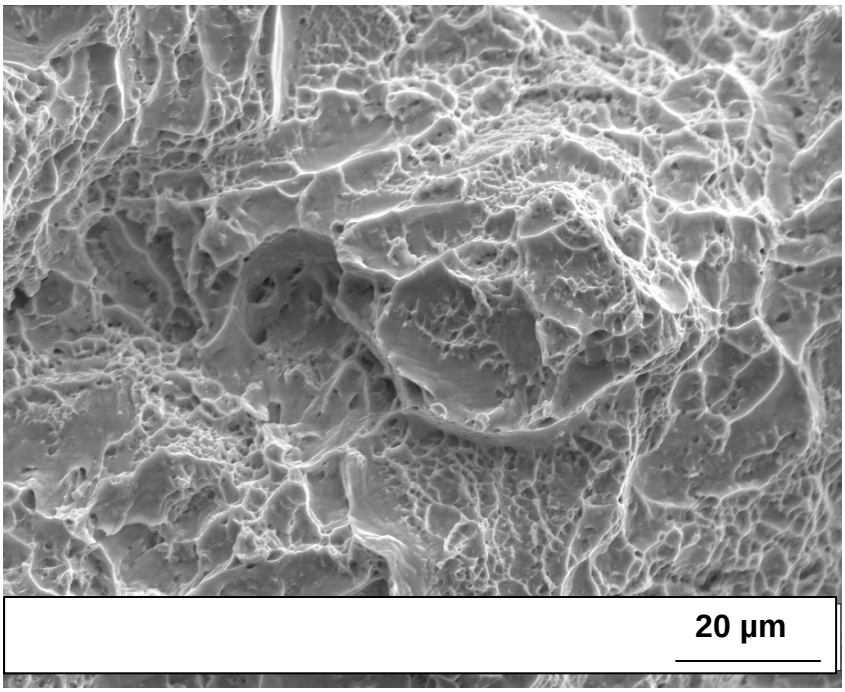

FIGURE 4.3 Fracture surface of an as-received specimen showing a typical ductile fracture with dimples associated with ductile metallic ligaments.

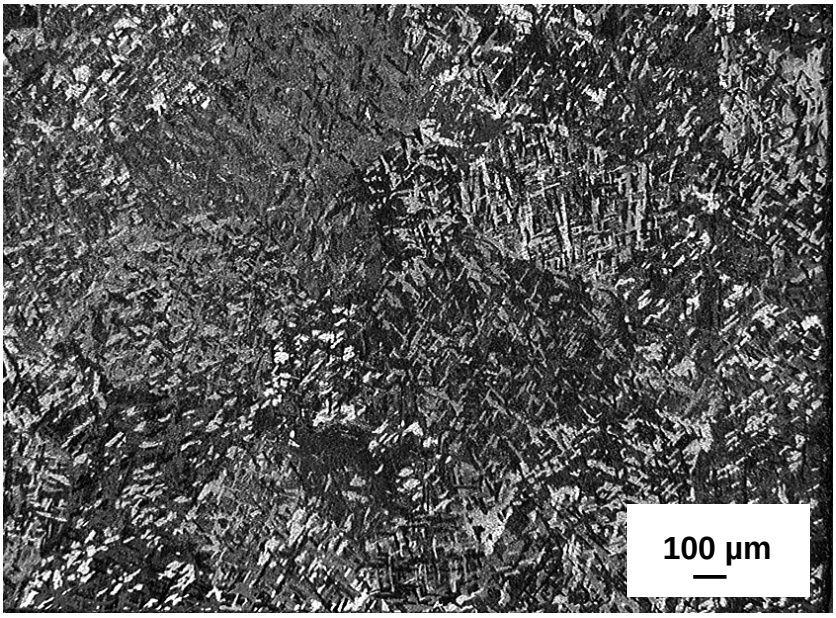

FIGURE 4.4 Optical micrograph of the mechanically polished and etched cross section of the CT specimen charged electrochemically with hydrogen, showing the same trend for areas (1) and (2), in Figure 3.9.

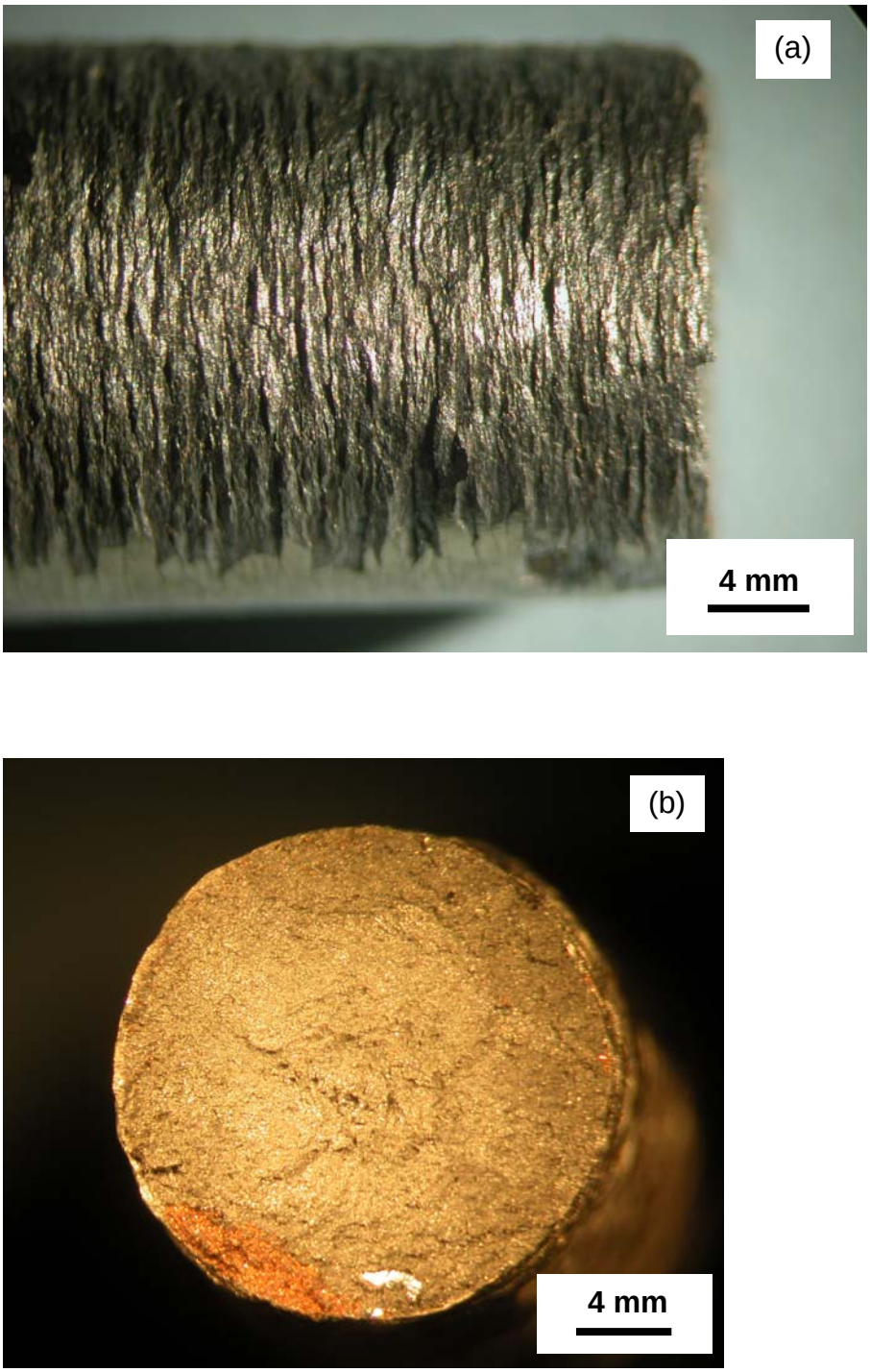

FIGURE 4.5 Optical images of the fracture surface of the round bar tensile specimen charged with hydrogen for 30 minutes. It shows a brittle behavior. (a) Side view, hydride layer cleaved by the end of a tensile test and (b) cross sectional view.

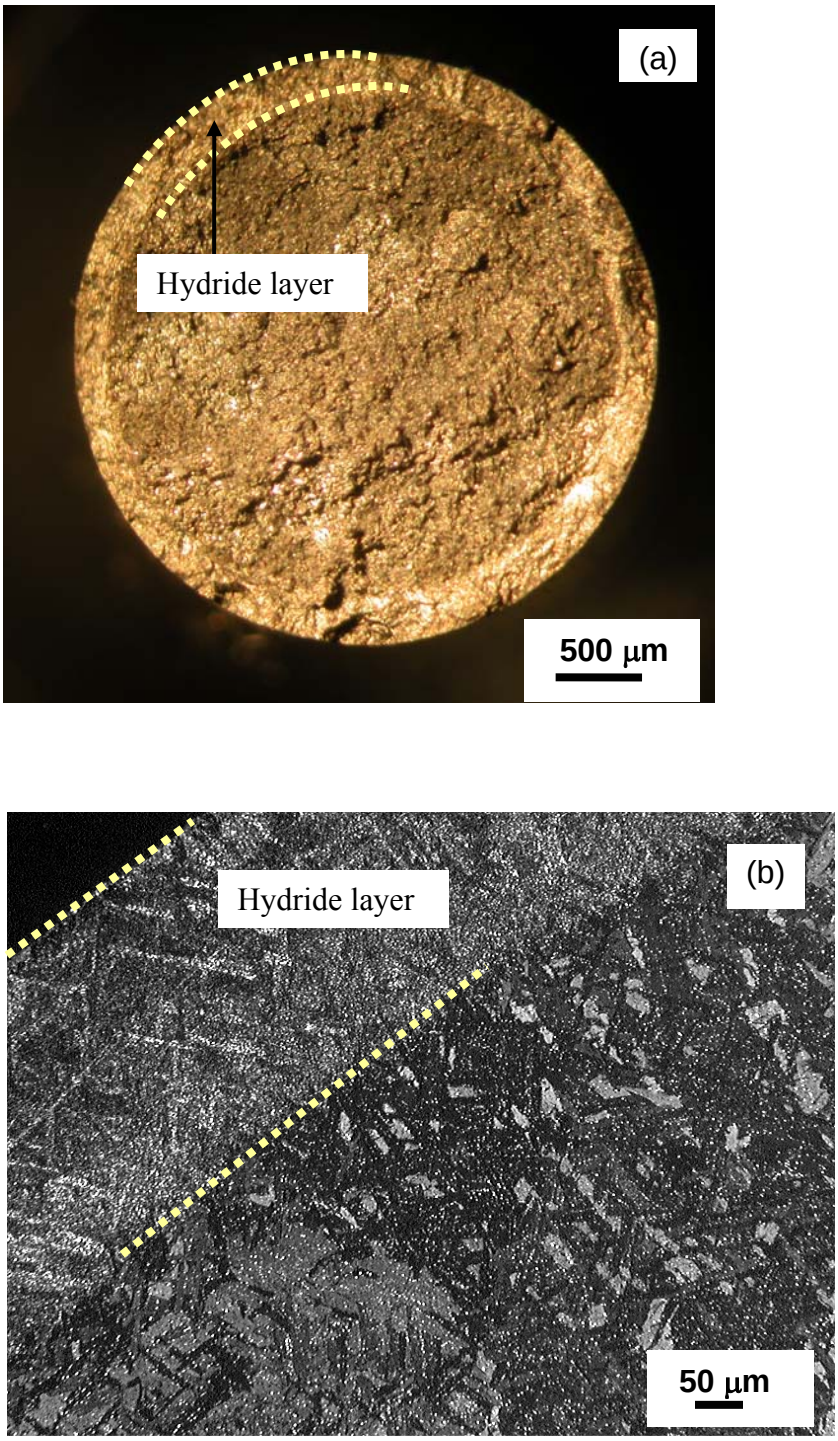

FIGURE 4.6 Optical images of a specimen charged with hydrogen gas for 1 hour (a) Fracture surface shows a hydride layer with a thickness of 400 μm in a ring shape near the surface of the specimen, (b) Optical micrograph of a polished and etched cross section, and

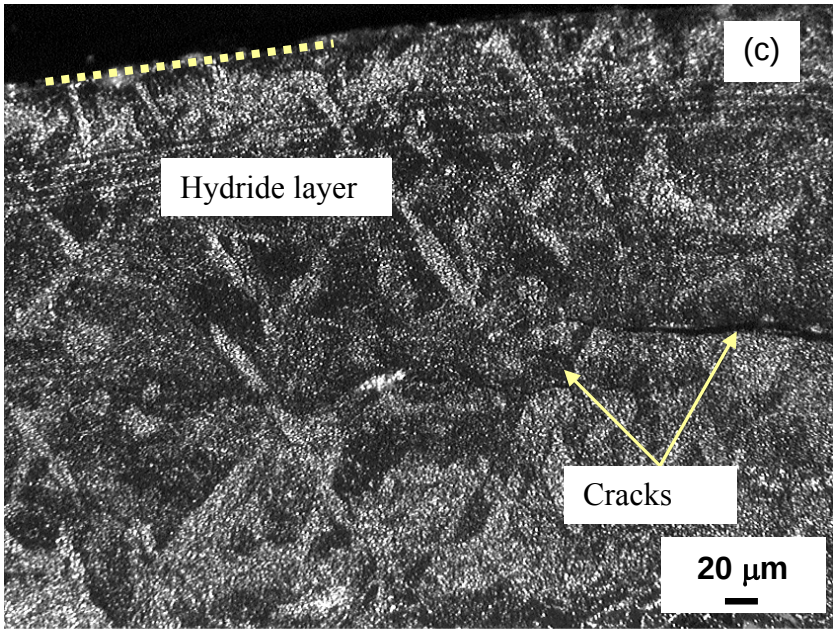

FIGURE 4.6 **Continued** (c) Magnified image of (b) showing the cracks. Dotted lines represent the outer edge of the hydride layer.

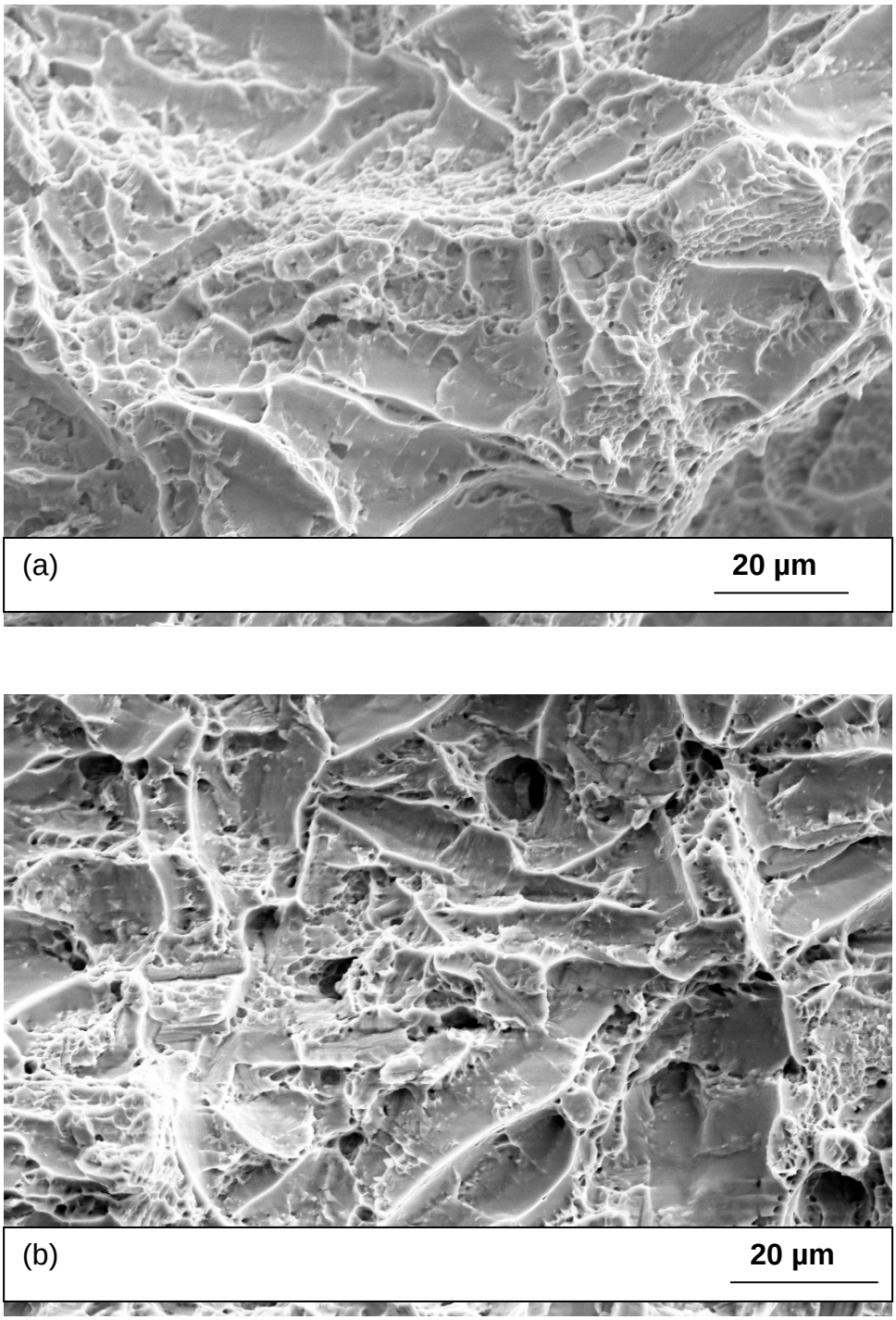

FIGURE 4.7 Fracture surfaces of the specimen charged with hydrogen for one hour. The specimen shows (a) ductile fracture around its center (area 1 in Figure 3.10), (b) mixed brittle and ductile regions between its center and edge (area 2 in Figure 3.10), and

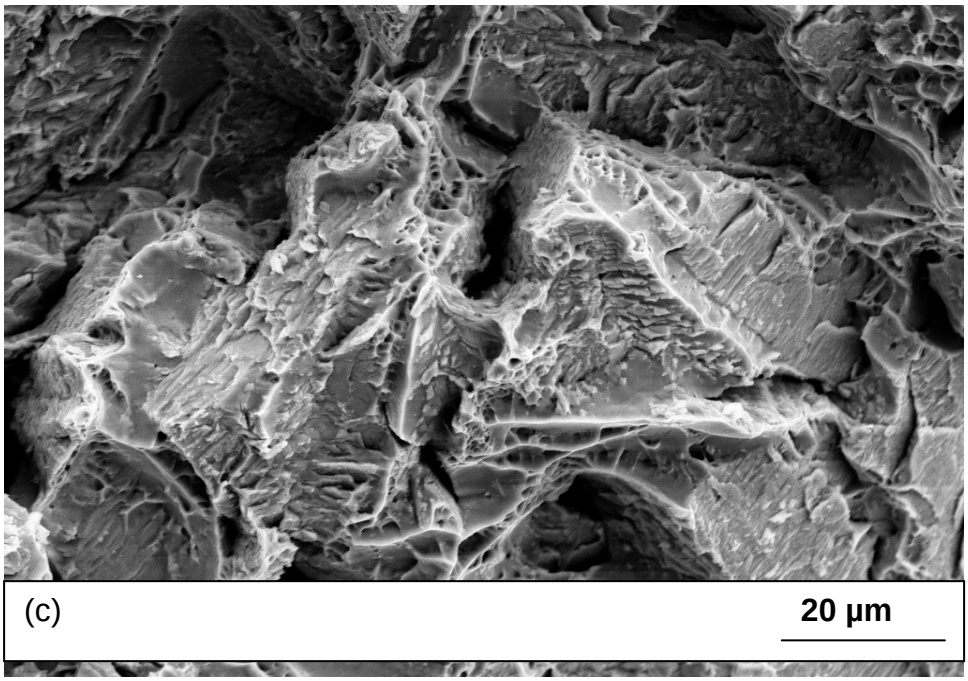

FIGURE 4.7 **Continued** (c) mostly brittle fracture regions near the surface edge of the specimen. (area 3 in Figure 3.10).

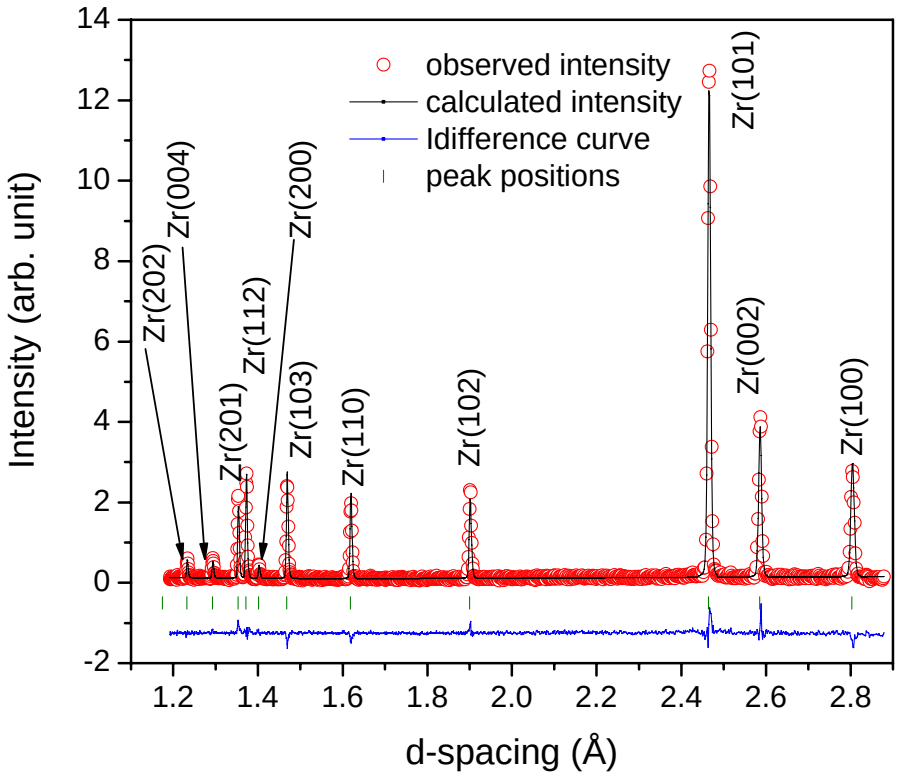

FIGURE 4.8 A typical neutron-diffraction pattern of an as-received Zr-4 alloy, showing α –Zr phase. This pattern was obtained at 1 mm distance from the surface using the ENGIN-X instrument. Red circles are the observed data and the continuous line is the theoretical data.

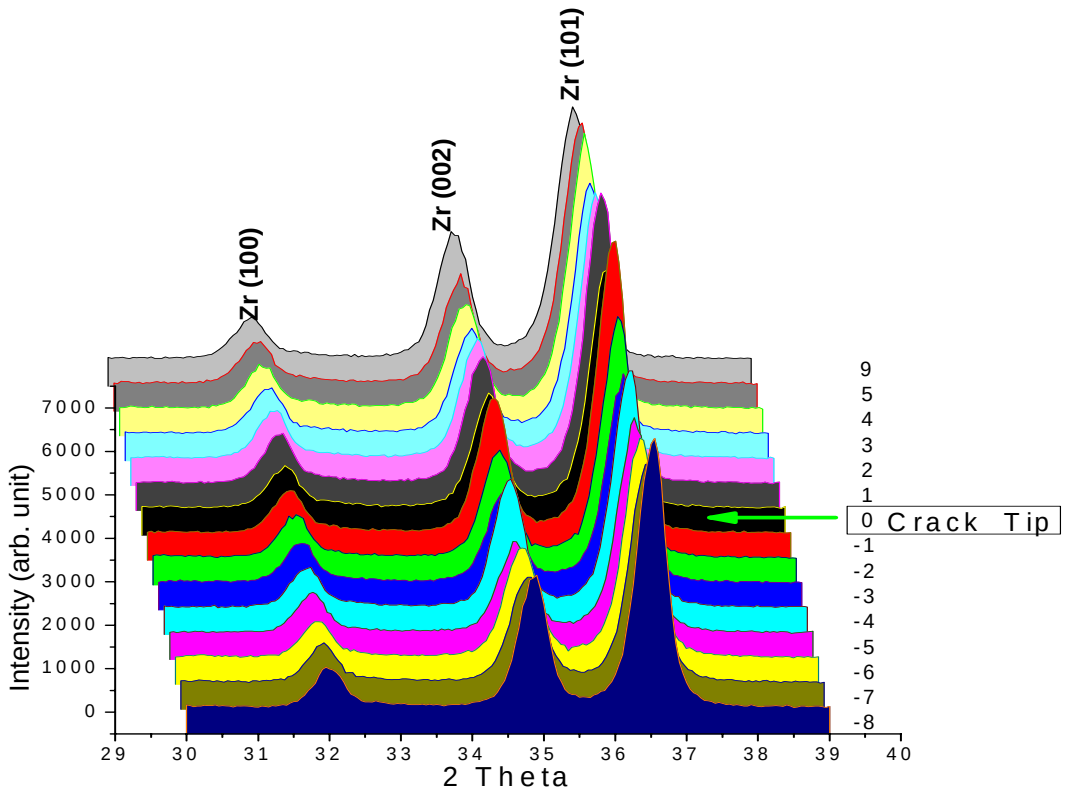

FIGURE 4.9 X-ray diffraction patterns obtained from the CT specimen in the as-received condition at different measurement points, using a rotating anode x-ray diffractometer. Arrow stands for the position of the crack tip.

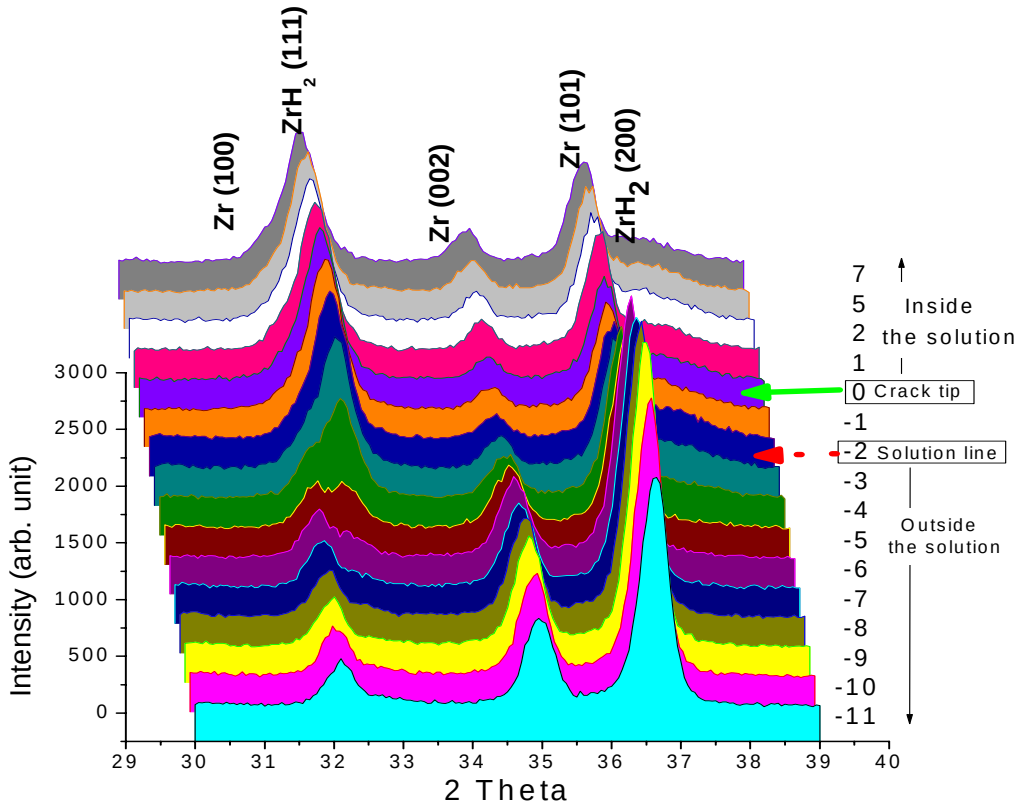

FIGURE 4.10 X-ray diffraction patterns obtained from the CT specimen electrochemically charged with hydrogen at different measurement points, using a rotating anode x-ray diffractometer. Red dotted arrow stands for the level of the charging solution, which is at 2 mm behind the crack tip (the green arrow).

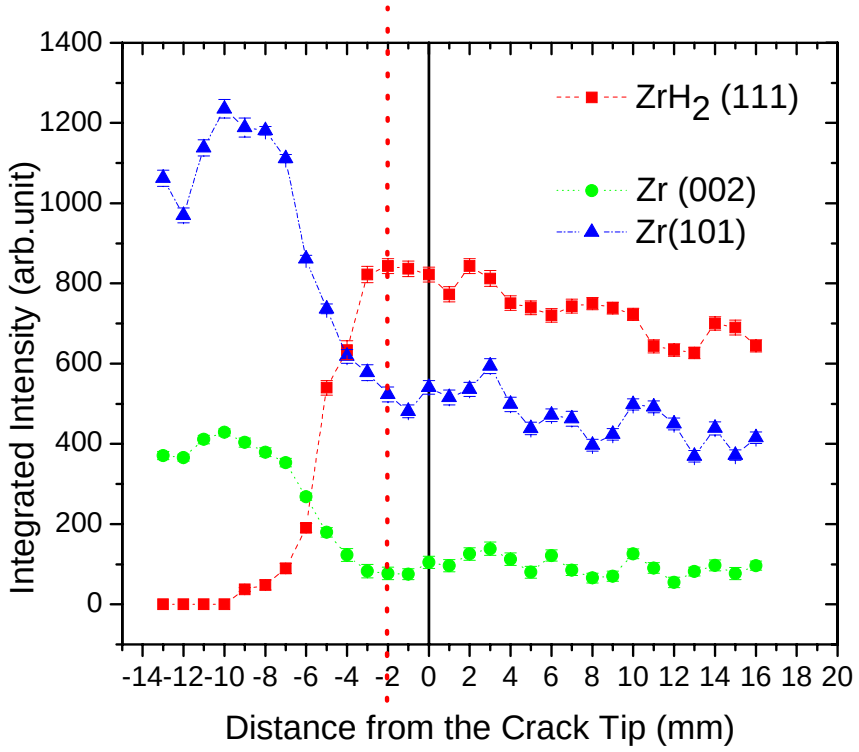

FIGURE 4.11 Variations of the peaks intensities for [● Zr (002), ▲ Zr (101), and ■ ZrH_2 (111)] as a function of the position relative to the charging solution line and crack tip. Red dotted line represents the charging solution line and black continuous line is for the crack tip position.

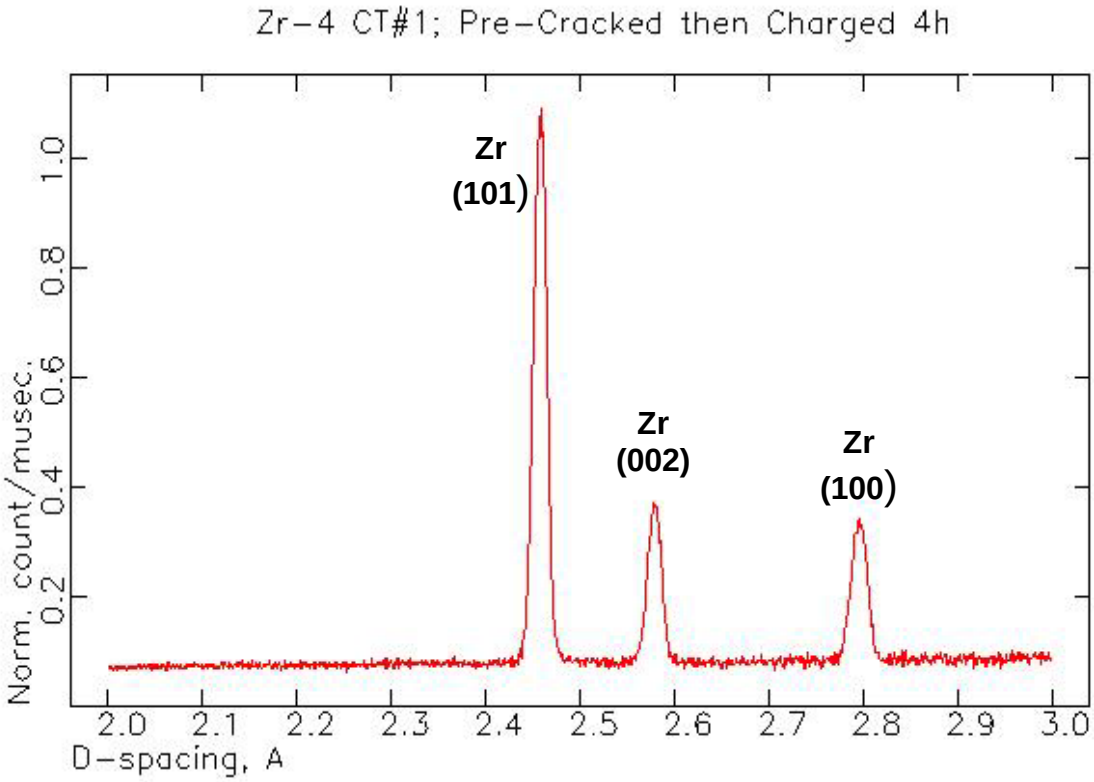

FIGURE 4.12 Example of a neutron-diffraction pattern taken using the SMARTS instrument from the middle of the thickness of CT specimen charged electrochemically with hydrogen.

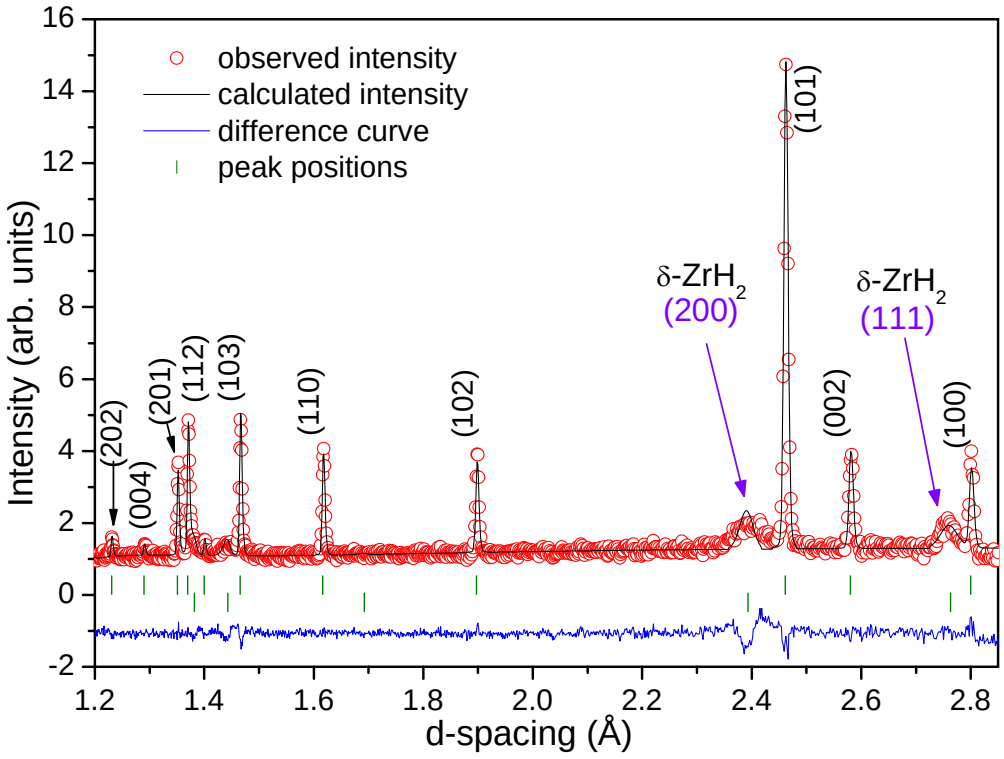

FIGURE 4.13 Example of a neutron-diffraction pattern for the sample charged with hydrogen gas for 1 hour showing two phases: hcp zirconium and face-centered-cubic (delta) δ-ZrH_2. The diffraction pattern was obtained at 1 mm from the surface of the specimen using the ENGIN-X instrument. Red circles are the measured data and the black continuous line is the fitted data.

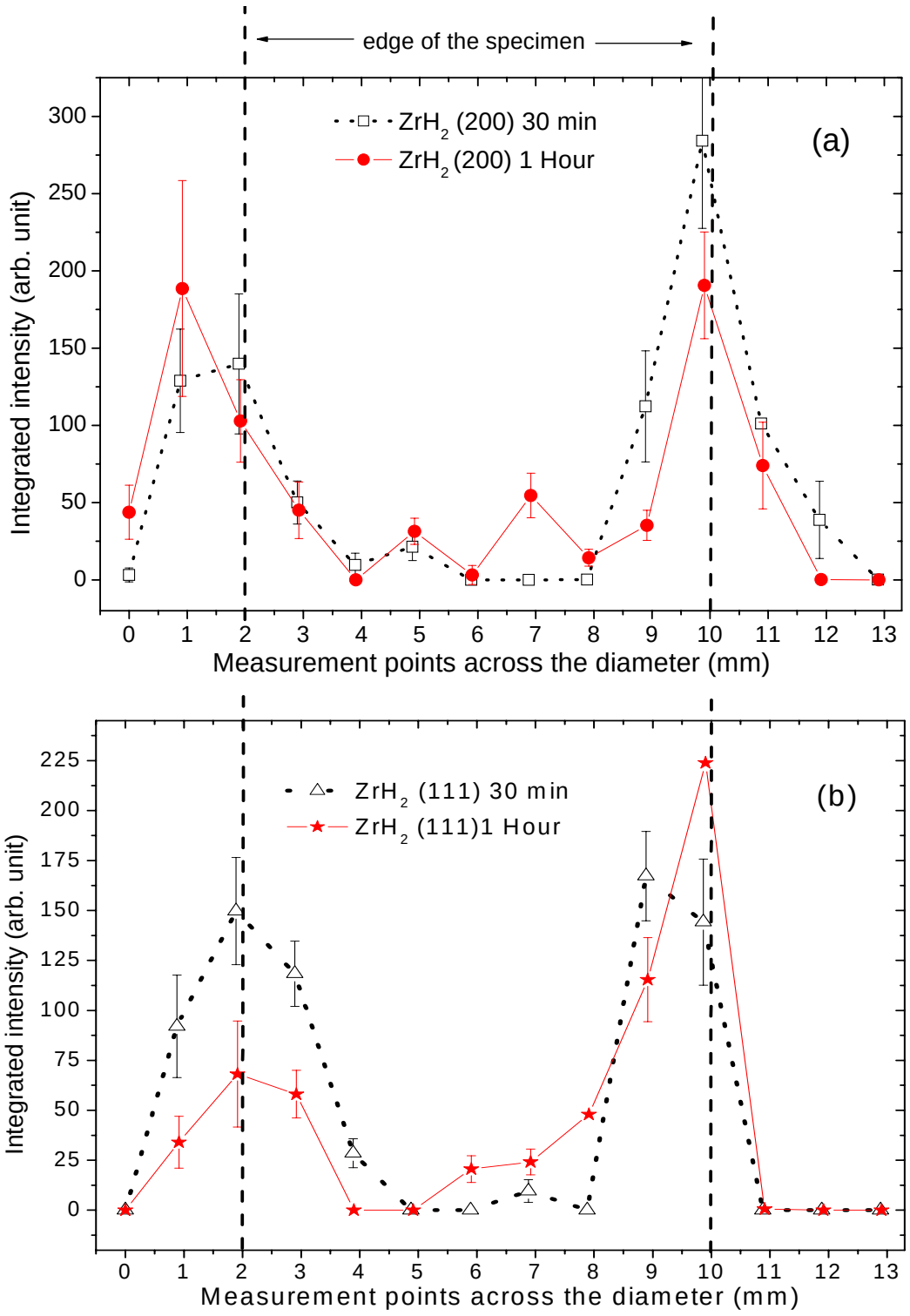

FIGURE 4.14 Variation of the peak intensities across the diameter of the gas-hydrogenated specimens (a) δ-ZrH_2 (200) (□ 30 minutes, ● 1 hour) and (b) δ-ZrH_2 (111) (△ 30 minutes, ☆ 1 hour).

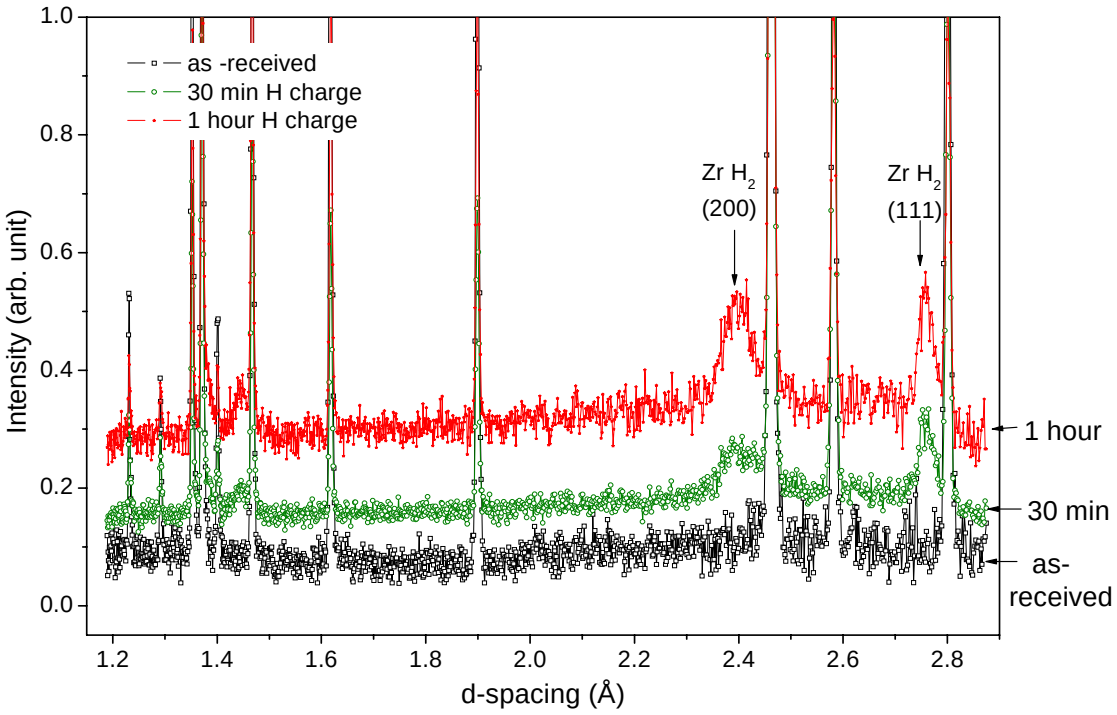

FIGURE 4.15 Comparison of three diffraction patterns, corresponding to the as-received and hydrogenated specimens, showing increases in the background due to the hydrogen incoherent scattering.

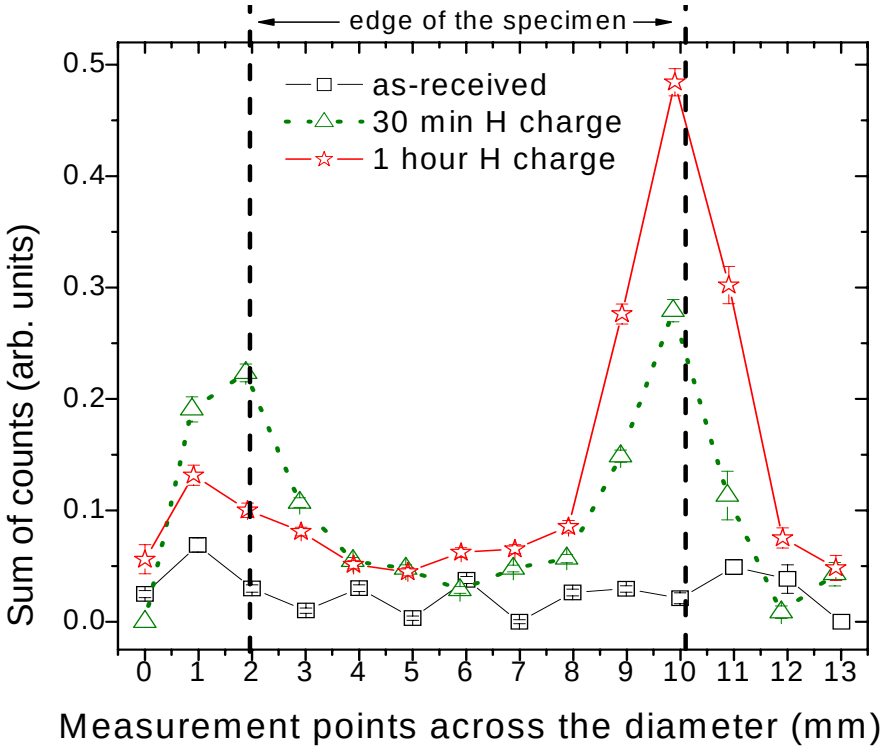

FIGURE 4.16 Variation of the background intensity across the diameter for all three specimens (□ as-received, △ 30 minutes, ☆ 1 hour).

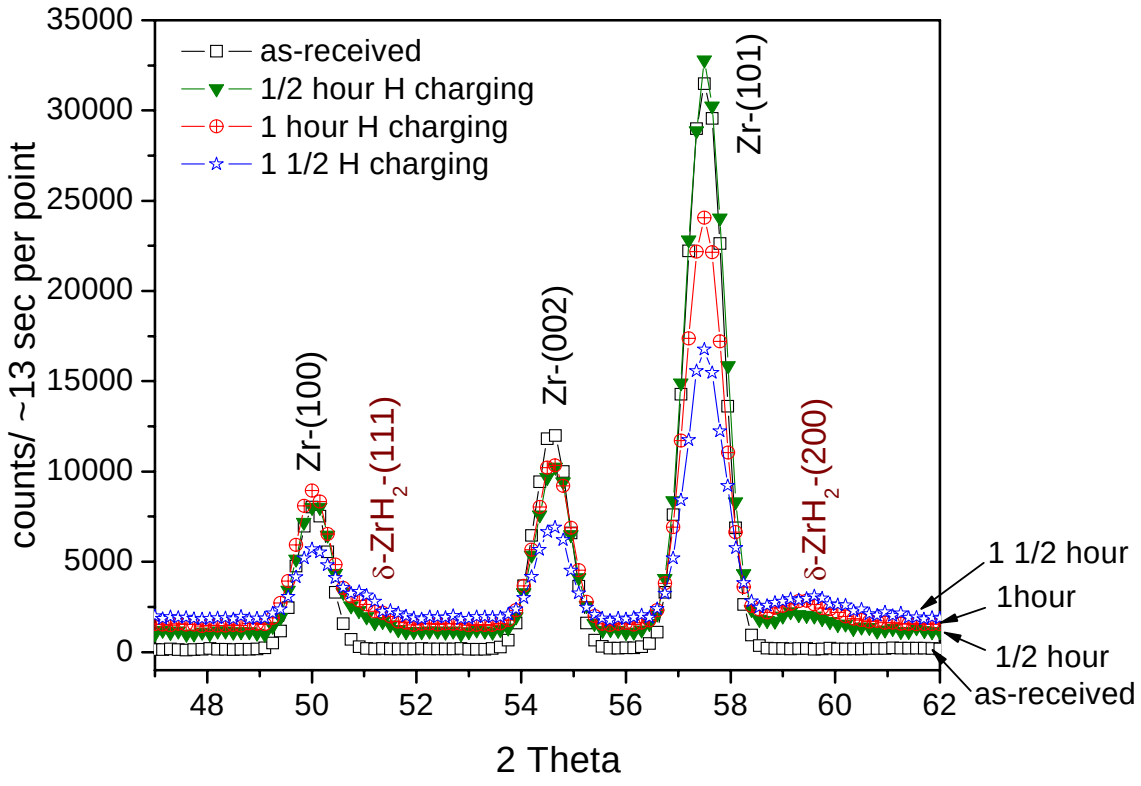

FIGURE 4.17 Diffraction measurements at the HB1A instrument for several Zr-4 specimens charged with hydrogen for different charging times (□ as-received specimen, ▼ ½ hour hydrogen charging, ⊕ 1 hour hydrogen charging, ☆ 1 ½ hour hydrogen charging).

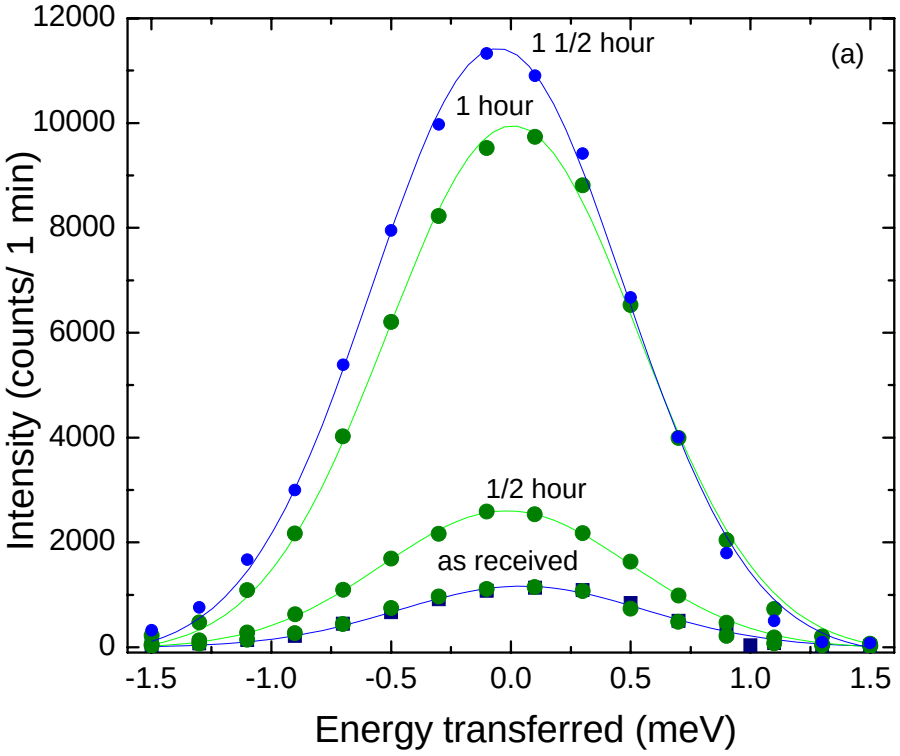

FIGURE 4.18 Energy scans around the zero-energy transfer showing the increase of the incoherent scattering with the increase in the hydrogen content in (a) the hydrogen-charged Zr-4 specimens and

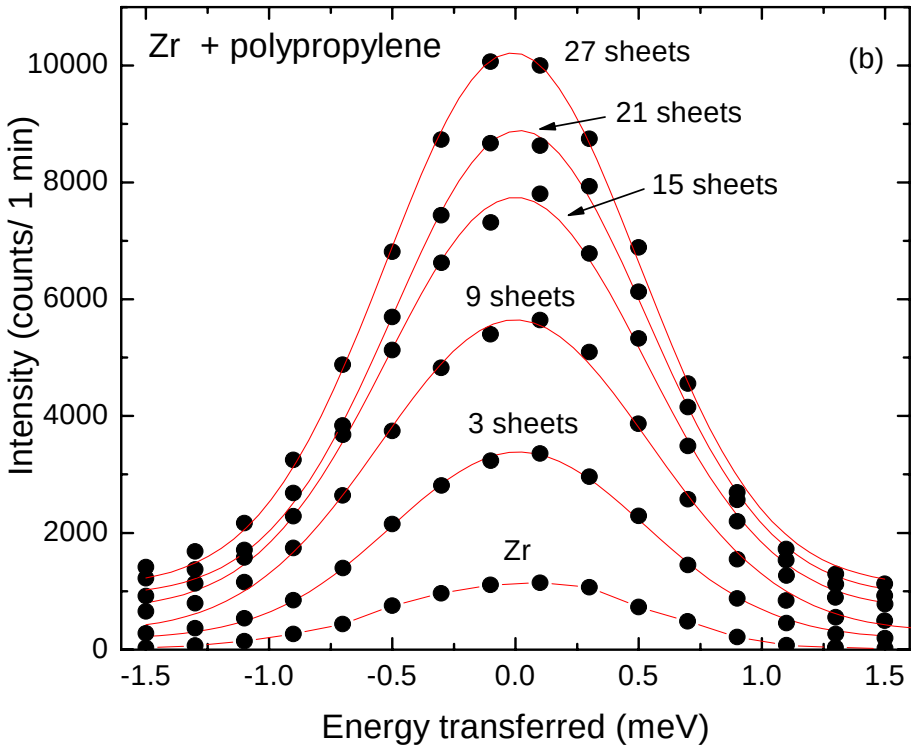

FIGURE 4.18 **Continued** (b) standard samples with polypropylene sheets. (Black dots are the experimental data and the continuous lines are the fitting to the measured data).

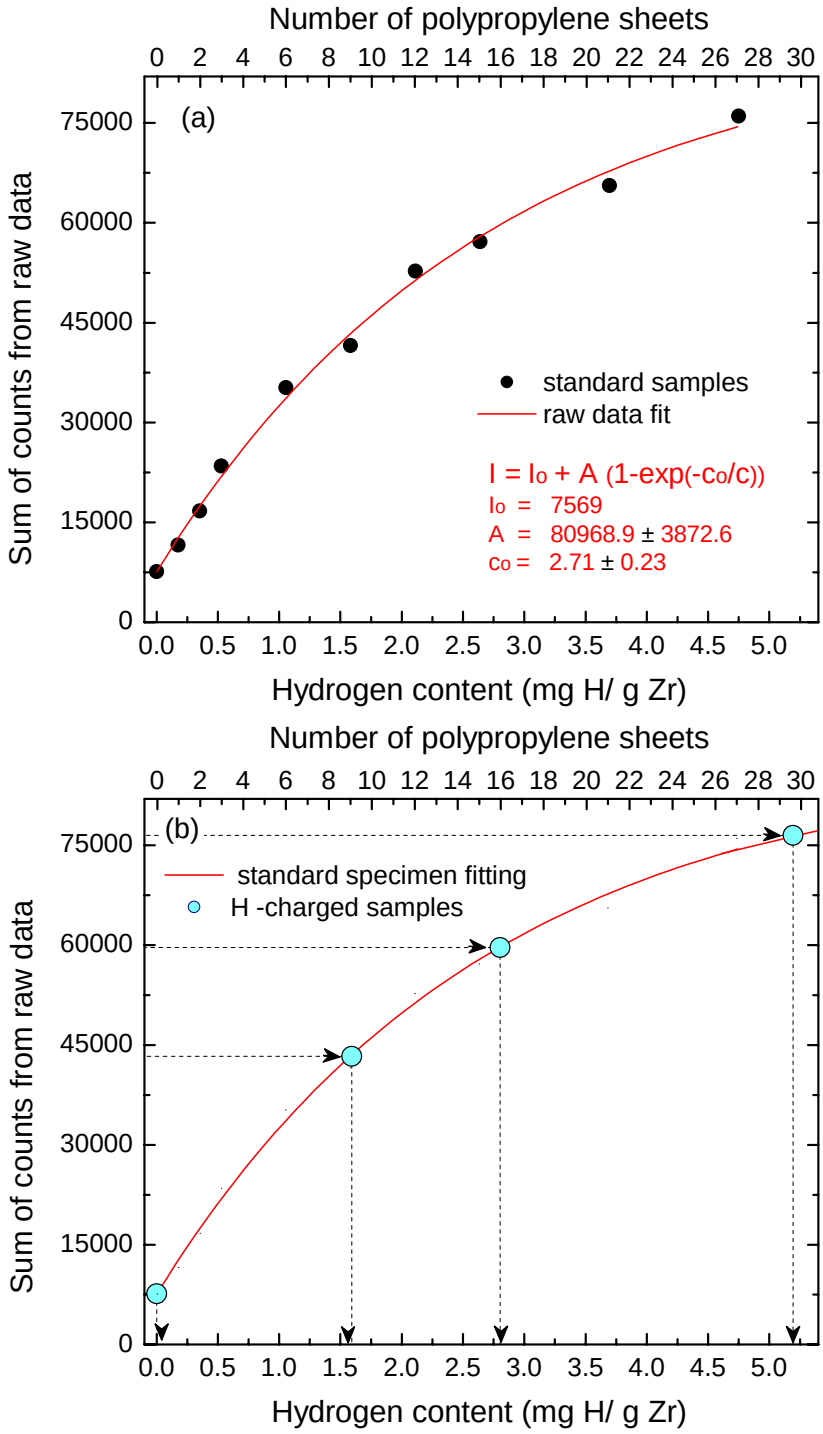

FIGURE 4.19 Neutron incoherent scattering (NIS) as a function of the hydrogen content. (a) NIS measured for the standard specimens and the fit (red line) of the experimental data using the equation from the inset and (b) NIS obtained for the hydrogen-charged samples by interpolation using the equation from the inset of (a).

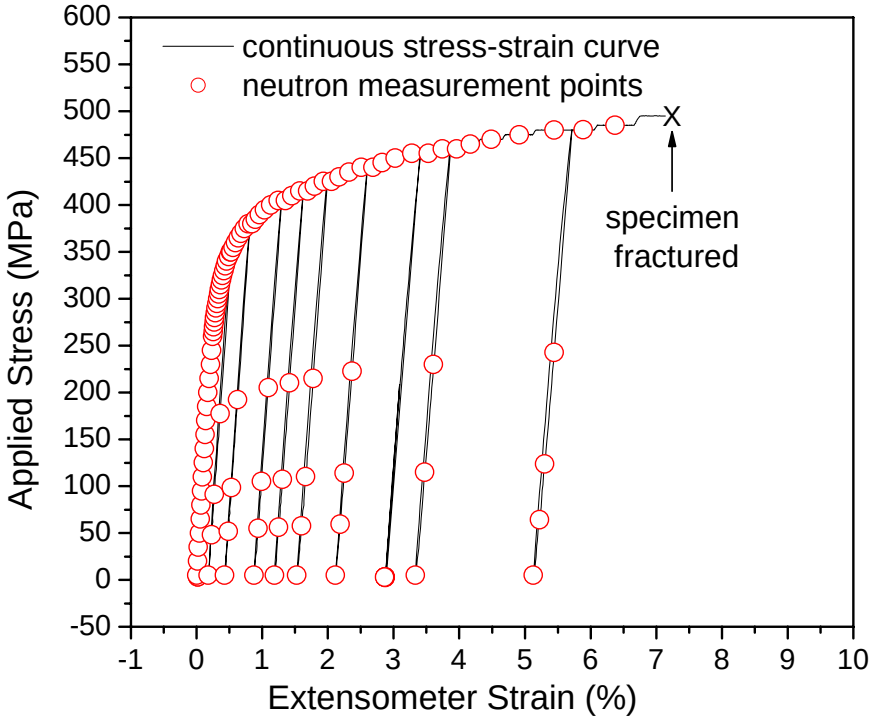

FIGURE 4.20 Macroscopic stress-strain curve of Zr-4 in the as-received condition. The strain was measured, using an extensometer attached to the specimen (continuous black line) using the ENGIN-X instrument. Neutron-diffraction measurement points are represented by red circles.

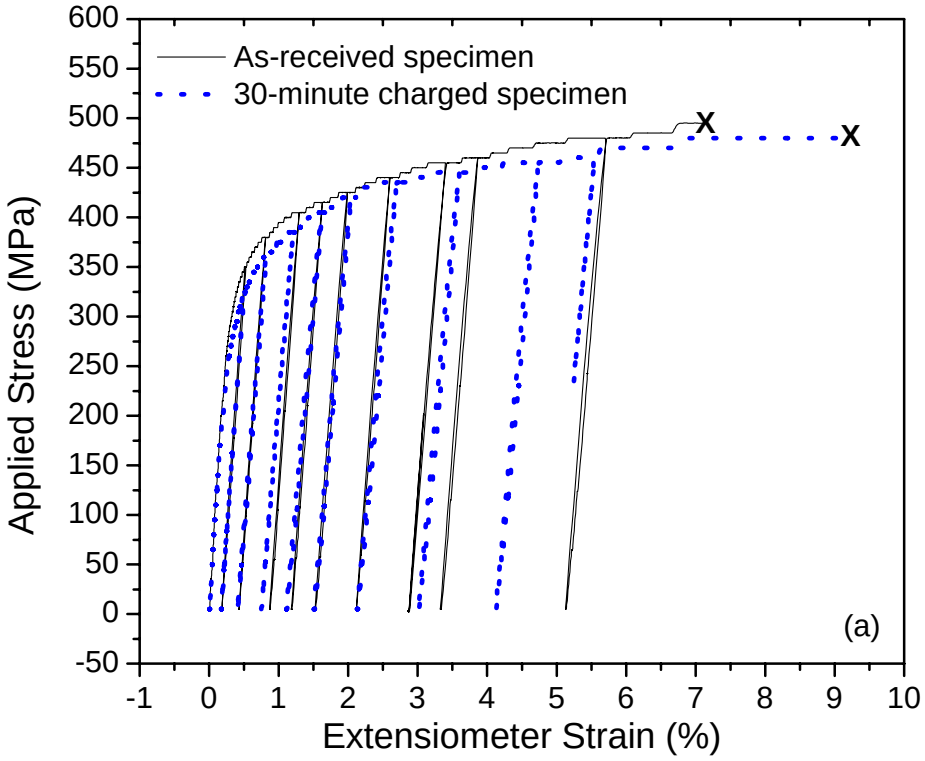

FIGURE 4.21 Macroscopic stress-strain curves of Zr-4 (a) comparison between as-received specimen (continuous black line) and a specimen charged with hydrogen gas for 30 minutes (about 1,600 ppm hydrogen, dotted blue line). The strain was measured using an extensometer attached to the specimen and

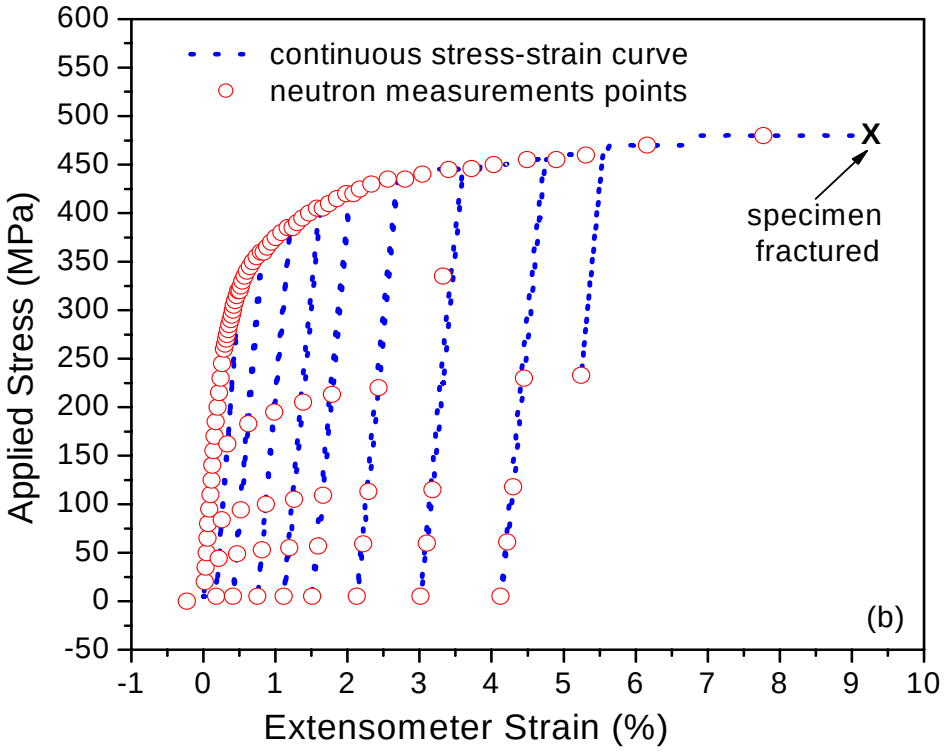

FIGURE 4.21 **Continued** (b) specimen with 1,600 ppm hydrogen showing the, extensometer strain (blue dotted line) and neutron-diffraction measurement points collected using the ENGIN-X instrument (red circles).

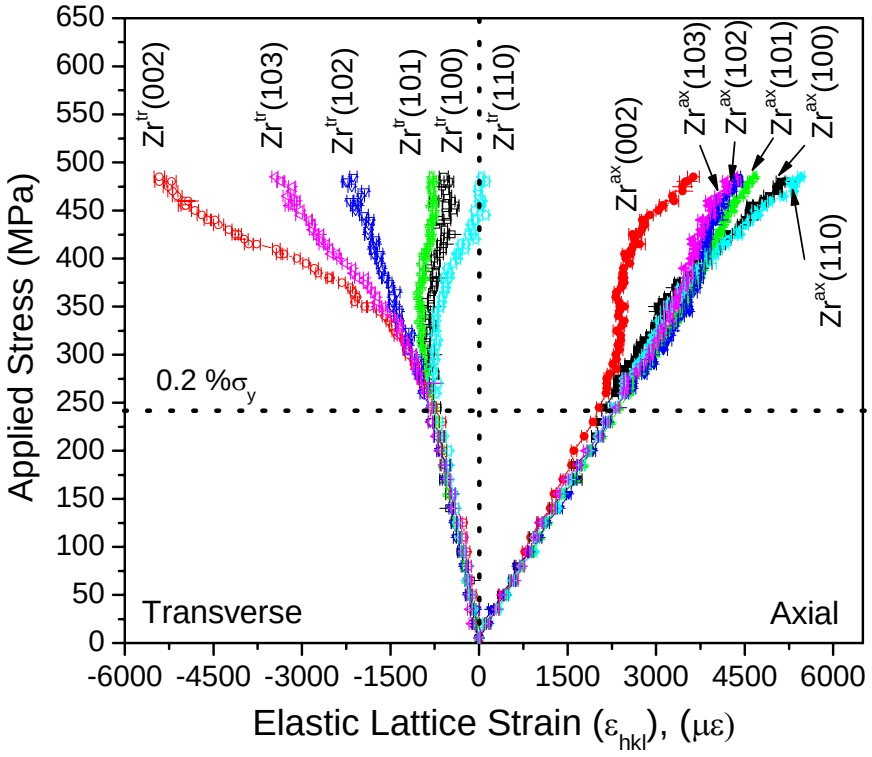

FIGURE 4.22 Elastic-plastic anisotropy on axial and transverse directions for the specimen in the as-received condition.

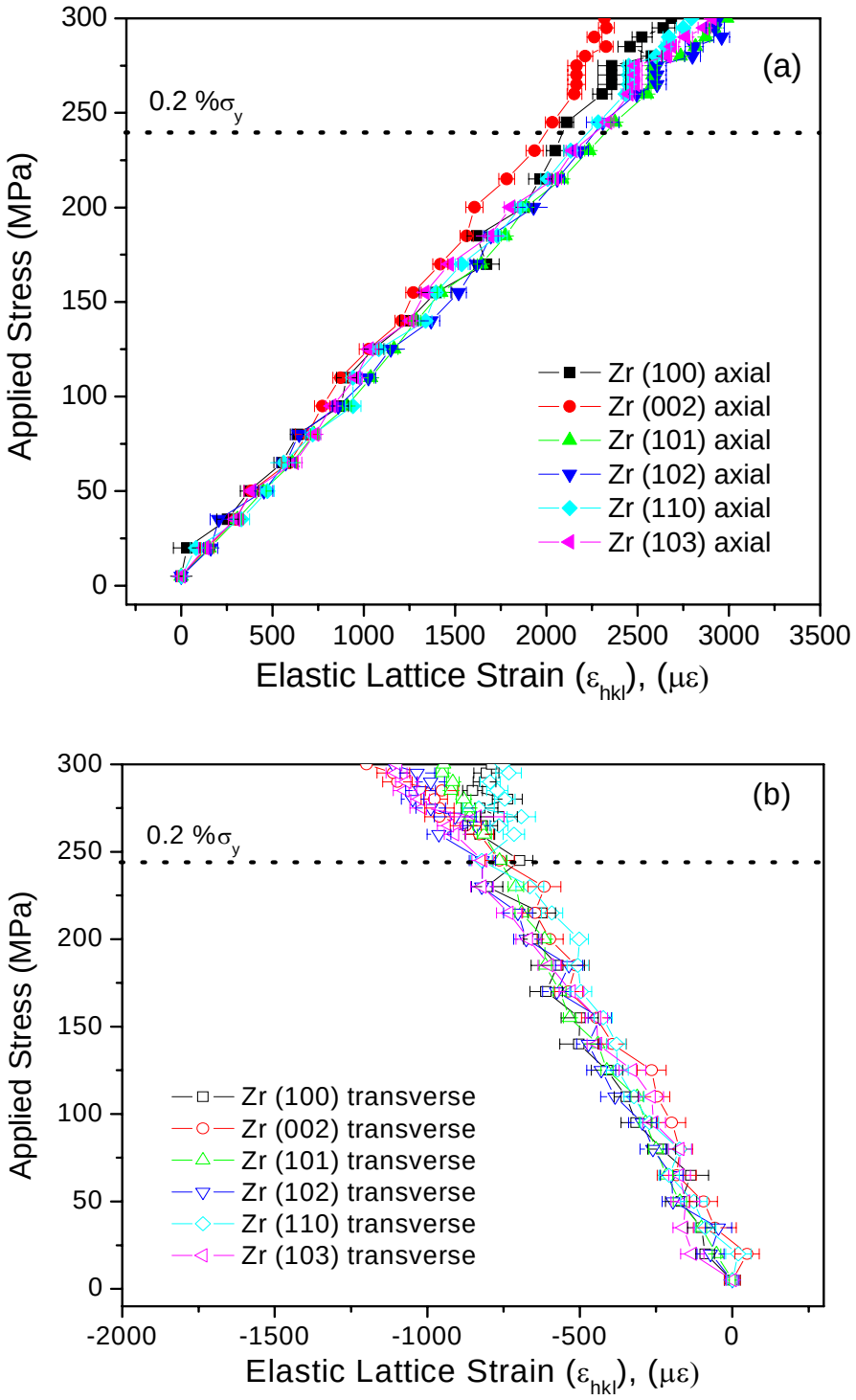

FIGURE 4.23 Elastic anisotropy for the specimen in the as-received condition, (a) axial and (b) transverse directions.

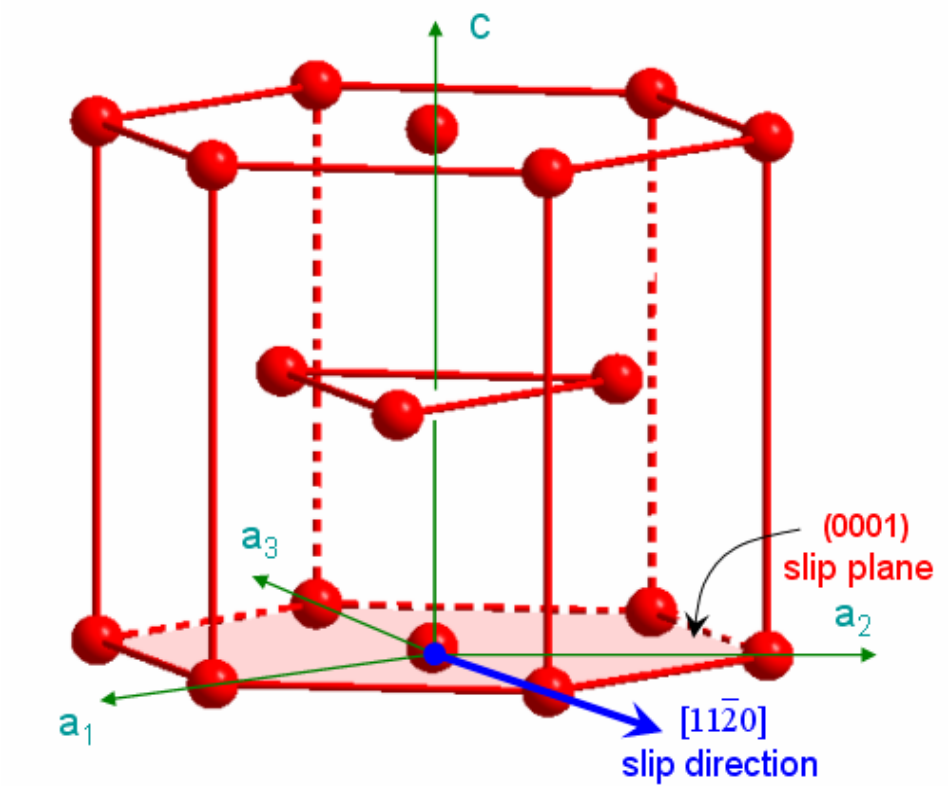

FIGURE 4.24 Slip System for hcp Zr-4.

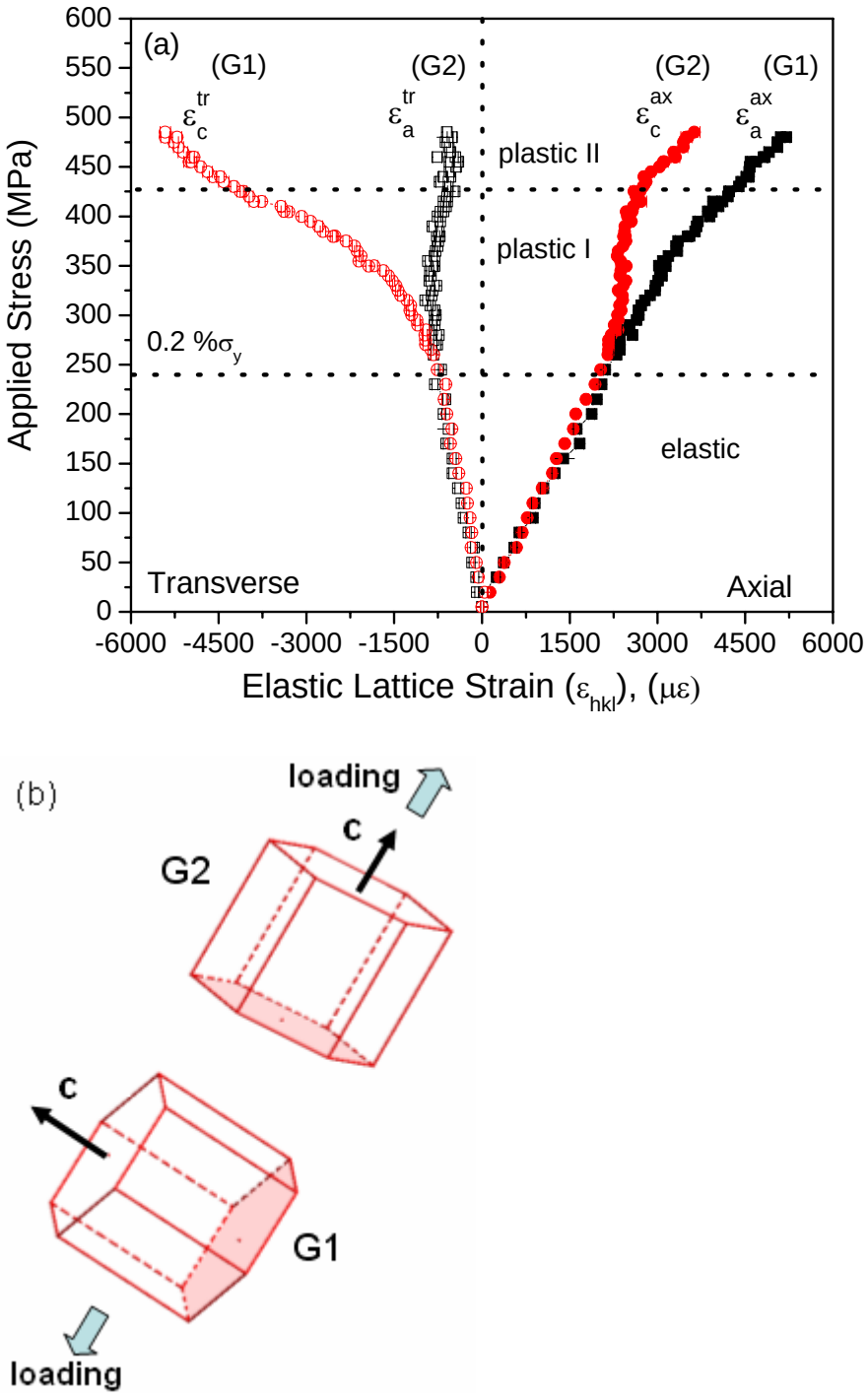

FIGURE 4.25 The elastic lattice strains in Zr-4 in the as-received condition as a function of the applied stress (a) the *a*- and *c*-axes strains are shown for the axial and transverse directions (■ ε_a^{ax}, ● ε_c^{ax}, □ ε_a^{tr}, and ○ ε_c^{tr}) and (b) perspective view of the two different grains set G1 and G2 (black arrow is the c-axis and the wide blue arrow is the loading direction).

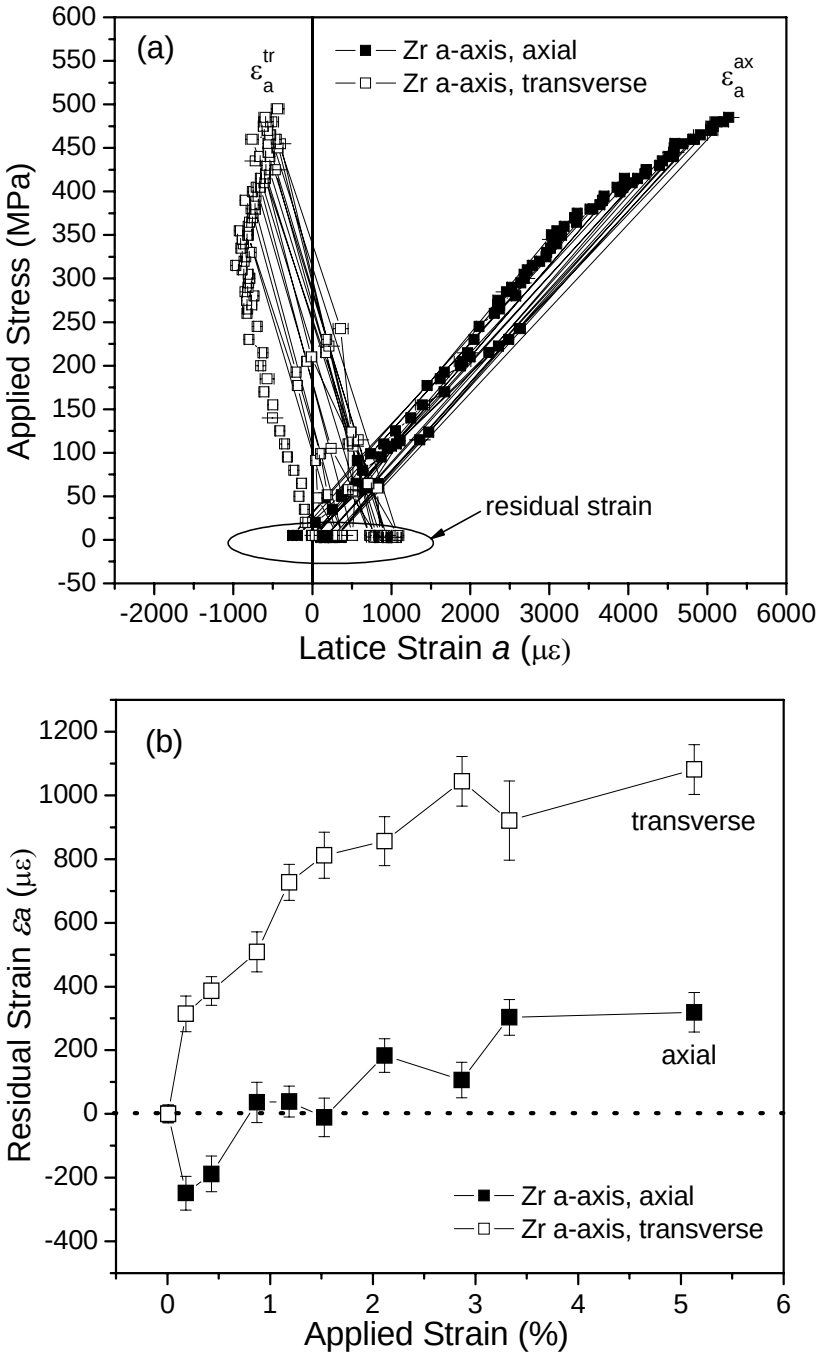

FIGURE 4.26 Residual lattice strain, ε_a, as a function of the plastic strain in axial and transverse directions for the specimen in the as-received condition. (a) in-situ loading and unloading lattice strain evolution. Circled data are residual strains obtained from unloads to a stress of 5 MPa and (b) development of the residual lattice strains at the unloads (■ ε_a^{ax} and □ ε_a^{tr}).

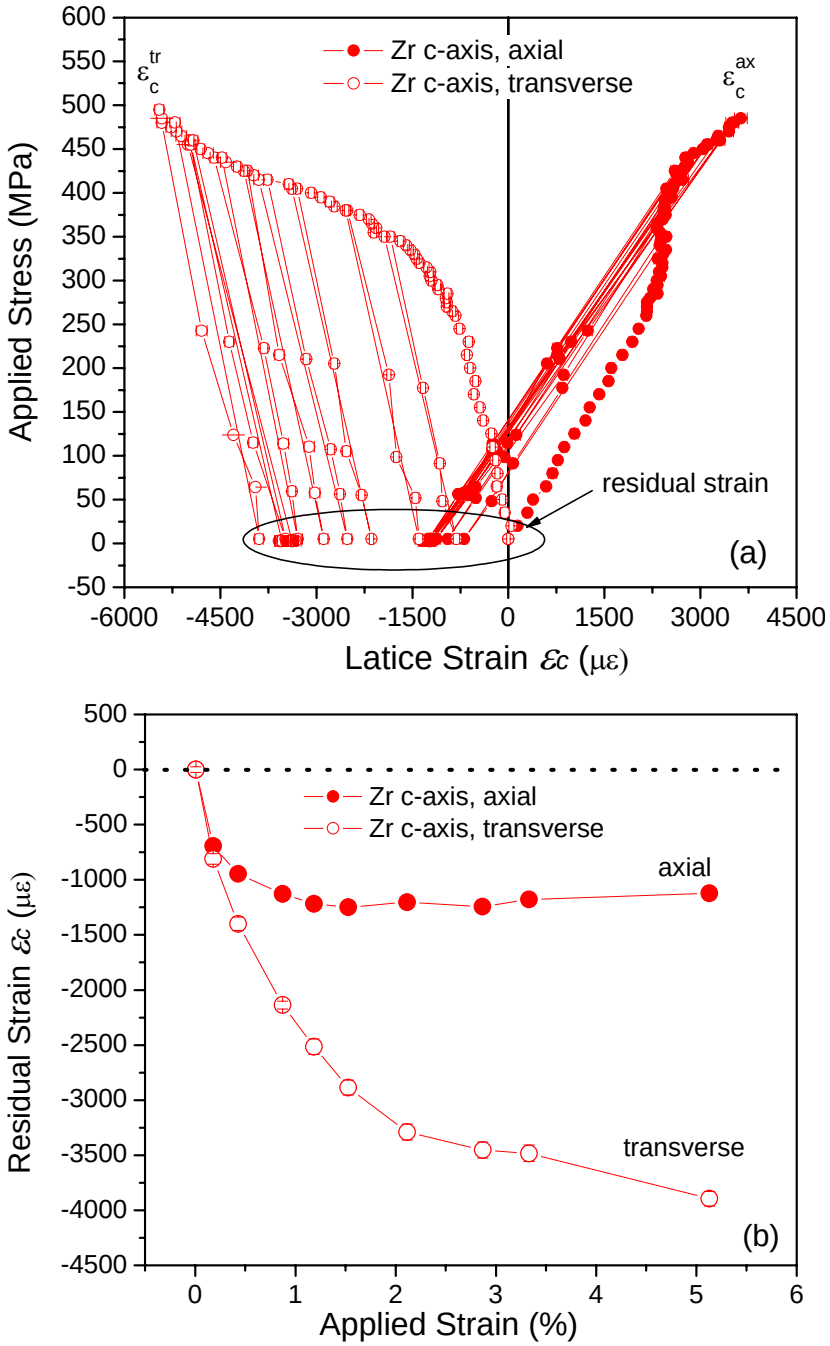

FIGURE 4.27 Residual lattice strain, ε_c, as a function of the plastic strain in axial and transverse directions for the specimen in the as-received condition. (a) in-situ loading and unloading lattice strain evolution. Circled data are residual strains obtained from unloads to a stress of 5 MPa and (b) development of the residual lattice strains at the unloads (● ε_c^{ax} and ○ ε_c^{tr}).

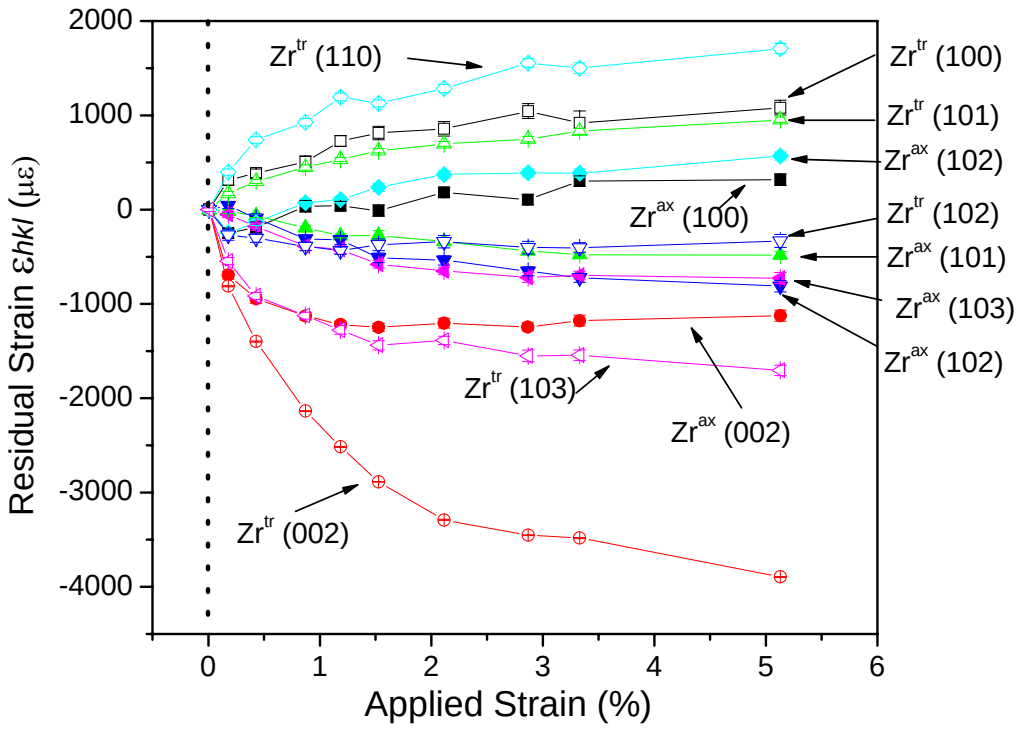

FIGURE 4.28 Residual lattice strains as a function of the plastic strain in axial and transverse directions for six different Zr reflections in the as-received specimen.

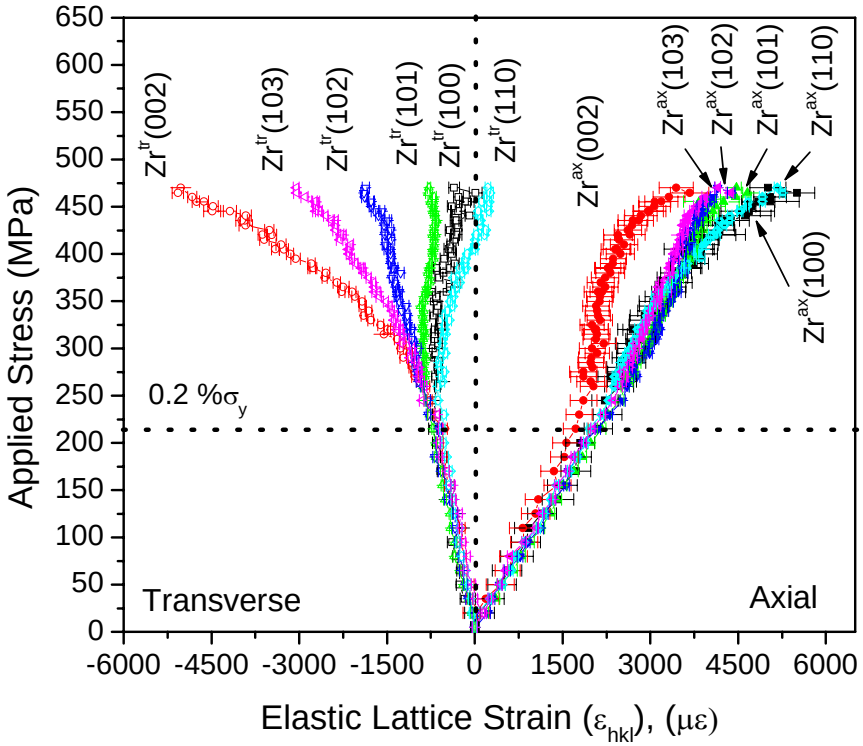

FIGURE 4.29 Elastic-plastic anisotropy in the specimen with approximately 1,600 ppm hydrogen.

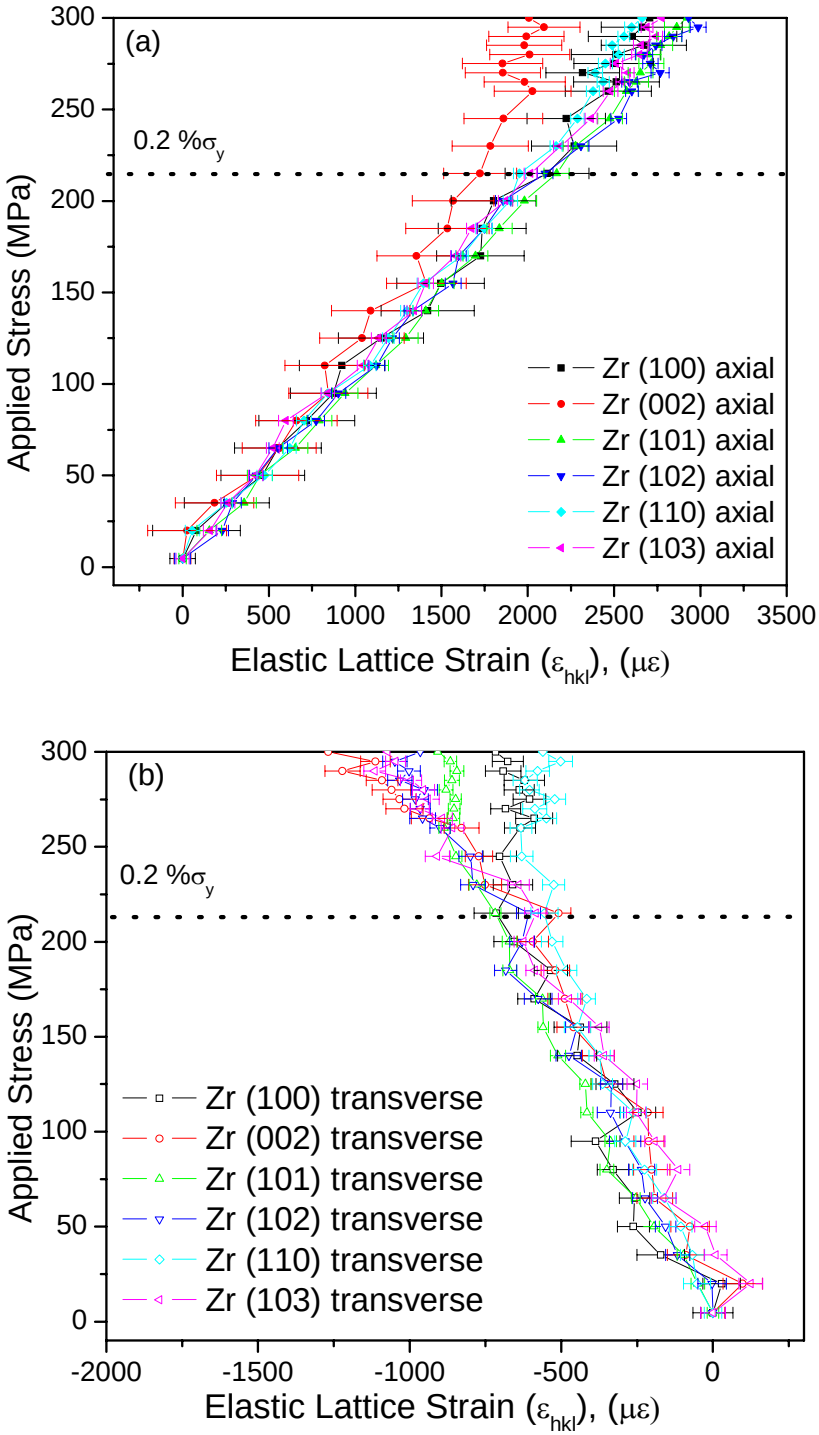

FIGURE 4.30 Elastic anisotropy for the specimen with 1,600 ppm hydrogen, (a) axial and (b) transverse directions.

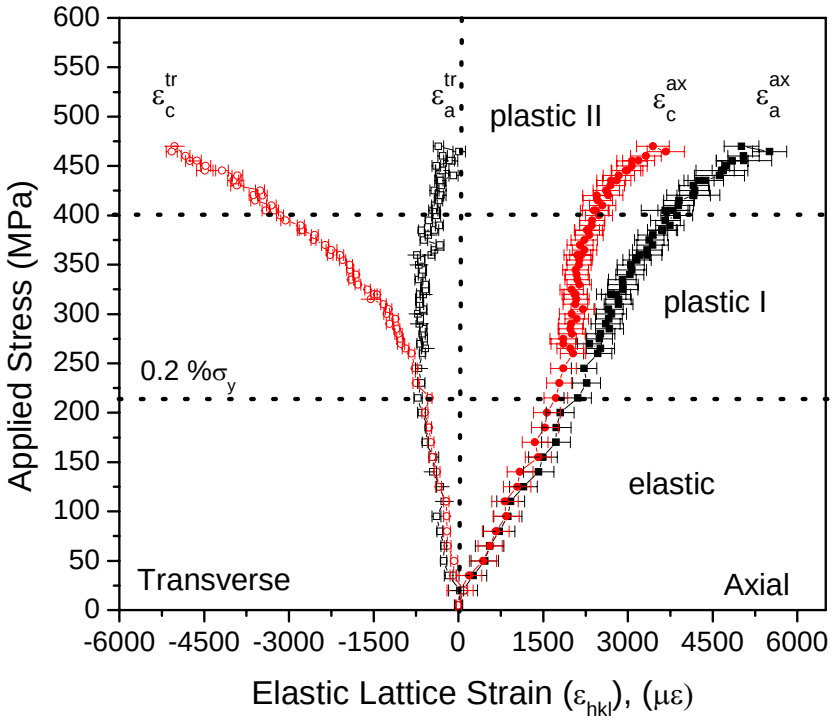

FIGURE 4.31 The elastic lattice strains in specimen with 1,600 ppm hydrogen as a function of applied stress. The *a*- and *c*-axes strains are shown for the axial and transverse directions (■ ε_a^{ax}, ● ε_c^{ax}, □ ε_a^{tr}, and ○ ε_c^{tr}).

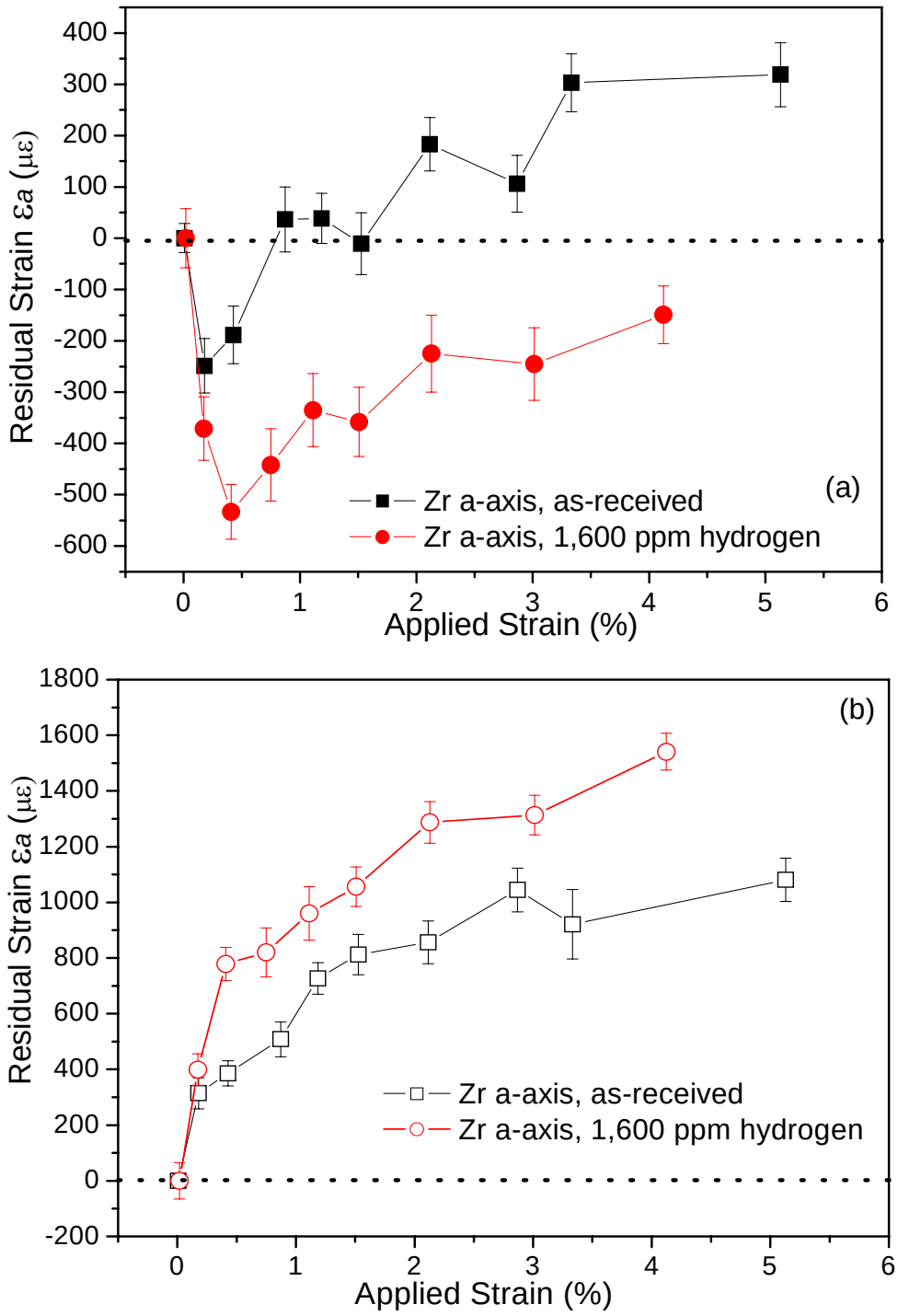

FIGURE 4.32 Comparison of the residual lattice strain ε_a as a function of the applied strain between the specimens with 1,600 ppm hydrogen and in as-received condition (a) axial direction (■ as-received and ● 30-minute charged) and (b) transverse direction (□ as-received and ○ 30-minute charged).

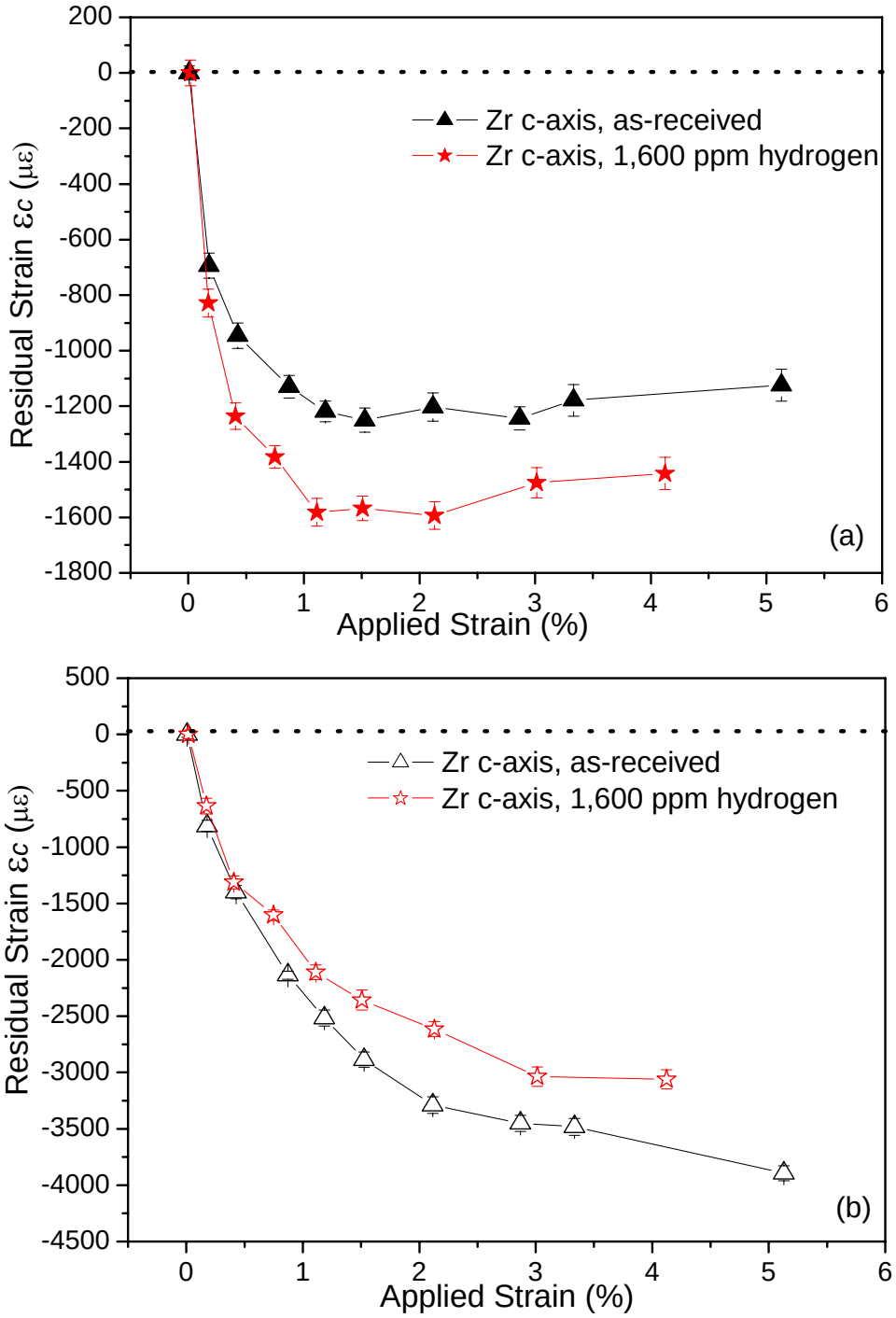

FIGURE 4.33 Comparison of the residual lattice strain ε_c as a function of the applied strain between the specimens with 1,600 ppm hydrogen and in as-received condition (a) axial direction (▲ as-received and ★ 30-minute charged) and (b) transverse direction (△ as-received and ☆ 30-minute charged).

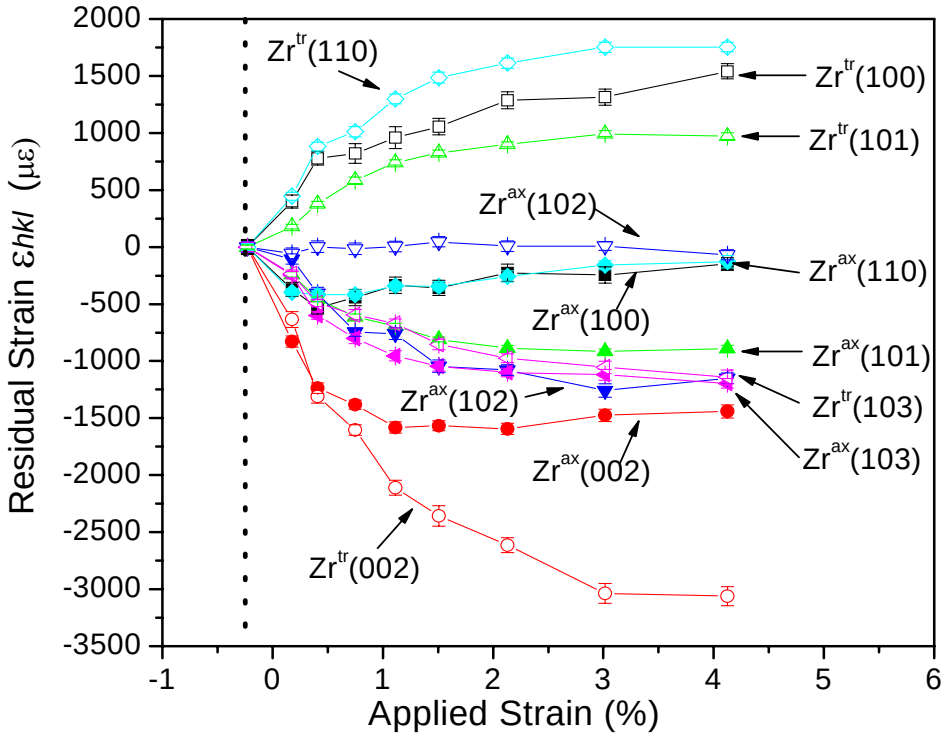

FIGURE 4.34 Residual lattice strains as a function of the plastic strain in axial and transverse directions for six different Zr reflections in the specimen with 1,600 ppm hydrogen.

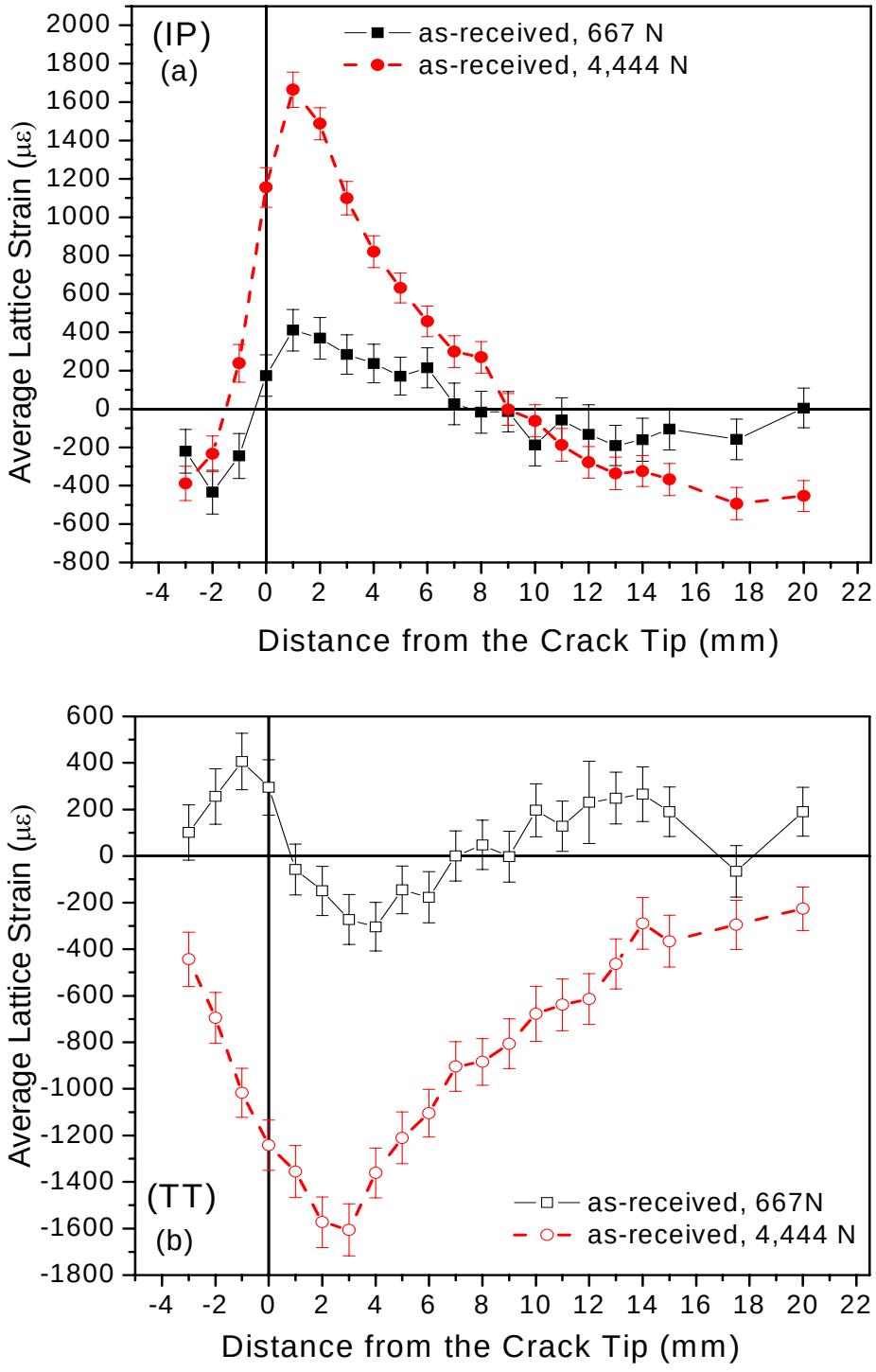

FIGURE 4.35 Average lattice strain around the crack tip for the sample the in as-received condition (a) in-plane direction (IP) and (b) through-thickness direction (TT).

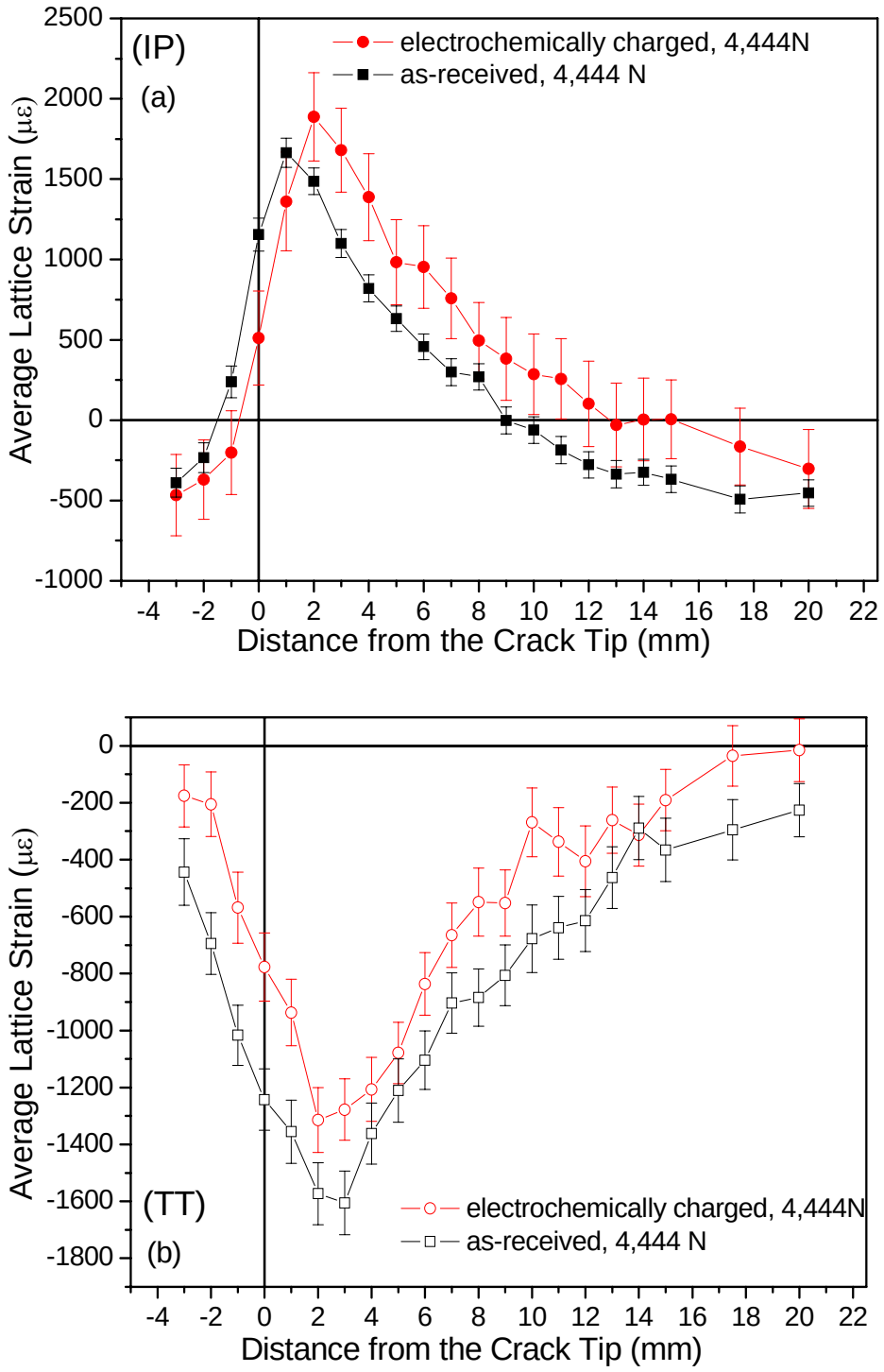

FIGURE 4.36 Comparison of average lattice strain around the crack tip between the specimen electrochemically charged with hydrogen and in the as-received condition (a) in-plane direction (IP) under 4,444 N load and (b) through-thickness direction (TT) under 4,444 N load,

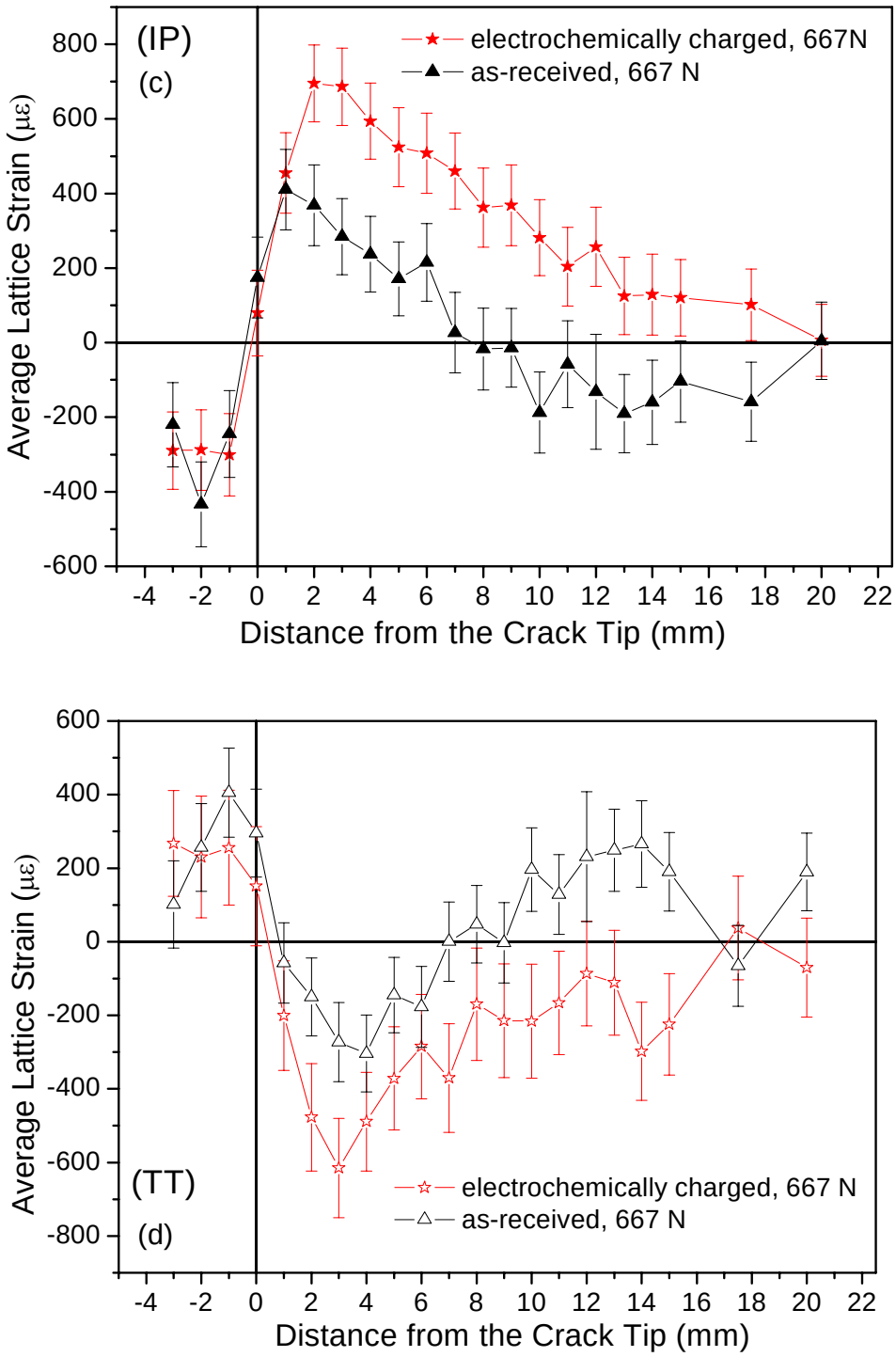

FIGURE 4.36 Continued (c) in-plane direction (IP) under 667 N load and (d) through-thickness direction (TT) under 667 N load.

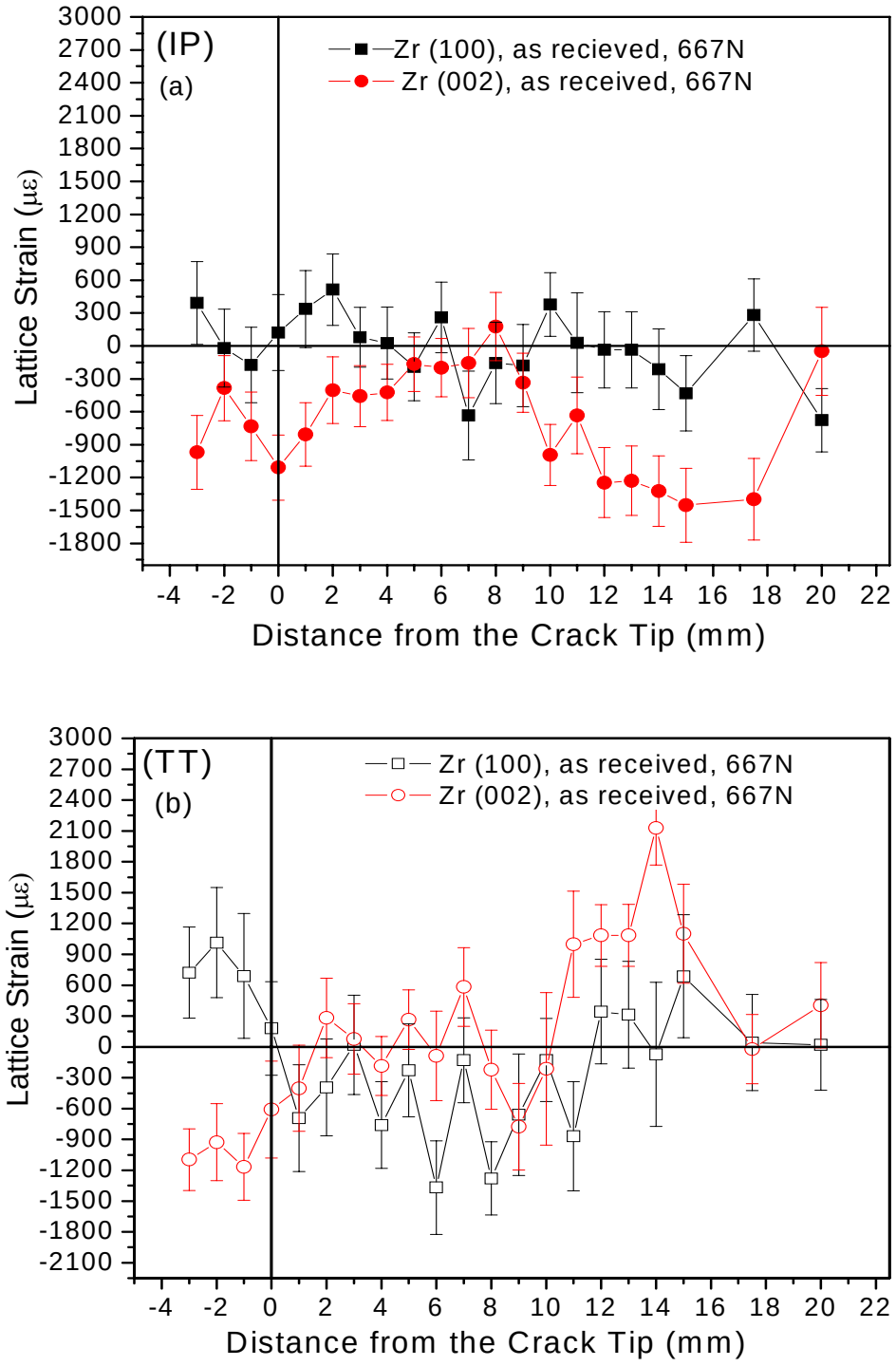

FIGURE 4.37 Elastic lattice strain as a function of the distance from the crack tip for the sample in the as-received condition under an applied load of 667 N (a) in-plane direction (IP) and (b) through-thickness direction (TT). (■ ε_{100}^{ax}, ● ε_{002}^{ax}, □ ε_{100}^{tr}, and ○ ε_{002}^{tr}).

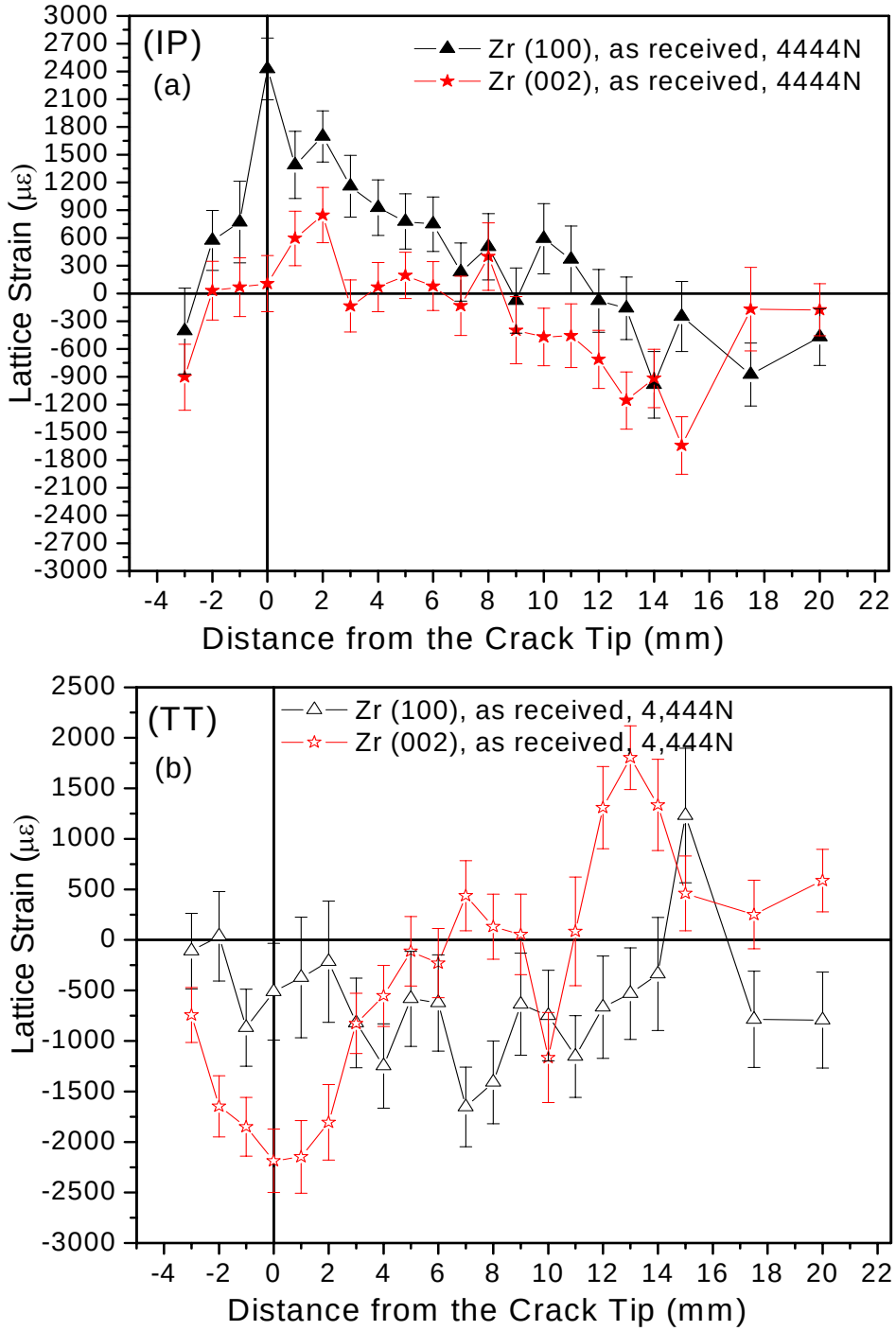

FIGURE 4.38 Elastic lattice strain as a function of the distance from the crack tip for the sample in the as-received condition under an applied load of 4,444 N (a) in-plane direction (IP) and (b) through-thickness direction (TT). (▲ ε_{100}^{ax}, ★ ε_{002}^{ax}, △ ε_{100}^{tr}, and ☆ ε_{002}^{tr}).

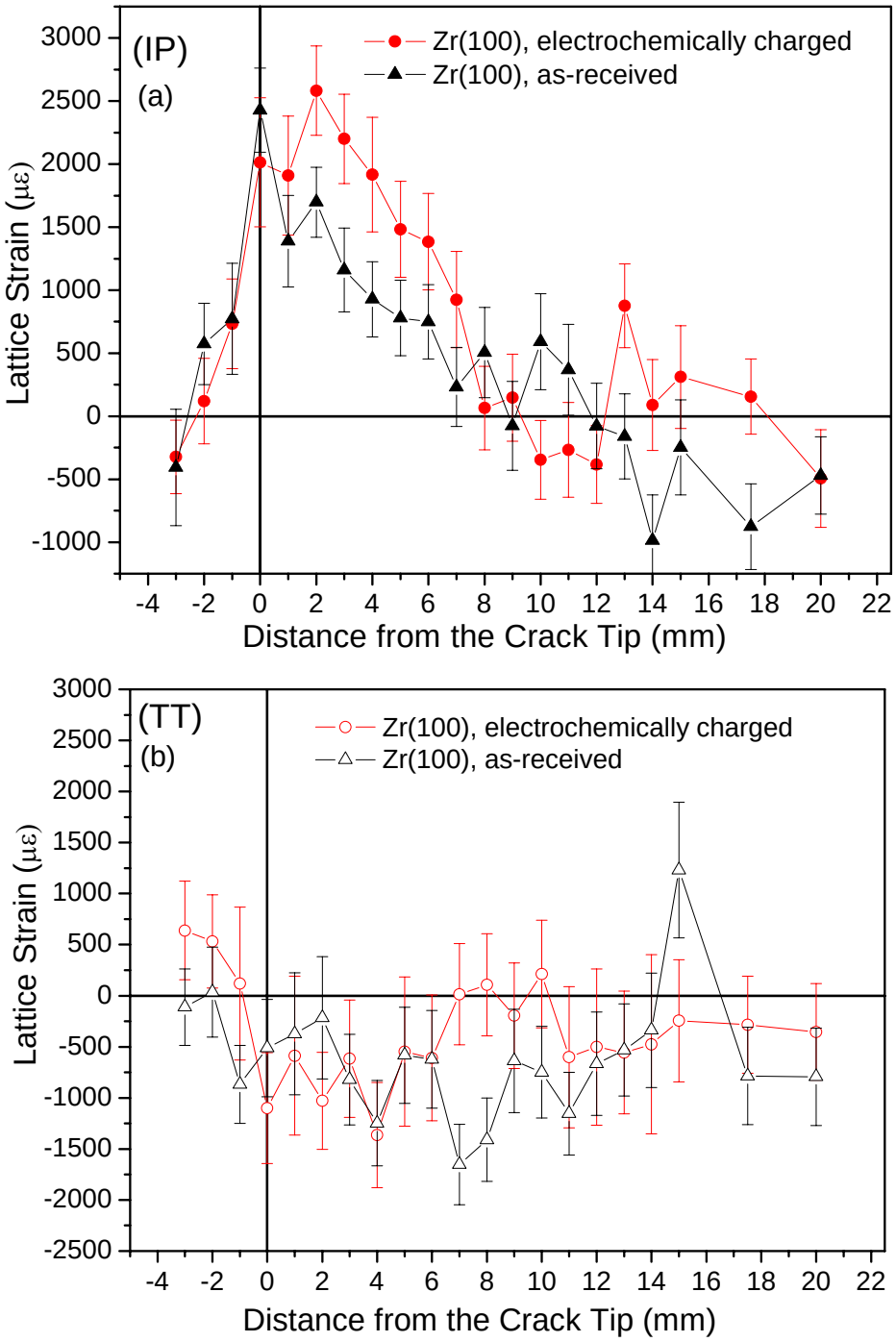

FIGURE 4.39 Comparison of the elastic lattice strains in a-axis as a function of the distance from the crack tip under an applied load of 4,444 N between the sample in the as-received condition (AR) and electrochemically charged with hydrogen (ECH) (a) in-plane direction (IP) and (b) through-thickness direction (TT). (▲ $\varepsilon_{100}^{\text{ax-AR}}$, ● $\varepsilon_{100}^{\text{ax-ECH}}$, △ $\varepsilon_{100}^{\text{tr-AR}}$, and ○ $\varepsilon_{100}^{\text{tr-ECH}}$).

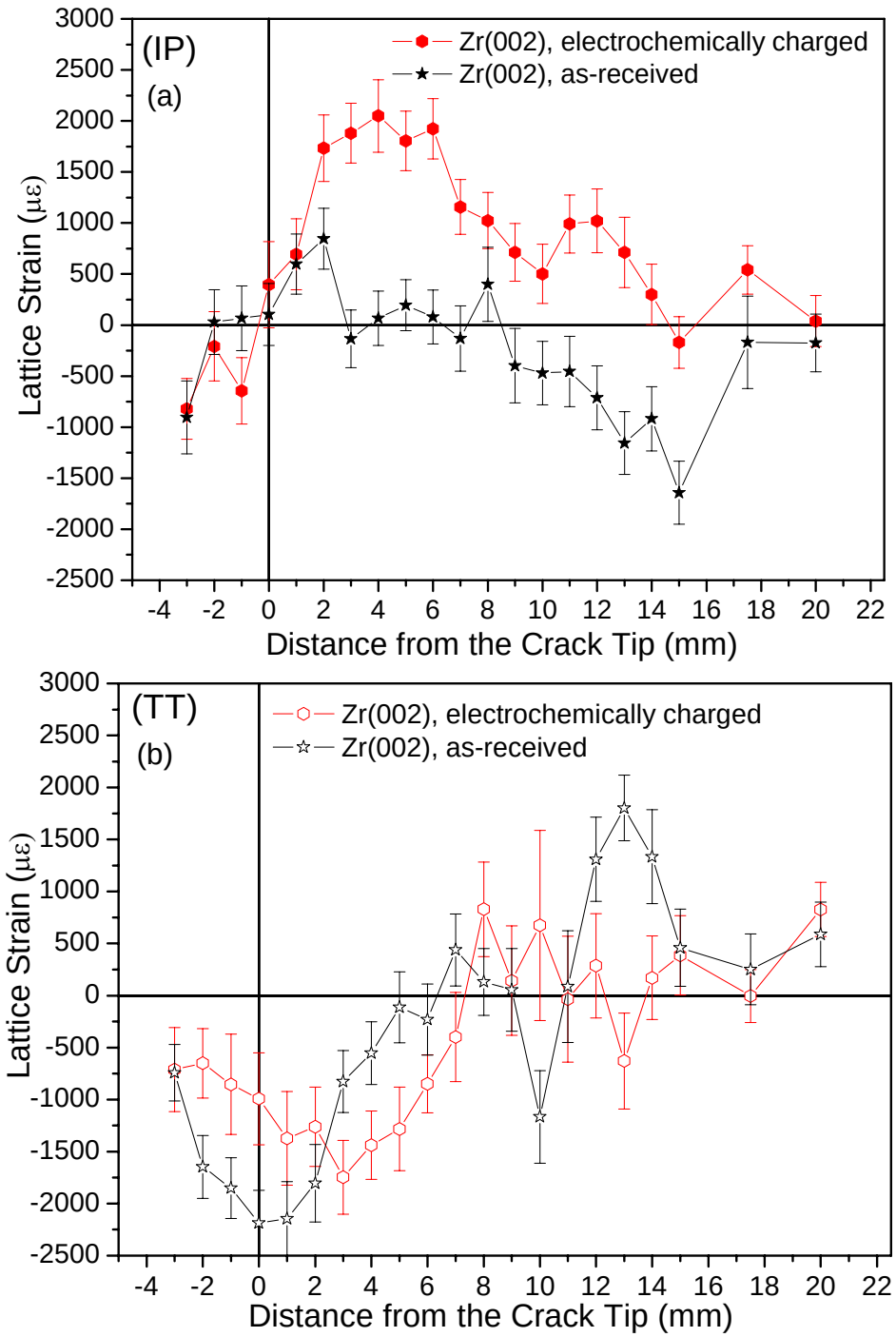

FIGURE 4.40 Comparison of the elastic lattice strain in c-axis as a function of the distance from the crack tip under an applied load of 4,444 N between the samples in as-received condition (AR) and electrochemically charged with hydrogen (ECH) (a) in-lane direction (IP) and (b) through-thickness direction (TT). (★ $\varepsilon_{002}^{\text{ax-AR}}$, ● $\varepsilon_{002}^{\text{ax-ECH}}$, ☆ $\varepsilon_{002}^{\text{tr-AR}}$, and ○ $\varepsilon_{002}^{\text{tr-ECH}}$).

VITA

Elena Garlea was born in Aiud, Romania, on April 18, 1975. She attended schools in Blaj, Romania, where she graduated from Iacob Muresianu High School, chemistry-biology specialty, in June, 1993. Elena entered the Babes-Bolyai University, Cluj-Napoca during July of 1993 where in June, 1997 she received a Bachelor of Science degree in Chemistry, graduating with a GPA of 9.66/10. She developed a broad work experience in coating formulation, quality control, the food industry, and teaching. After working as a chemist at PPG Industries, Troy, MI, she entered the Graduate Program in Materials Science and Engineering Department at The University of Tennessee in August 2003. The Master of Science degree in Materials Science and Engineering was received December 2005, with a GPA of 3.9/4.